Aus dem Fachbereich der Molekularen Biophysik
Theoretische Medizin und Biowissenschaften der Medizinischen Fakultät
der Universität des Saarlandes, Homburg/Saar

STIM2.3: An evolutionary late regulator of intracellular calcium signaling

DISSERTATION

Zur Erlangung des akademischen Grades

eines Doktor der Naturwissenschaften

der Medizinischen Fakultät

der Universität des Saarlandes

2023

vorgelegt von

VANESSA POTH

Geb. am 12.10.1991 in Idar-Oberstein

Tag der Promotion: 22.06.2023

Dekan: Prof. Dr. med. Michael D. Menger

Berichterstatter: Prof. Dr. rer. nat. Barbara Niemeyer-Hoth

Prof. Dr. med. Frank Schmitz

TABLE OF CONTENTS

Summary

Calcium (Ca^{2+}) regulates as a highly versatile second messenger a variety of short-term as well as long-term cellular processes such as gene transcription, muscle contraction and apoptosis. Store-operated Ca^{2+} entry (SOCE) regulates basal and receptor-triggered Ca^{2+} signaling with STIM (stromal interaction molecule) proteins sensing the endoplasmic reticulum (ER) Ca^{2+} content and triggering Ca^{2+} entry by gating ORAI channels in the plasma membrane (PM) in response to store depletion.

This study identified and characterized the splice variant STIM2.3, which arises with the evolution of hominoids ~20 million years ago. In STIM2.3, insertion of a short exon results in a translated protein lacking the C-terminal serine/proline rich region, the microtubule-associated EB binding sites, and the polybasic domain (PBD), which functions as an ER retention signal and anchors STIM proteins at phospholipids at the inner leaflet of the PM. STIM2.3 showed the highest expression in human cerebellum as analyzed from different postmortem human brain regions by quantitative RT-PCR. Ca^{2+} imaging experiments revealed a STIM2.3-mediated gain-of-function SOCE phenotype, which is encoded by the larger C-terminal deletion and not by the splice-specific residues. However, deletion of only the PBD (STIM2.2Δ5K) in full-length STIM2 abolished SOCE, which was rescued by the simultaneous mutation of both EB binding motifs (STIM2.2 2xIP+Δ5K). These results demonstrate competitive functions of plasma membrane anchoring and microtubular tracking on STIM2 function. Despite the lack of the PBD, STIM2.3 showed ER distribution at rest and colocalized with STIM1 and STIM2.2 in regions near the nucleus but did not show pre-clustering as STIM2.2 at ER PM junctions under basal conditions. Full store depletion abolished differences in colocalization, however, deletion of the PBD significantly reduced Tg-induced cluster formation and size in STIM2.3, STIM2.2Δ5K and STIM2.2 2xIP+Δ5K in the absence of endogenous STIM despite their differential SOCE phenotypes.

While deletion of STIM1 and/or STIM2 using CRISPR/Cas9 in the neuroblastoma cell line SH-SY5Y significantly increased voltage-gated Ca^{2+} influx, transient over-expression of either STIM2.1, STIM2.2 or STIM2.3 did not significantly reduce K^+-induced Ca^{2+} influx. However, neuronal differentiation of SH-SY5Y cells using retinoic acid and BDNF demonstrated a reciprocal negative feedback regulation of voltage-gated and store-operated Ca^{2+} influx.

Furthermore, the effect of STIM2.3 on the activation of the Ca^{2+}-dependent transcription factor NFAT was analyzed. While basal NFAT translocation was observed with STIM2.2 expression in SH-SY5Y STIM1/STIM2$^{-/-}$, activation of NFAT was only observed after Tg-induced store depletion with STIM2.3. Strikingly, the PBD is not necessarily required for Tg-induced STIM2-mediated NFAT translocation in the absence of microtubular binding protein attachment sites but more likely recruits and stabilizes the signalosome under conditions with low agonist concentration. Additionally, STIM2.3 displayed reduced interaction with and activation of the energy sensor AMPKα using co-immuno-precipitation. To further investigate potential physiological functions of STIM2.3 in a more neuronal background, a stable cell line was generated using the neuroblastoma cell line SH-SY5Y lacking endogenous STIM2. RNA sequencing and subsequent Gene Ontology analysis of this cell line showed significantly upregulated neuronal processes such as axonogenesis, axon guidance, brain development and neurogenesis compared to SH-SY5Y WT cells expressing both STIM1 and STIM2.2. These data together with the qRT-PCR results indicate that splicing of STIM2.3 might be associated with the evolutionary increasing cerebellar size in apes and the development of fine motor skills and language.

In summary, functional characterization of the C-terminally truncated STIM2.3 uncovers a novel and evolutionarily late regulator of intracellular Ca^{2+} signaling.

Zusammenfassung

Kalzium (Ca^{2+}) reguliert als sekundärer Botenstoff eine Vielzahl an zellulären Prozessen wie Transkription, Muskelkontraktion und Apoptose. Beim speichergesteuerten Kalziumeinstrom (SOCE) aktivieren STIM-Proteine als ER-ständige Kalziumsensoren in Abhängigkeit der luminalen Kalziumkonzentration die in der Plasmamembran (PM) lokalisierten ORAI-Proteine, die den Ca^{2+}-selektiven CRAC-Kanal bilden.

In dieser Arbeit wurde die STIM2 Spleißvariante STIM2.3, die mit Evolution der Hominoiden vor etwa 20 Millionen Jahren entstand, funktionell charakterisiert. Im Vergleich zum konventionellen STIM2 (hier STIM2.2 genannt) führt die Insertion eines kurzen Exons in STIM2.3 zu einem STIM2-Protein, dem die C-terminale Serin/Prolin-reiche Region, die Mikrotubuli-assoziierte Bindestelle sowie die polybasische Domäne (PBD) fehlen. Letztere fungiert als ER-Retentionssignal und verankert STIM-Proteine an Phospholipiden innerhalb der PM. Das STIM2.3-spezifische Exon konnte in verschiedenen humanen postmortem Gehirnregionen nachgewiesen werden und zeigte zusammen mit *ORAI2* die höchste Expression im Cerebellum. Die funktionelle Charakterisierung mittels Ca^{2+}-Imaging-Experimenten in unterschiedlichen Zelllinien zeigte, dass STIM2.3 zu einem erhöhten Kalziumeinstrom führt. Während der STIM2.3-spezifische SOCE-Phänotyp durch Deletion der C-terminalen Aminosäuren 675-833 reproduziert werden konnte, führte die Deletion der PBD (Δ5K) in STIM2.2 zu einem signifikant reduzierten SOCE, welcher durch die simultane Mutation beider EB-Bindemotive wiederhergestellt werden konnte (Δ5K+2xIP). Trotz der fehlenden PBD zeigte STIM2.3 eine Lokalisation innerhalb des ERs und kolokalisierte mit STIM1 und STIM2.2 in Zellkern-nahen Regionen. Allerdings zeigte STIM2.3 im Gegensatz zu STIM2.2 keine Präcluster in Plasmamembran-nahen Bereichen. Während eine vollständige Speicherentleerung Unterschiede in der Kolokalisation beseitigte, zeigten alle STIM2-Proteine, denen die PBD fehlte, eine reduzierte Clustergröße nach Stimulation mit Thapsigargin in Abwesenheit von endogenen STIM-Proteinen.

Während die Deletion von STIM1 und STIM2 mittels CRISPR/Cas9 in der Neuroblastoma Zelllinie SH-SY5Y den spannungsgesteuerten Kalziumeinstrom erhöhte, führte die transiente Expression von STIM2.1, STIM2.2 oder STIM2.3 zu keiner signifikanten Reduktion des K^+-induzierten Kalziumpeaks. Die neuronale Differenzierung der SH-SY5Y-Zelllinien unter Verwendung von Retinsäure und BDNF zeigte jedoch eine negative

Feedback-Regulation des spannungs- und speichergesteuerten Kalziumeinstroms. Zusätzlich wurde der Effekt von STIM2.3 auf die Aktivierung des Ca^{2+}-abhängigen Transkriptionsfaktors NFAT untersucht. Während die Expression von STIM2.2 in SH-SY5Y STIM1/STIM2$^{-/-}$-Zellen bereits zu einer basalen NFAT-Translokation in den Zellkern führte, konnte eine STIM2.3-vermittelte NFAT-Aktivierung erst nach Speicher-entleerung beobachtet werden. Zudem ist die PBD nicht unbedingt für die Tg-induzierte STIM2-vermittelte NFAT-Aktivierung erforderlich, sofern die Bindestellen der Mikrotubuli-assoziierten Proteine fehlen. Sie ist vielmehr für die Rekrutierung und Stabilisierung des NFAT-Signalkomplexes unter Bedingungen mit niedriger Agonist-konzentration verantwortlich. Des Weiteren zeigte STIM2.3 eine reduzierte Interaktion mit und gleichzeitig reduzierte Aktivierung des Energiesensors AMPKα in Ko-Immun-präzipitationsexperimenten.

Um mögliche physiologische Funktionen von STIM2.3 in einem mehr neuronalen Zellsystem zu untersuchen, wurde eine stabile SH-SY5Y STIM2$^{-/-}$-Zelllinie generiert, die STIM2.3 stabil überexprimiert. RNA-Sequenzierung und die nachfolgende Gen-Ontologie-Analyse identifizierte mehrere signifikant hochregulierte neuronale Prozesse wie Neurogenese, Axonogenese, Gehirnentwicklung und Axonentwicklung. Diese Ergebnisse in Kombination mit den Expressionsdaten deuten darauf hin, dass das Spleißen von STIM2.3 mit der evolutionär wachsenden Cerebellumgröße in menschen-artigen Affen sowie der Entwicklung feinmotorischer Fähigkeiten und Sprache in Zusammenhang stehen könnte.

Zusammenfassend konnte in dieser Arbeit mit der funktionellen Charakterisierung der C-terminal verkürzten SOCE-Komponente STIM2.3 ein neuer Regulator der intra-zellulären Kalziumhomöostase identifiziert werden.

Chapter 1

1 Introduction

1.1 Calcium homeostasis and signaling

Calcium (Ca^{2+}) is the fifth most abundant element in the human body with a total mass of ~ 1 kg. Approximately 99 % of calcium is bound as crystalline calcium phosphate in bones and teeth, providing skeletal strength and a dynamic calcium storage. Only 1 % exists as soluble Ca^{2+} ions regulating as a highly versatile second messenger a variety of physiological processes such as gene transcription, cytokine release and neurotransmission [reviewed in Berridge et al. 2000 and Peacock 2010]. Second messengers are intracellular signaling molecules which enable cells to amplify the original signal recognized by cell surface receptors reacting to external signals to trigger intracellular responses. Thus, their concentrations need to be tightly regulated to generate specific signals with distinct spatial and temporal dynamics [reviewed in Berridge et al. 2003].

Cellular Ca^{2+} homeostasis is such a finely tuned system which is maintained by pumps, transporters, and compartmentalization (Fig. 1). While the extracellular Ca^{2+} concentration is $\sim 1\text{-}2$ mM, the intracellular Ca^{2+} concentration is ~ 100 nM avoiding phosphate precipitation within the cytosol. This $\sim 20{,}000$-fold concentration gradient across the plasma membrane enables cells to efficiently respond to external signals by rapidly increasing the cytosolic Ca^{2+} concentration through Ca^{2+} efflux from internal stores or Ca^{2+} influx from the outside. To maintain such a low cytosolic Ca^{2+} concentration, plasma membrane Ca^{2+} ATPases (PMCA) and Na^+/Ca^{2+} or $Na^+/K^+/Ca^{2+}$ exchanger (NCX/NCKX) efficiently transport Ca^{2+} across the plasma membrane (PM) into the extracellular space [reviewed in Carafoli 1987]. PMCA is a P-type ATPase that hydrolyzes one molecule ATP per transported Ca^{2+} ion [reviewed in E. Carafoli 1991], whereas NCX transports one Ca^{2+} ion against the gradient in exchange for three Na^+ ions with the gradient. Depending on the electrochemical gradient, the ion exchange can be reversed [Niggli et al. 1981; reviewed in Carafoli et al. 2001]. While PMCA exhibits a high Ca^{2+} affinity but low transport capacity, thereby maintaining Ca^{2+} concentration even under resting conditions, the low-affinity high-capacity Na^+/Ca^{2+} exchanger limits excessive Ca^{2+} concentrations, thus, rapidly adapting Ca^{2+} signals [Clapham 2007].

The endoplasmic reticulum (ER) serves as the main internal Ca^{2+} store with a concentration of $\sim 500\,\mu M$. The sarcoplasmic/endoplasmic Ca^{2+} ATPase (SERCA) compensates Ca^{2+} leakage at the translocon complex during protein biosynthesis thereby stabilizing cytosolic and luminal Ca^{2+} concentrations. In addition, SERCA ensures refilling of the ER store following activation of the IP_3 or ryanodine (RyR) receptor, which lead to rapid Ca^{2+} release and store depletion [Lomax et al. 2002]. In addition to the ER, Ca^{2+} sequestration in further organelles is essential to maintain Ca^{2+} homeostasis and adjust Ca^{2+} signals [reviewed in Clapham 2007]. The secretory pathway Ca^{2+} ATPase (SPCA) is a P-type ATPase with high affinity for Ca^{2+} and Mn^{2+}, which mediates Ca^{2+} uptake into the Golgi and is essential for post-translational processing of secretory proteins. SPCA was first identified in *S. cerevisiae* as the product of the *PMR1* gene [reviewed in Pizzo et al. 2011]. Due to their spatial vicinity to Ca^{2+} channels in the ER and PM, mitochondria can take up large amounts of Ca^{2+} from cytosolic microdomains, thus, regulating Ca^{2+} channel activity by shaping Ca^{2+} signals in a spatio-temporal dependent manner [Rizzuto et al. 1998].
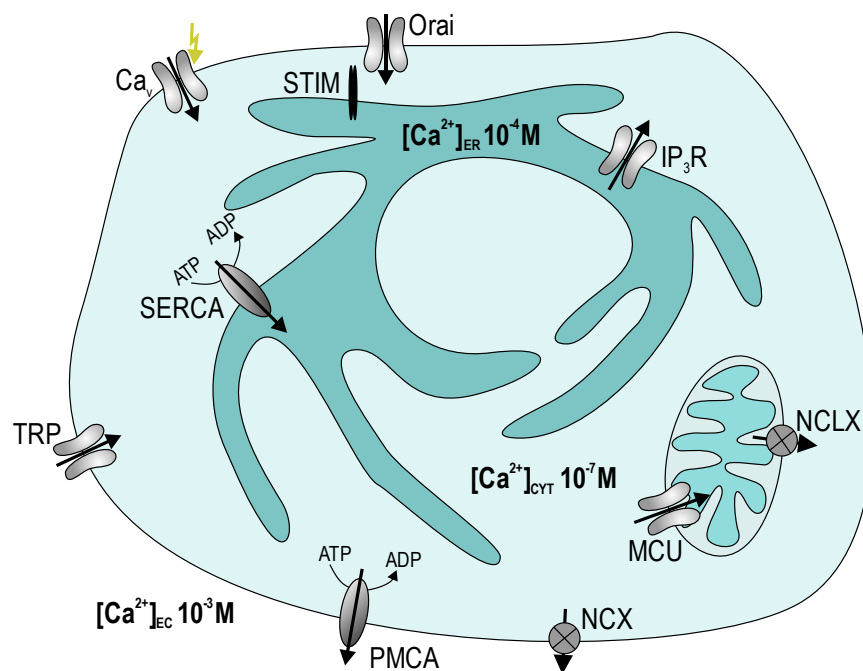
Figure 1 Cellular Ca^{2+} homeostasis. Plasma membrane: Ca^{2+} influx into the cell is mediated by voltage-gated (Ca_v) and store-operated (Orai) channels or channels with distinct activation mechanisms (TRP), while PMCA (plasma membrane Ca^{2+} ATPase) and NCX (Na^+/Ca^{2+} exchanger) mediate extrusion of Ca^{2+}. **Endoplasmic reticulum (ER):** Activation of the ER-resident IP3 receptor (IP_3R) results in Ca^{2+} release from the ER, whereas SERCA (sarco-/endoplasmic reticulum Ca^{2+} ATPase) transports Ca^{2+} into the ER. **Mitochondria:** Ca^{2+} influx into the mitochondrial matrix is mediated by the mitochondrial Ca^{2+} uniporter (MCU), NCLX (Na^+/Ca^{2+} (Li^+) exchanger) mediates Ca^{2+} export into the cytosol.

The outer mitochondrial membrane is permeable for Ca^{2+}, whereas transport of Ca^{2+} across the inner mitochondrial membrane requires transporters. Free Ca^{2+} within the mitochondrial matrix controls Ca^{2+} sensitive processes such as ATP production and is balanced by Ca^{2+} influx and efflux [reviewed in Clapham 2007]. While Ca^{2+} uptake is mediated by the highly selective mitochondrial Ca^{2+} uniporter (MCU) within the inner mitochondrial membrane [Nicholls and Åkerman 1982], Ca^{2+} is exported by the Na^+/Ca^{2+} and H^+/Ca^{2+} exchanger (NCLX) [R. Palty et al. 2010; reviewed in Rizzuto et al. 2012]. In addition to pumps and transporters, a large group of buffer proteins can reversibly bind free Ca^{2+} ions via specific structural motifs, regulating Ca^{2+} concentration [reviewed in Carafoli et al. 2001]. The EF hand is one of the most prominent Ca^{2+} binding motif consisting of one loop flanked by two helices. The negatively charged carboxylic oxygen atoms of glutamic and aspartic acid together with the carbonyl oxygen of the protein backbone within the EF hand motif selectively chelate Ca^{2+} in a pentagonal bipyramidal conformation. Ca^{2+} binding proteins often contain more than one EF hand motif. Ca^{2+} binding modifies charge and conformation of proteins resulting in activation or inhibition [reviewed in Carafoli 1987 and Clapham 1995].

An increase in cytosolic Ca^{2+} concentration can be achieved by Ca^{2+} release from internal stores or by Ca^{2+} influx through plasma membrane resident Ca^{2+} channels, which are classified into three types. While receptor operated channels (ROC) are activated by binding of extracellular ligands, voltage operated channels (VOC) respond to a change in membrane potential. The third group are store-operated channels (SOC), which are indirectly activated following receptor induced generation of signals lowering the ER Ca^{2+} to then activate a ligand of plasma membrane localized ion channels [Rizzuto et al. 2009]. Distinct Ca^{2+} related processes such as cytoskeletal remodeling, muscle contraction and activation of the transcription factor NFAT (nuclear factor of activated T cells) are regulated depending on duration and amplitude of the generated signals [reviewed in Berridge et al. 2003].

1.2 Store-operated Ca^{2+} entry

Store-operated Ca^{2+} entry (SOCE) is the main Ca^{2+} influx pathway in non-excitable cells transforming external stimuli into internal signaling cascades. In 1986, Putney first described the underlying mechanism as *capacitative Ca^{2+} entry*, in which the filling state

of the ER as the main internal Ca^{2+} pool finely regulates activation of plasma membrane Ca^{2+} channels. In this model, initial store depletion induced by inositol (1,4,5) triphosphate (IP_3) results in rapid Ca^{2+} influx into the cell, which is attenuated by withdrawal of the agonist and simultaneous store refilling [J W Putney 1986]. Hoth & Penner (1992) as well as Zweifach & Lewis (1993) succeeded in recording in mast cells and T cells a sustained Ca^{2+} current induced by store depletion using whole-cell patch clamp. This inward rectifying and highly selective Ca^{2+} current is referred to as I_{CRAC} (calcium release-activated calcium current) [Hoth and Penner 1992; Zweifach and Lewis 1993].
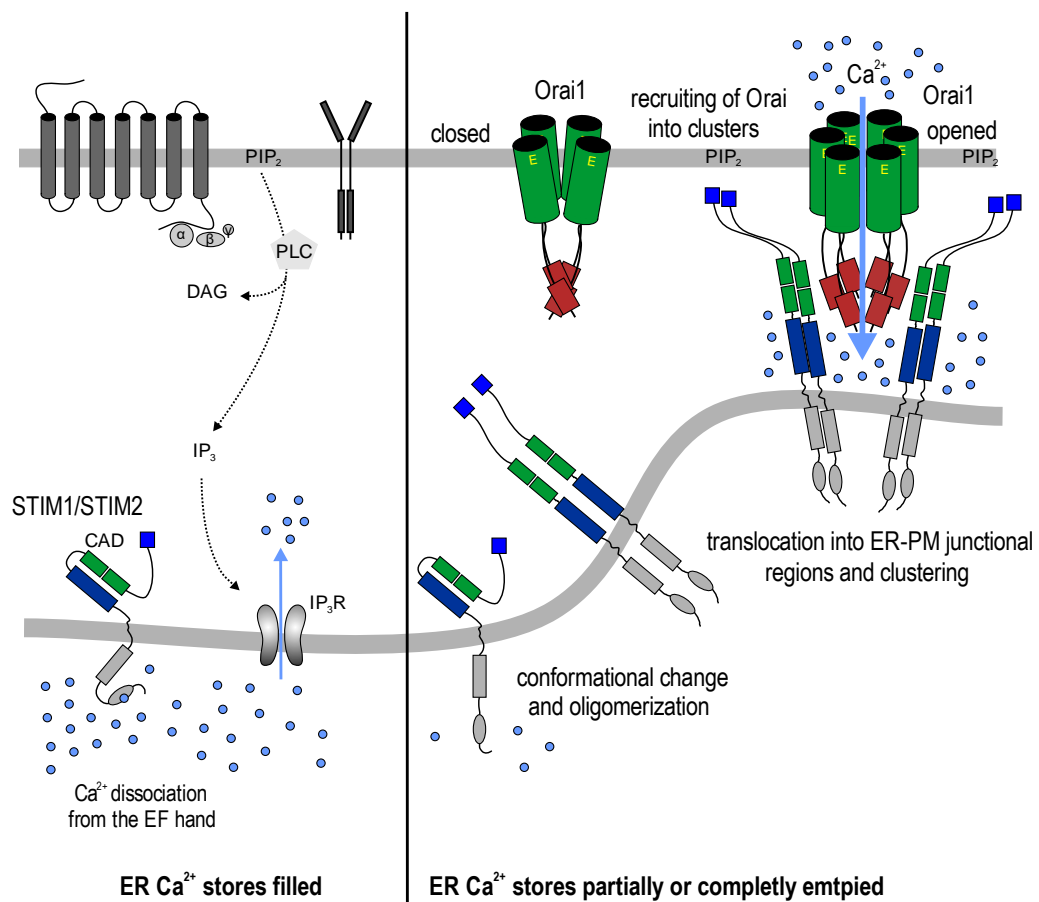
Figure 2 Store-operated Ca^{2+} entry (SOCE). Activation of plasma membrane resident G-protein coupled, or tyrosine kinase receptors leads to catalytic formation of IP_3 by phospholipase C (PLC), which subsequently activates IP_3R (IP_3 receptor) in the ER membrane resulting in Ca^{2+} release from the ER into the cytosol. Er resident STIM (stromal interaction molecule) proteins sense decreasing luminal Ca^{2+} concentration and undergo conformational change upon Ca^{2+} dissociation from their luminal Ef hand followed by oligomerization and translocation into ER PM junctional regions. There, they recruit and activate Orai proteins forming the Ca^{2+} selective channel in the plasma membrane. (Modified from Feske et al. 2012).

Under physiological conditions, formation of IP_3 and diacylglycerol (DAG) is catalyzed by phospholipase C (PLC) by cleavage of phosphatidylinositol (4,5) bisphosphate (PIP_2) following activation of G protein- or tyrosine kinase-coupled surface receptors. The second messenger IP_3 transiently activates the ER resident IP_3 receptor (IP_3R) leading to

Ca²⁺ release from the internal store [reviewed in M.J. Berridge 1993]. In research, the irreversible SERCA inhibitor Thapsigargin is regularly used to artificially deplete the ER stores. In contrast to physiological activation of the IP$_3$ receptor, Thapsigargin results in passive depletion [Lytton et al. 1991]. The decreasing luminal Ca²⁺ concentration is sensed by the ER resident stromal interaction molecules (STIM). Upon store depletion, dissociation of Ca²⁺ from their N-terminal EF hand results in conformational change of STIM followed by oligomerization and translocation into ER PM junctional regions. There, STIM proteins activate SOCE by recruiting and directly gating ORAI, which form the Ca²⁺ selective CRAC channel in the plasma membrane (Fig. 2) [J W Putney 1986; reviewed in Shaw and Feske 2012]. The resulting Ca²⁺ influx and increase in cytosolic Ca²⁺ concentration refills internal Ca²⁺ pools inducing dissociation of the STIM-ORAI complexes and thereby simultaneously attenuating SOCE [Malli et al. 2008]. In immune cells, SOCE as the main Ca²⁺ influx mechanism regulates immune response by inducing dephosphorylation and nuclear translocation of the transcription factor NFAT, which was first described as a protein complex in 1988 [J. P. Shaw et al. 1988; Kar et al. 2011]. About two decades after the mechanism of coupling ER filling to plasma membrane channels was proposed, by genome wide RNAi screens in *Drosophila* and the human cell lines HeLa and Jurkat T cells, and by sequencing SCID patient material the key components of SOCE were identified in 2005 and 2006: STIM and ORAI. In mammals, there are currently two STIM (STIM1, STIM2) and three ORAI (ORAI1, ORAI2, ORAI3) homologues [Liou et al. 2005; Roos et al. 2005; Feske et al. 2006; S. L. Zhang et al. 2006; Vig et al. 2006].

1.2.1 STIM

STIM structure

STIM are type I transmembrane proteins, which function as ER resident Ca²⁺ sensors and constantly track along the microtubule network under resting conditions. After signal peptide cleavage, anchoring of STIM within the ER membrane is mediated by an α-helical transmembrane domain separating STIM into a luminal and cytosolic part containing distinct functional domains (Fig. 3). The N terminus is localized within the ER lumen consisting of a signal peptide, two EF hands and a sterile alpha motif (SAM) domain [R. T. Williams et al. 2001; Stathopulos et al. 2008]. In contrast to STIM1, STIM2 contains a longer signal peptide theoretically resulting in three posttranslational processed proteins. Complete cleavage of the signal peptide results in the ER resident

STIM2, whereas preSTIM2 still containing the signal peptide displays cytosolic localization and store-independently regulates resting Ca^{2+} concentration to maintain homeostasis. Further processing of the cleaved signal peptide results in a 91 aa long fragment affecting NFκB mediated gene transcription [Graham et al. 2011].

The first canonical EF (cEF) hand senses the filling state of the ER and is stabilized in the Ca^{2+} bound conformation by the second non-canonical or hidden EF (n/hEF) hand. In addition, interaction of the SAM domain with the EF hand in the presence of Ca^{2+} stabilizes the inactive state and prevents oligomerization of STIM under resting conditions [Stathopulos et al. 2008; L. Zheng et al. 2011]. In contrast to STIM1, STIM2 regulates basal Ca^{2+} levels due to a lower Ca^{2+} affinity of the EF hand, which enables STIM2 to respond to even minor fluctuations in luminal Ca^{2+} concentration [Brandman et al. 2007]. Hence, STIM2 exhibits mobile and immobile clusters at ER PM junctions under basal conditions coordinated by IP_3 receptor function and the associated Ca^{2+}
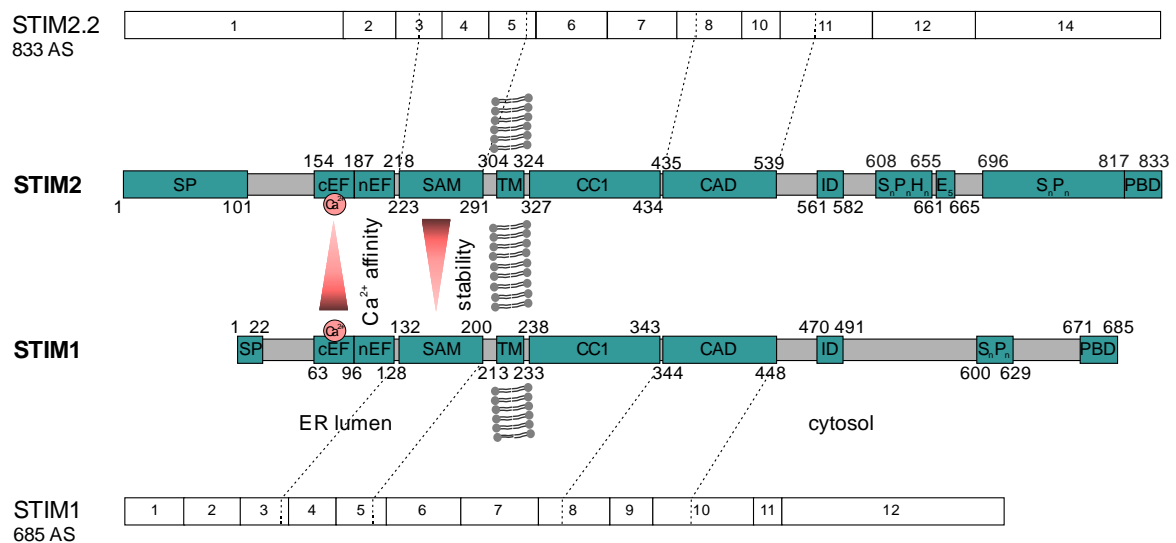
Figure 3 Schematic exon and protein structure of STIM1 and STIM2. Schematic exon structure of STIM2 (**top**) and STIM1 (**bottom**). Length of the individual exons are indicated by the length of the corresponding boxes. **Middle:** Schematic protein structure of STIM1 and STIM2 with indicated functional domains and their subcellular localization. Amino acid positions are indicated at the corresponding domains. Compared to STIM1, STIM2 has a longer exon 1 resulting in a longer signal peptide. STIM proteins are type I t̲ransm̲embrane (TM) proteins. The N terminus is localized in the ER lumen consisting of a c̲anonical (cEF) hand, essential for Ca^{2+} binding, a n̲on-canonical or h̲idden (nEF/hEF) E̲F hand, which mediates together with the SAM (sterile α motif) domain the inactive conformation upon Ca^{2+} binding. While the cEF hand of STIM2 exhibits a lower Ca^{2+} affinity, the SAM domain has a higher stability. The C terminus is localized in the cytosol comprised of a c̲oiled-c̲oiled (CC1) domain, the c̲hannel a̲ctivating d̲omain (CAD), which forms an inhibitory clamp by interacting with the CC1 domain under resting conditions and activates Orai proteins upon store depletion, an i̲nhibitory d̲omain (ID), a s̲erine/p̲roline rich region (S_n/P_n) and a terminal p̲oly b̲asic d̲omain (PBD). STIM2 additionally contains a s̲erine/p̲roline/h̲istidine ($S_nP_nH_n$) rich region and a poly E̲ domain (E_5). (Modified from B. Niemeyer)

release. In turn, immobilization of STIM2 clusters and IP$_3$R activity are determined by ambient PLC mediated PIP$_2$ hydrolysis. The close vicinity of STIM2 clusters to IP$_3$R facilitates the initiation of SOCE and regulation of Ca^{2+} signaling [Ahmand et al. 2022]. In addition, STIM2 pre-clustering recruits STIM1 into ER PM junctional regions promoting ORAI activity under low agonist concentrations. This STIM2-mediated modulation of STIM1/ORAI1 coupling adjusts receptor induced signaling and amplifies the physiological response [Subedi et al. 2018]. Recently, Son et al. (2020) demonstrated that STIM2 targets STIM1/ORAI1 complexes to ER PM junctions promoting assembly of the signalosome complex essential for NFAT activation.

The N-terminal conformational change following Ca^{2+} dissociation from the EF hand translates into unfolding of the cytosolic region. The cytosolic C terminus of STIM consists of three coiled-coiled domains (CC1-CC3), an inhibitory domain (ID), a serine/proline rich region (S$_n$/P$_n$) and a poly basic domain (PBD) [Stathopulos et al. 2009]. CC2 together with CC3 form the channel activating domain (CAD), which is also referred to as SOAR, OASF or CCb9 [Kawasaki et al. 2009; Muik et al. 2009; Park et al. 2009; Yuan et al. 2009]. A short positively charged basic sequence within CAD is essential for CRAC channel activation by interacting with an acidic stretch of the ORAI1 coiled-coiled domain [Calloway et al. 2010; reviewed in Lunz et al. 2019]. In addition, the short α3 domain within the CAD forms a gating interface with ORAI1 separating STIM1-mediated interaction with from gating of the channel. Consequently, STIM1 α3 domain promotes the transmission of the gating signal affecting CRAC channel opening in a direct or indirect manner [Butorac et al. 2019]. The CAD domain not only mediates ORAI activation but additionally stabilizes STIM oligomers together with the N-terminal SAM domain after activation [Muik et al. 2009; Park et al. 2009; Covington et al. 2010]. Despite high similarities between both STIM homologues, an amino acid exchange within the CAD converts STIM2 into a weaker ORAI activator compared to STIM1, preventing excess Ca^{2+} influx triggered by its increased sensitivity [X. Wang et al. 2014]. Under resting conditions, interaction of an acidic stretch within CC1 with CC3 prevents oligomerization of STIM in addition to the N-terminal stabilization, maintaining the quiescent state [Korzeniowski et al. 2012; Fahrner et al. 2014]. However, a recent study demonstrated that also CC2 and the ID are both involved in forming the inhibitory clamp to stabilize the CC1/CAD interaction [Shrestha et al. 2022]. Mullins et al. identified seven negatively charged acidic amino acids (DDVDDMDEE) within the ID$_{STIM1}$ responsible for Ca^{2+} dependent inactivation (CDI) of SOCE, which was abolished by mutation of six

amino acids. A mutational screen identified the residues D476, D478 and D479 as the crucial core of this domain. In STIM2, the first two acidic residues (**GG**V<u>DDL</u><u>DED</u>) are lacking. However, ID in STIM1 might not only function as a Ca^{2+} sensor but is likely to interact with the outward facing pore residue W76 in ORAI1 inducing full Ca^{2+} dependent inactivation [Mullins and Lewis 2016]. Moreover, ID_{STIM1} keeps STIM1 in an inactive state under resting conditions by stabilizing the CC1/CC3 interaction [S. K. Lee et al. 2020]. In addition to the inhibitory domain, the Ca^{2+} binding protein calmodulin also regulates as a second messenger Ca^{2+} dependent inactivation of SOCE. Binding of CaM to the CAD or PBD in the presence of Ca^{2+} diminishes the STIM-ORAI interaction and induces dissociation of the STIM oligomers. Consequently, simultaneous store refilling and subsequent binding of Ca^{2+} to the luminal EF hand promotes the inactive state of STIM [Bauer et al. 2008; Bhardwaj et al. 2013; X. Li et al. 2017]. The hydrophobic residues L374/V375 and L390/F391 within the CAD mediate Ca^{2+}/CaM binding inducing slow Ca^{2+} dependent activation. While the first residues exclusively regulate CaM binding, the second site is required for ORAI activation [Bhardwaj et al. 2020]. The terminal polybasic domain consists of lysine residues anchoring STIM to phospholipids at the inner leaflet of the plasma membrane with STIM2 exhibiting a higher binding affinity to PIP_2 compared to STIM1 [Bhardwaj et al. 2013]. While a typical di-lysine motif within the PBD in STIM2 serves as an ER retention signal, a lysine-rich domain and a di-arginine motifs mediate ER localization of STIM1. However, in contrast to STIM2, STIM1 also shows cell surface localization in mitotic cells [Ercan et al. 2012]. Moreover, plasma membrane localized STIM1 is constitutively associated with and store-independently activates arachidonic acid-regulated (ARC) channels in response to low concentrations of intracellular arachidonic acid [Thompson and Shuttleworth 2013]. ARC channels are formed by ORAI1 and ORAI3 [Mignen et al. 2008a].

Regulation of STIM function

Both STIM1 and STIM2 contain microtubular binding protein (MBP) attachment sites (S/T-x-I-P, here EB) within their cytosolic region. End binding (EB) proteins constantly track plus-ends of growing microtubules facilitating movement of STIM1 within the ER under resting conditions [Grigoriev et al. 2008]. However, association of STIM1 with EB1 delays translocation by competing with attachment of the PBD to the PM, thus, diminishing SOCE [Honnappa et al. 2009; Chang et al. 2018]. Dissociation of the EB1/STIM1 complex can be mediated by ERK1/2-induced phosphorylation of STIM1 at

residues S575, S608 and S621 following stimulation of receptor tyrosine kinases. Hence, the reversible phosphorylation state of STIM1 is dependent on the ER Ca^{2+} content [Pozo-Guisado et al. 2013]. However, a recent study demonstrated that STIM1 phosphorylation by ERK1/2 is not essential for SOCE activation [Hammad et al. 2021]. Despite provoking damage to cellular organelles and processes at high concentrations, reactive oxygen species (ROS) such as H_2O_2 can also function as intracellular second messengers modulating protein function by oxidation of reactive cysteines [reviewed in Sauer et al. 2001 and Auten and Davis 2009]. While Ca^{2+}- and phosphorylation-mediated modulation of STIM1 function is well understood, the effects of oxidative stress on STIM activity have been controversial. Hawkins et al. demonstrated that in STIM1, oxidative stress induces S-glutathionylation of the N-terminal C56 thereby mimicking store depletion by reducing the Ca^{2+} binding affinity, thus, promoting STIM1 oligomerization and SOCE activation. In contrary, Prins et al. reported the formation of a disulfide bridge between C56 and C49 induced by the ER-resident oxidoreductase ERp57, which negatively affects SOCE by preventing STIM1 clustering. Compared to STIM1, STIM2 contains ten additional reactive cysteine residues within its C-terminal region susceptible for redox modification but their role on STIM2 function under oxidative stress was still not clear. Recently, Gibhardt et al. identified C313 within the CC1 domain as the main redox sensor of STIM2. Indeed, oxidation of C313 alters activation of STIM2 and thereby prevents STIM2-mediated CRAC channel activation [Gibhardt et al. 2020].

1.2.2 ORAI

The homologues ORAI1, ORAI2 and ORAI3 form as homo- or heteromultimers the highly selective CRAC channel in the plasma membrane leading to Ca^{2+} influx triggered by store depletion [Lis et al. 2007]. While a tetrameric structure of the channel had been widely discussed [Ji et al. 2008; Mignen et al. 2008b; Penna et al. 2008; Demuro et al. 2011], the crystal structure of *Drosophila* Orai1 revealed a hexameric stoichiometry [Hou et al. 2012a; Cai et al. 2016; Yen et al. 2016]. Under resting conditions, ORAI1 has been reported to be a dimer [Penna et al. 2008; Demuro et al. 2011], however, Alansary et al. (2020) demonstrated that ORAI1 forms higher oligomers by using concatemeric constructs also at rest. Each ORAI subunit consists of four transmembrane domains connected via two extracellular and one intracellular loop. Both N and C terminus are localized within the cytosol [Vig et al. 2006; Hou et al. 2012b]. The Ca^{2+} permeable pore of the channel is formed by the first transmembrane domain (TMD) of each monomer

with a ring of glutamate residues (E106) towards the extracellular side serving as the selectivity filter. On the intracellular side, a basic region stabilizes the closed conformation of the channel [Mcnally et al. 2009; Yubin Zhou et al. 2010]. Coupling of STIM1 to the C-terminal region of ORAI1 induces a conformational change leading to channel pore opening. Several C-terminal residues and the nexus region (aa 261-265) connecting the TM4 with its helical extension have been identified to play a crucial role in ORAI1 activation. Coupling of STIM1 to the ORAI1 nexus region translates the interaction into the inner core without directly gating the N-terminal pore forming helix [Yandong Zhou et al. 2016]. Mutation of L273 and L276 within ORAI1 abolished STIM1-ORAI1 coupling important for channel gating [Tirado-lee et al. 2015]. In addition, several hydrophobic and basic amino acids within the conserved N-terminal ETON region spanning the amino acids 73-90 are essential for CRAC channel opening [Derler et al. 2013]. While K85 is essential for channel activation, the residues L74 and W76 define the characteristics of I_{CRAC} [Derler et al. 2018]. The hereditary loss of function mutation R91W, which helped to identify the CRAC channel forming ORAI1 protein, is responsible for defects in SOCE and T cell function in patients with severe combined immunodeficiency [Feske et al. 2006]. The R91W mutation increases the hydrophobicity at the ORAI1 N terminus and the first transmembrane segment perturbating channel gating while coupling of STIM1 to ORAI1 R91W seemed unaffected [Derler et al. 2009]. The interaction of STIM1 with the ORAI1 C terminus is structurally resolved, however, direct interaction of STIM1 with the ETON region is still controversial. While recent studies by Baraniak et al. confirmed that interaction of STIM1 with the ORAI1 C terminus is sufficient to trigger an allosteric change gating the CRAC channel pore, several groups demonstrated that the ETON region functions as a binding interface providing electrostatic stabilization of the pore, which is required for CRAC channel gating and activation [Derler et al. 2013, 2018; Fahrner et al. 2018; Knapp et al. 2022; McNally et al. 2013; Raz Palty and Isacoff 2016; Park et al. 2009]. Recently, Kar et al. (2021) identified a specific region in the ORAI1 N terminus, which is absent in other ORAI homologues, essential for recruiting of the signalosome to promote and couple NFAT activation to local Ca^{2+} signals.

Compared to ORAI1, the homologues ORAI2 and ORAI3 display distinct activation and inactivation kinetics and selectivity [Lis et al. 2007]. In contrast to ORAI2 and ORAI3, ORAI1 contains a N-glycosylation site mediating SOCE inhibition via interaction with

siglec, whereas ORAI3 is less redox sensitive due to a missing extracellular cysteine residue [Bogeski et al. 2010; Alansary et al. 2015; Dörr et al. 2016].

Genetically encoded loss- and gain-of-function mutations within *STIM1* and *ORAI1* are associated with severe combined immunodeficiency, Stormorken syndrome, congenital miosis and tubular myopathies [Thompson et al. 2009; Morin et al. 2014; Nesin et al. 2014; Böhm et al. 2017].

1.3 STIM in signaling pathways

1.3.1 STIM and energy metabolism

Maintenance of energy homeostasis is as critical as Ca^{2+} homeostasis to ensure proper cellular functionality. The AMP-activated protein kinase (AMPK) is the key energy sensor activated by energy stress, which is signaled by increased AMP/ATP and ADP/ATP ratios. AMPK is a heterotrimeric complex comprising of one catalytic α subunit and two regulatory subunits, β and γ [Herzig and Shaw 2018]. The crucial step of AMPK activation is the phosphorylation of the critical residue Thr172 in the activation loop of the α-subunit by upstream kinases. AMPK phosphorylation by the tumor suppressor liver kinase B1 (LKB1) in response to energy stress is supported by binding of AMP to the γ-subunit, resulting in allosteric activation and inhibition of dephosphorylation of AMPK [Gowans et al. 2013; Hawley et al. 1995; Sanders et al. 2007; Suter et al. 2006; Woods et al. 2003]. In addition to LKB1, the Ca^{2+}/Calmodulin dependent kinase kinase II (CaMKKII/β) has been identified to directly phosphorylate AMPK in response to increased cytosolic Ca^{2+} levels independently of the adenosine nucleotide concentration [Woods et al. 2005]. Following activation, AMPK phosphorylates downstream targets involved in various pathways, switching anabolic ATP consuming (e.g. gluconeogenesis, lipogenesis) to catabolic ATP producing processes (e.g. glycolysis, fatty acid oxidation) to restore energy balance [Garcia and Shaw 2017]. In 2011, Mungai et al. first reported a correlation between SOCE and CaMKKII-dependent AMPK activation. In osteosarcoma cells and mouse embryonic fibroblasts, hypoxia induced activation of SOCE results in AMPK phosphorylation, which was independent of changes in adenosine nucleotide levels and LKB1. Hence, silencing of STIM1 or CaMKKII abolished hypoxia induced AMPK activation [Mungai et al. 2011]. In addition, a study performed in the neuroblastoma cell line SH-SY5Y confirmed involvement of SOCE in AMPK activation, in which phosphorylation of Thr172 requires

STIM1-mediated Ca^{2+} influx [Olianas et al. 2014]. However, Chauhan et al. confirmed a direct interaction of STIM2, but not STIM1, with all AMPK subunits and the upstream CaMKKII indicating that STIM2 acts as a scaffolding protein to promote interaction of CaMKKII with and Ca^{2+}-dependent activation of AMPK [Chauhan et al. 2019]. In fact, a phosphoproteomic screen conducted in extracts of exercised muscle probes across different species (mouse, rat, human) identified STIM1 as a downstream target of AMPK in response to exercise, demonstrating a feedback mechanism of energy homeostasis and Ca^{2+} signaling. AMPK mediated phosphorylation of S257 within the CC1 domain inhibits SOCE enabling muscle to adapt to exercise [Nelson et al. 2019]. A second study examined the effect of metformin treatment *in vivo* identifying both STIM1 and STIM2 as AMPK targets with S521/S257 and S630/S261 as the phosphorylation sites, respectively. Metformin induced STIM phosphorylation reduced SOCE supporting a protective effect of AMPK signaling on Ca^{2+} homeostasis [Stein et al. 2019].

1.3.2 Neuronal SOCE

As a versatile second messenger, Ca^{2+} is of critical importance to neurons as it regulates neurotransmission and synaptic plasticity. In neurons, Ca^{2+} influx is mainly mediated by activation of voltage-gated channels or ionotropic receptors. Various studies provide evidence for the implication of the Ca^{2+} sensors STIM in neuronal Ca^{2+} signaling [reviewed in L. Majewski and Kuznicki 2015].

Both STIM1 and STIM2 are expressed in the murine and human brain. While the proteins will be found in every cell type of the brain, their relative abundance varies greatly (Allen Brain Atlas) [reviewed in Kraft 2015]. In cerebellar Purkinje neurons (PN), STIM1 refills dendritic Ca^{2+} stores essential for metabotropic glutamate receptor (mGluR1) dependent neurotransmission and synaptic plasticity [Hartmann et al. 2014]. Consequently, loss of STIM1 in PN results in reduced excitability, impaired plasticity and memory consolidation defects [Ryu et al. 2017]. In cortical neurons, activated STIM1 recruits NCX1 and TRPC6 (transient receptor potential canonical 6) to promote SOCE-dependent store refilling. The TRPC6-mediated Na$^+$ influx thereby facilitates the NCX1 reverse mode contributing to STIM1-mediated Ca^{2+} influx [Tedeschi et al. 2022]. However, a non-canonical regulation of voltage-gated Ca^{2+} channels by STIM1 has also been proposed to modulate neurotransmission. A negative feedback mechanism coupling the filling state of the ER to voltage-gated Ca^{2+} entry (VGCE) results in STIM1-mediated inhibition and long-term internalization of the L-type Ca$_v$1.2. [Park et al. 2010;

Youjun Wang et al. 2010]. Moreover, glutamate induced Ca^{2+} influx through NMDA receptors (NMDAR) and VGCCs leads to STIM1 activation resulting in inhibition of VGCCs, thereby, shaping postsynaptic plasticity [Dittmer et al. 2017]. Both knockout and overexpression of STIM1 and STIM2 in mice affects spatial memory, contextual learning and behavior [Garcia-alvarez et al. 2015; T. Majewski et al. 2016; L. Majewski et al. 2020]. In cultured hippocampal neurons, STIM1 and STIM2 exert distinct functions. STIM1 displays high mobility and regulates local Ca^{2+} influx required for dendritic spine and filopodia formation in developing neurons, whereas STIM2 is less mobile and maintains Ca^{2+} homeostasis in more mature neurons [Kushnireva et al. 2021]. In excitatory neurons, STIM2 modulates dendritic spine formation and remodeling by regulating SOCE-independently trafficking and protein kinase A (PKA)-mediated phosphorylation of the AMPA (α-amino-3-hydroxy-5-methyl-4-isoxazolepropionic acid) receptor (AMPAR) subunit GluA1, thus, modulating synaptic plasticity [Garcia-Alvarez et al. 2015; Yap et al. 2017]. However, both STIM1 and STIM2 directly interact with the AMPAR subunits GluA1 and GluA2 following store depletion demonstrating contribution of AMPAR-mediated Ca^{2+} influx to neuronal SOCE [Gruszczynska-Biegala et al. 2016]. In addition to ORAI and AMPAR, both STIM1 and STIM2 directly interact with the NMDA (N-methyl-D-aspartate) receptor (NMDAR) subunits NR2A and NR2B negatively modulating NMDA-evoked Ca^{2+} influx in cortical neurons [Gruszczynska-Biegala et al. 2020]. In contrast, Patil et al. proposed that NMDAR-mediated Ca^{2+} entry recruits STIM proteins to directly gate and activate the non-selective ion channel pannexin-1 (Panx1), which has been linked to neurological disorders such as epilepsy and stroke but also regulates spine formation and synaptic plasticity. Indeed, this study unveiled a mechanism that couples Panx1 activation to ER-initiated signaling, which is crucial not only in neuronal but also in non-neuronal cells requiring distinct STIM activation pathways independent of NMDAR signaling. [Patil et al. 2022]. On the presynaptic side, transient increase in Ca^{2+} concentrations mediated by STIM2 enhances spontaneous neurotransmission at excitatory synapses through the Ca^{2+} sensor synaptotagmin 7 (Syt7). Neuronal dysregulation caused by chronic ER stress was partially prevented by SOCE inhibition or deletion of Syt7, indicating that increased presynaptic STIM2-mediated neurotransmitter release augments ER stress-induced neurodegenerative processes [Chanaday et al. 2021].

Reduced STIM2 expression and impaired nSOC have been associated with Alzheimer's disease, which is characterized by destabilization and loss of mushroom spines.

Overexpression of STIM2 restored the nSOC-CaMKII pathway stabilizing mushroom spines and reduced amyloid plaques in brain of 5FAD mice. [Sun et al. 2014; Chernyuk et al. 2016]. Pchitskaya et al. identified the underlying mechanism, in which interaction of STIM2 with EB3, a microtubule plus end binding protein, regulated dendritic spine morphology. Disruption of the association results in a reduced number of dendritic spines and altered spine morphology [Pchitskaya et al. 2017]. In fact, J. Zhou et al. (2019) directly linked impaired neuronal SOCE to neurodegenerative loss of mushroom spines by uncovering a mechanism, in which ER stress-induced autophagic degradation of STIM2 results in disruption of dendritic spines.

1.4 Alternative splicing of STIM

The human genome encodes ~ 20,000 proteins identified by the Human Genome Project, which was initiated in 1990 and completed in 2003. While only ~1-2 % of the genome is coding DNA, the residual 98-99 % are non-coding, mostly functioning as regulatory elements such as promotors, enhancers, or non-coding RNAs. The complexity of the human organism does not rely in the quantity of coding genes, but on the transcriptional network regulating codification of different proteins [reviewed in Moraes and Góes 2016]. Alternative splicing is a potent means to adapt protein function and to significantly increase proteomic diversity despite limited gene numbers. In the process, a large number of functionally distinct protein isoforms arise from one mRNA through different exon combinations. Alternative splicing is an intricate mechanism, which is both developmental and cell type specific and can be altered by environmental influences [Yan Wang et al. 2015]. Beside the positive effect of increasing protein diversity, dysregulation of alternative splicing is associated as the cause or consequence with human diseases [Tazi et al. 2009].

Both STIM1 and STIM2 are large genes encoded by 12 exons sharing similar exon structures with differences in the length of exon 1 and 11 translating into mature proteins with a diverging distal cytosolic region. The great exon number increases the probability of alternative splicing. Database mining predicts several splice variants for STIM1 and STIM2. In the past years, the region around the exons 10 – 12 in STIM1 has been identified as a hotspot for alternative splicing. In 2011, Darbellay et al. first described the STIM1 splice variant STIM1L, which is predominantly expressed in skeletal muscle. During myogenesis, alternative splicing of exon 11 in STIM1 results in

the C-terminal extended STIM1L, which additionally contains an actin binding domain. The interaction with actin enables STIM1L to form permanent clusters with ORAI1 leading to faster activation of SOCE in muscle cells [Darbellay et al. 2011]. Moreover, both STIM1 and STIM1L activate the non-selective cation channel TRPC1 following ORAI stimulation. However, STIM1L displayed stronger interaction with TRPC1 compared to STIM1, which may explain the less efficient activation of ORAI1 [Dyrda et al. 2020]. In addition to insertion of exon 11L, splice insertion of the short alternative exon 13B in the same region (mutually exclusive splicing) results in the C-terminal truncated STIM1B, which reduces SOCE in a partially residue dependent manner. The neuronal splice variant STIM1B preferentially localizes to neurites and presynaptic regions in contrast to the more somatic localization of STIM1. Additionally, repetitive high frequency stimulation of autaptic hippocampal neurons overexpressing STIM1B leads to a strong enhancement of synaptic transmission due to increased vesicle replenishment that is absent in STIM1 expressing cells [Ramesh et al. 2021]. The recently published and longer STIM1 variant STIM1A is a dominant-negative regulator of SOCE expressed in various tissues. While the C-terminal insertion of domain A reduces SOCE in a sequence-dependent manner and facilitates FCDI (fast Ca^{2+} dependent inactivation), STIM1A increases NFAT activation by reducing PDE8-mediated cAMP degradation and increasing PIP5K activity [Knapp et al. 2022]. Almost simultaneously, Xie et al. postulated, that STIM1A, which they termed as STIM1β, promotes tumor cell proliferation and growth by increasing Ca^{2+} influx. Insertion of domain A (β) potentially perturbates the autoinhibition of STIM mediated by the CC1-CAD interaction, while interfering with the co-inhibitory ID to release CAD and to promote ORAI1 gating [Xie et al. 2022]. In addition to the C-terminal splicing, database mining also predicts N-terminal spliced variants for STIM1 with alternative 5' UTRs resulting in STIM1 variants lacking the signal peptide and the Ca^{2+}-sensing EF hand. Whether these splice events occur in combination with C-terminal splicing and whether these variants would function as cytosolic store independent SOCE activators, still needs to be investigated [Knapp et al. 2022].

Database mining predicts three STIM2 variants with STIM2.2 being the conventional and most investigated variant (Fig. 4). Insertion of the eight amino acid motif VAASYLIQ within the CAD domain converts STIM2.1 (STIM2β) to a potent inhibitor of SOCE. Interaction of STIM2.1 with ORAI1 is impaired and thus prevents SOCE activation [Miederer et al. 2015; Rana et al. 2015].
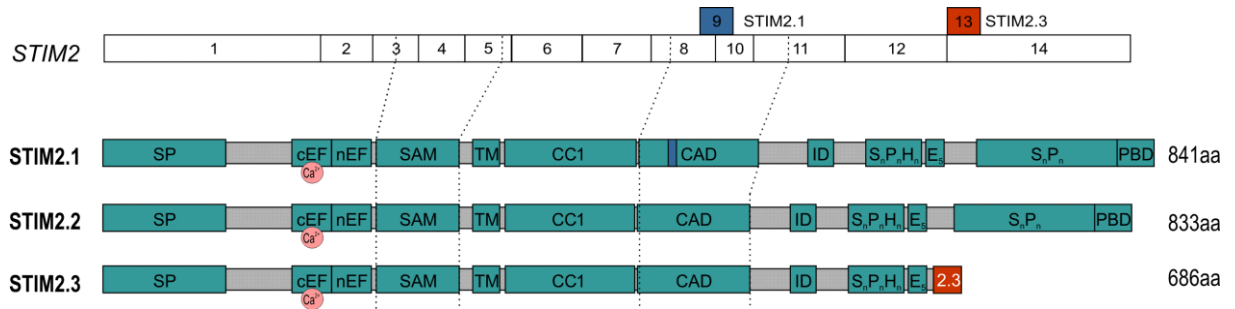
Figure 4 STIM2 splice variants. Schematic exon structure of STIM2 with alternative exon 9 (blue; STIM2.1) and exon 13 (red; STIM2.3). Schematic protein structure of the STIM2 variants STIM2.1, STIM2.2 and STIM2.3 with common functional domains and splice specific domains of STIM2.1 (blue) and STIM2.3 (red). (Modified from B. Niemeyer)

While a homodimeric STIM2.1 CAD is incapable of gating ORAI1, heterodimers with STIM1 are still able to interact with and activate ORAI1. However, these heterodimers abolished cross-linking and subsequent clustering of ORAI1 suggesting that STIM2.1 acts as a modulator of SOCE, which prevents excessive Ca^{2+} influx [Yandong Zhou et al. 2018]. The eight amino acid stretch within STIM2.1 decreases α-helicity of the CC region while increasing the exposed hydrophobicity implying that STIM2.1 interferes with the gating of ORAI1 by disrupting the coupling with the C-terminal helices of ORAI1 [Chung et al. 2018]. STIM2.1 is highly expressed in muscle cells regulating MEF2C- and NFAT4-mediated myogenesis by controlling cell cycle arrest through SOCE inhibition [Kim et al. 2019]. In STIM2.3, splice insertion of a 36 bp long exon between the exons 12 and 14 leads to a premature stop resulting in a C-terminal truncated protein, which is similar to the splice event of STIM1B. The novel and hitherto uncharacterized STIM2 variant STIM2.3 lacks the microtubule-associated EB binding sites, the S_n/P_n rich region and the PBD. In contrast to the shorter STIM1B, STIM2.3 contains its own polyadenylation site generating an alternate 3' UTR.

1.5 Aim

The family of STIM splice variants is constantly growing, and their functions are highly diverse, demonstrating that STIM proteins are involved in many processes besides the canonical SOCE pathway. The aim of this work is the characterization of the hitherto not investigated and novel STIM2 splice variant STIM2.3 to extent the so far obtained results of a previous master thesis [Poth 2018] and to understand the molecular mechanisms of differential compositions of SOCE. Analysis of postmortem human brain regions was performed to provide information about the *in vivo* expression of STIM2.3. Further functional characterization of the novel variant included Ca^{2+} imaging, localization, and cluster formation analysis. Additionally, different mutants were generated to elucidate the importance of the C terminus in regulating STIM2 function. Validation of already known interaction partners, the impact of STIM2.3 on NFAT translocation as well as RNA Seq analysis of a stable cell line should provide first indications about the potential physiological function of the C-terminally truncated STIM2.3.

The results of this thesis constitute the majority of the figures and content of the submitted manuscript: Poth, V., Do, H. T. T., Foerderer, K., Tschernig, T., Alansary, D., Helms, V., & Niemeyer, B. A. (2023). A better brain? Alternative spliced STIM2 in hominoids arises with synapse formation and creates a gain-of-function variant. *bioRxiv*, (doi:10.1101/2023.01.27.525873). The dissertation author is the first author of this publication.

2 Materials

2.1 Antibodies

Table 1 **Primary antibodies** used for Western Blot

Antigen	Manufacturer	Catalog #	clonality	Dilution
α- phospho-AMPK	Cell signaling	2535	polyclonal	1:1000
α-AMPK	Cell signaling	2532S	polyclonal	1:1000
α-β-Actin	Sigma Aldrich	A5441	monoclonal	1:5000
α-GFP D5.1	Cell signaling	2956	polyclonal	1:1000
α-HA 3F10	Roche	11867423001		1:1000
α-STIM1	Proteintech	11565-1-AP	polyclonal	1:1000
α-STIM2	Alomone	ACC-064	polyclonal	1:300

Table 2 **Secondary antibodies** used for Western Blot

Antigen	Manufacturer	Catalog#	Dilution
α-rabbit-HRP	GE Healthcare/Amersham	NA9340	1:10000
α-rat-HRP	Sigma Aldrich	A5795	1:20000
α-mouse-HRP	Amersham/Bioscience	NA931	1:5000

2.2 Bacterial strains

Table 3 **Bacterial strains**

Bacteria strain	Manufacturer
Escherichia coli XL-1 Blue Subcloning Grade	Agilent Technologies

2.3 Cell culture

2.3.1 Cell lines

Table 4 **Cell lines**

Cell line	Origin
HEK ORAI1/2/3$^{-/-}$	human embryonic kidney
HEK STIM1/2$^{-/-}$	human embryonic kidney
SH-SY5Y WT	neuroblastoma
SH-SY5Y STIM1$^{-/-}$	neuroblastoma
SH-SY5Y STIM2$^{-/-}$	neuroblastoma
SH-SY5Y STIM1/2$^{-/-}$	neuroblastoma

2.3.2 Media and transfection reagents

Table 5 **Cell culture media and supplements**

Media/Supplements	Manufacturer	Catalog #
Gibco™ DMEM	Thermo Fisher Scientific	11965084
Gibco™ MEM	Thermo Fisher Scientific	11935046
Gibco™ DMEM/F12	Thermo Fisher Scientific	10565018
FCS	Sigma Aldrich	F6765-500ML
Gibco™ MEM NEAA (100x)	Thermo Fisher Scientific	11140050

Table 6 **Transfection reagents**

Transfection reagent	Manufacturer	Catalog #
Opti-MEM	Life Technologies	11058021
JetPrime®	Polyplus Transfections	101000015
JetOptimus®	Polyplus Transfections	101000025

2.4 Chemicals

Table 7 **Chemicals**

Chemical	Manufacturer	Catalog #
2-Propanol	Sigma Aldrich	19516
6-Bnz-cAMP	BioLog	B 079-01
Acrylamid-Bisacrylamid	Sigma Aldrich	A7168
Agar Select	Sigma Aldrich	A5054
Agarose broad range	Roth	T846.3
Agarose GTQ	Roth	6352.4
Albumin, Bovine Serum	Sigma Aldrich	A6003
Ampicillin	Sigma Aldrich	A9393
APS	Sigma Aldrich	248614-56
BDNF	Preprotech	450-02
Brom phenol blue, sodium salt	Roth	A512.1
Calcium chlorid	Merck	102382
cOmplete Protease inhibitor	Roche	5892791001
DDM	Sigma Aldrich	850520P
DMSO	Sigma Aldrich	D8418
dNTP mix	VWR	733-1363
EDTA	Sigma Aldrich	ED2SS
EGTA	Sigma Aldrich	E4378.2506
FACSClean solution	BD Bioscience	340345
Fura2-AM	Invitrogen	F1221
Glycine	Applichem	R030
HEPES	Sigma Aldrich	H7523
Hoechst 3342	Thermo Fisher Scientific	62249
Ionomycin	Calbiochem	407950
Kanamycin solution	Sigma Aldrich	K0254-20ML
Magnesium chloride	Merck	105833025
Methanol	Fisher Chemicals	M3950

Chemical	Manufacturer	Catalog #
PeqGREEN DNA Dye	peqLAB	732-2960
PF- 0495732	MCE Medical Chem Express	HY-15426
Poly-L-lysine	Sigma Aldrich	P2636-25MG
Potassium chloride	AnalaR	26764.298
Retinoic acid	Sigma Aldrich	R2625
Skimmed milk powder	Sucofin	Edeka
Sodium-dodecyl-sulfate (SDS)	Acrosorganics	327315000
Sodium azide	Sigma Aldrich	S8032
Sodium chloride	Sigma Aldrich	S9888
TEMED	Sigma Aldrich	T9281
Thapsigargin	Invitrogen	T7458
Triton X-100	Eurobio	18774
Trizma	Sigma Aldrich	T1503
TRIzol	Life Technologies	15596018
Trypsin	Thermo Fisher Scientific	25300-062
Trypton	Sigma Aldrich	T9410
Tween20	Sigma Aldrich	P1379
Yeast extract	Difco	212750

2.5 Consumables

Table 8 **Consumables**

Consumable	Manufacturer	Catalog #
6x Loading Dye	Thermo Fisher Scientific	R0619
Anti-HA agarose	Thermo Fisher Scientific	26181
Coverslips, 12 mm and 25 mm	ORSATec/Kindler	02R1215-D
electroporation cuvettes	BioBudget	75-02-SE
Gel blotting paper	GE Healthcare	10426981
nitrocellulose membrane	Amersham	10600016
PVDF membrane	Merck Millipore	IPVH0010
silicon paste, high viscosity	Roth	0857.1
single-use pipettes	BioBudget	75-50-PP

2.6 Enzymes

Table 9 **Enzymes**

Enzyme	Manufacturer	Catalog #
Antarctic Phoshatase	NEB	M0289S
DreamTaq Green PCR Master Mix (2x)	Thermo Fisher Scientific	K1081
Phusion polymerase	Finnzymes	F-530S
T4 DNA ligase	Finnzymes	M0202S
Superscript II RT	Life Technologies	18064
DpnI	NEB	R0176S

2.7 Kits

Table 10 **Kits**

Kit	Manufacturer	Catalog #
Clarity Western ECL	BioRad	1705060
GeneJet Plasmid Miniprep Kit	Thermo Fisher Scientific	10242490
HiSpeed Plasmid Maxiprep Kit	Qiagen	12663
Pierce BCA Protein Assay Kit	Thermo Scientic	10741395
QIAquick Gel extraction Kit	Qiagen	28706
QuantiTect SYBR Green PCR Kit	Qiagen	204145
Zombie NIR Fixable Viability Kit	Biolegend	432105
QIAamp DNA Blood Mini Kit	Qiagen	51106

2.8 Laboratory devices

2.8.1 Axio Observer 7

Table 11 **Axio Observer 7**

Component	Manufacturer
Axio Observer A1	Zeiss
Light source: HXP 120V	Leistungselektronik JENA
filter set 21HE	Zeiss
filter set 38HE	Zeiss
filter set 46HE	Zeiss
Prime 95B sCMOS camera	Photometrics

2.8.2 Ca^{2+} Imaging

Table 12 **Ca^{2+} imaging**

Component	Manufacturer
filter set Fura2 F76-512	Analysetechnik AG
filter set YFP F36-528	Analysetechnik AG
filter set mCherry F20-451	Analysetechnik AG
Imago CCD Camera Andor Clara	Till Photonics
Imaging Control Unit ICU	Till Photonics
Monochromator Polychrome V	Till Photonics
Observer.A1	Zeiss
Transmitted Light source	Till Photonics

2.8.3 Cell Observer

Table 13 **Cell observer**

Component	Manufacturer
Camera Evolve 512	Photometrics
CO_2 Module	Zeiss
Control Unit SMC 2009	Zeiss
filter set 46HE	Zeiss
filter set 63HE	Zeiss
Heating Unit XLS	Zeiss
LED light source Colibri	Zeiss
Observer.A1	Zeiss
Power Supply 231	Zeiss
TempModuleS	Zeiss

2.8.4 TIRF

Table 14 **TIRF**

Component	Manufacturer
HCX Plan Apo oil objective 100x	Leica
Leica AM TIRF MC System	Leica
wide band supression filter525/50	Leica
wide band supression filter600/40	Leica

2.8.5 Additional devices

Table 15 **Additional devices**

Component	Manufacturer
Amaxa® Nucelofector II®	Lonza
Back-Ups 1400 Akku	APC
Bio-Photometer	Eppendorf
Centrifuge 5415C	Eppendorf
Centrifuge Mikro 220R	Hettich
Centrifuge Mini Spin 5452	Eppendorf
Centrifuge Universal 32 R	Hettich
ChemiDoc™ XRS	BioRad
FACSVerse	BD Bioscience
Gel electrophoresis Mini Protean Tetra Cell	BioRad
Heating Block	Bioer
Incubator Heracell 150i	Thermo Fisher Scientific
Incubator Hereaus	Thermo Fisher Scientific
Incubator shaker Minitron CH-4103	Infors HT
Incubator shaker Unimax 1010	Heidolph
Infinite M200 Plate Reader	Tecan
Mastercycler Personal 5332	Eppendorf
Microscope Ax10	Zeiss
NanoDrop One Microvolume UV-Vis spectrophotometer	Thermo Fisher Scientific
Power supply Power Pac HC	BioRad

Component	Manufacturer
SE260/SE250 MiniVertical Electrophoresis System Plates	Cytiva
Sterile bench HERAsafeKS	Thermo Fisher Scientific
Sterile bench KS12	Thermo Fisher Scientific
Sub-cell agarose gel electrophoresis systems	BioRad
Thermocycler, PeqSTAR	VWR Peqlab
Vortex thriller	Peqlab
Water bath A100	Lauda

2.9 Oligonucleotides

Table 16 **Oligonucleotides**

Primer	Target	Sequence
BAN426	ORAI3 rev	CACAGCCTGCAGCTCCC
BAN608	hSTIM2 1140 for	GGTGATGCCCAGAGTCTCCATT
BAN609	hSTIM2 1537 for	TCATTAGCCAGAAGCAGCAGCC
BAN610	hSTIM2 887 for	ATGCAAAGGAGGAGGCTTGTCG
BAN675	ORAI2 rev	CAAGACCTGCAGGCTGCG
BAN794	STIM2 1984	GTTGCCCTGCGCTTTATCGA
BAN828	STIM2.1	CTTAGATTTCTTCTTAAAAAGGC
BAN986	STIM1 for	atcgcCACCATGGATGTATGCGTCC
BAN1024	STIM1 for	ATGGATGTATGCGTCCGTCTTGCCCTG
BAN1433	pMAX for	GATATCTCGAGCTCGATGAGTTTG
BAN1435	ORAI1 rev	GGCATAGTGGCTGCCGG
BAN1485	hSTIM2 rev	ctaggttctagaTCACTTAGATTTCTTCTTAAAAAGGC
BAN1546	EGFP/mCherry rev	TTACTTGTACAGCTCGTCCATG
BAN1570	hSTIM2 200 rev	AGTTTTTGTCTGTGACTCCG
BAN1587	QC Δ5K for	GCCATCAAAAATCAAAAGCCTTTGAAAGAAGAAATCTAAGTGAAACCCAG
BAN1588	QC Δ5K rev	CTGGGTTTCACTTAGATTTCTTCTTTCAAAGGCTTTTGATTTTTGATGGC
BAN1661	QC for I775N/P776N	GAACCAGCTTTCCAGTGGCAACAACGTGCCTAAACCTCGCCACAC
BAN1662	QC rev I775N/P776N	GTGTGGCGAGGTTTAGGCACGTTGTTGCCACTGGAAAGCTGGTTC
BAN1706	STIM1 5'UTR	AAACTTGGAGCACTTGACCTTTG
BAN1708	STIM1 ex1 rev	AGATTTCAACTTGCCCACTTC
BAN1709	STIM2 ex1 for	GGACGGATGCGAGCTTGT
BAN1710	STIM2 intr1 rev	AGATGCTGACCTCTGCACG
BAN1719	mKate for	ATGGTGAGCGAGCTGATTAAG
BAN1720	mKate rev	TCTGTGCCCCAGTTTGCTAG
BAN1752	STIM2 CEV for	TGCGAGCTTGTGCCCCG
BAN1846	QC for I807N/P808N	GTGTTGCCAGAATAAGCAGCAACAACCATGACCTTTGTCATAATGGAG
BAN1847	QC rev I807N/P808N	CTCCATTATGACAAAGGTCATGGTTGTTGCTGCTTATTCTGGCAACAC
BAN1858	STIM1 SP rev	GAGGCTCTGGCCCTGGTGC

Primer	Target	Sequence
BAN1999	half HA STIM2 for	*GTACCGGATTACGCCGGCGGC*TGCGAGCTTGTGCCCCG
BAN2003	half HA STIM2 rev	*GTCATATGGGTAgccgcc*GAGGCTCTGGCCCTGGTGC
BAN2034	YFPn rev	cgccggtaccTAGCCCAGAAGACAGTGGAG
BAN2046	linker YFPn/c for	GGATCCTCTAGAGTCGACG
BAN2048	STIM2.3 rev	TTCACTTTTGCACGCACCga
BAN2287	Δ711 rev	CTTTCGCGGAGATAATGTTTG
BAN2289	Δ711 for	TGAAACCCAGCTTTCTTGTAC
BAN2297	Δ675-710 for	TTGCTTTTCAGCAGAGAAGTAAAT
BAN2298	Δ675-710 rev	AAGATATCAAGAGATGAGGTGT

Table 17 **qRT-PCR oligonucleotides**

Target	Primer forward	Primer reverse
CACNA1B	Hs_CACNA1B_1_SG / QT00077042	
CACNA1C	Hs_CACNA1C_1_SG / QT00053480	
CACNA1D	Hs_CACNA1D_1_SG / QT00076657	
CACNA1G	Hs_CACNA1G_1_SG / QT00043043	
hSTIM1	Hs_STIM1_1_SG / QT00083538	
hSTIM2	Hs_STIM2_1_SG / QT00023744	
hSTIM2.3	GAGCTCAGCTTGCTCCACAC	CGAGCCCAAGGTGAATACAT
ORAI1	ATGAGCCTCAACGAGCACT	GTGGGTAGTCGTGGTCAG
ORAI2	TGGAACTGGTCACCTCTAAC	GGGTACTGGTACTGCGTCT
ORAI3	GTACCGGGAGTTCGTGCA	GGTACTCGTGGTCACTCT
TBP	Hs_TBP_1_SG / QT00000721	

2.10 Plasmids

Table 18 **Plasmids**

Construct	Fluorescent marker	Vector
HA-STIM2.2	-	pEX-SP1
HA-STIM2.3	-	pEX-SP1
mKate2-STIM2.2	mKate2, N-term	pEX-SP1
mKate2-STIM2.3	mKate2, N-term	pEX-SP1
mCherry-STIM1	mCherry, N-term	pEX-SP1
STIM2.2-mCherry	mCherry, C-term	pEX-SP1
YFP-STIM2.2	YFP, N-term	pEX-SP1
YFP-STIM2.3	YFP, N-term	pEX-SP1
YFP-STIM2.2Δ5K	YFP, N-term	pEX-SP1
YFP-STIM2.2Δ674	YFP, N-term	pEX-SP1
YFP-STIM2.2 I775N/P776N	YFP, N-term	pEX-SP1
YFP-STIM2.2 I807N/P808N	YFP, N-term	pEX-SP1

Construct	Fluorescent marker	Vector
YFP-STIM2.2 2xIP	YFP, N-term	pEX-SP1
YFP-STIM2.2 2xIP+Δ5K	YFP, N-term	pEX-SP1
YFP-STIM2.2Δ711	YFP, N-term	pEX-SP1
YFP-STIM2.2Δ675-710	YFP, N-term	pEX-SP1
YFP-STIM2.2Δ675-710+2xIP	YFP, N-term	pEX-SP1
YFP-STIM2.2Δ675-710+2xIP+Δ5K	YFP, N-term	pEX-SP1
ORAI1 TCM	IRES RFP	pCAGGS
NFAT1-GFP	GFP	pCAGGS
HA-STIM2.2-YFPc	HA, N-term; YFPc, C-term	pEX-SP1
STIM2.2-YFPn	YFPn, C-term	pBabe
HA-STIM2.3-YFPc	HA, N-term; YFPc, C-term	pEX-SP1
STIM2.3-YFPn	YFPn, C-term	pBabe
STIM1-YFPn	YFPn, C-term	pBabe
ORAI1-YFPn	YFPn, C-term	pMax
ORAI2-YFPn	YFPn, C-term	pMax
ORAI3-YFPn	YFPn, C-term	pMax
EFEMP1-YFPn	YFPn, C-term	pBabe
Syt2-YFPn	YFPn, C-term	pBabe
TRPC1-YFPn	YFPn, C-term	pBabe
TRPC5-YFPn	YFPn, C-term	pBabe
FLOT1-YFPn	YFPn, C-term	pBabe
SOD1-YFPn	YFPn, C-term	pBabe
PDE8B-YFPn	YFPn, C-term	pBabe
CACNA1C-YFPn	YFPn, C-term	pBabe
YFP-STIM1	YFP, N.term	pMAX
YFP-STIM1B	YFP, N.term	pMAX
STIM1-mCherry	mCherry, C-term; HA, N-term	pMAX
STIM1A-mCherry	mCherry, C-term; HA, N-term	pMAX
STIM1ΔKK-mCherry	mCherry, C-term; HA, N-term	pMAX
STIM1AΔKK-mCherry	mCherry, C-term; HA, N-term	pMAX

2.11 Size standards

Table 19 **Size standards**

Size standard	Manufacturer	Catalog #
100 bp DNA ladder	NEB	N3231S
1kb plus DNA ladder	Thermo Fisher Scientific	10787-018
Precision Plus Protein Dual Color Standard	BioRad	1610394
Spectra™ Multicolor Broad Range Protein Ladder	Thermo Fisher Scientific	26623

2.12 Software

Software	Manufacturer
Application Suite Advanced Fluorescence	Leica
Axio Vision	Zeiss
Benchling	
CorelDraw X4	Corel Corporation
Excel	Microsoft
FACSSuite	BD Bioscience
FIJI	
FlowJo	BD Bioscience
GraphPad Prism 9	Graph Pad Software
Image Lab	BioRad
Mendeley	Elsevier
PowerPoint	Microsoft
VisiView	Visitron
Word	Microsoft
Zen	Zeiss

2.13 Solutions

2.13.1 Ca^{2+} Ringer solutions

0-2 mM Ca^{2+} ringer

145	mM	NaCl
4	mM	KCl
10	mM	HEPES pH 7.4
10	mM	Glucose
2	mM	$MgCl_2$
0/0.5/1/2	mM	$CaCl_2$

310 mosm; pH 7.4 adjusted with NaOH

100 mM K^+ in 1.5 mM Ca^{2+} ringer

49	mM	NaCl
100	mM	KCl
10	mM	HEPES pH 7.4
10	mM	Glucose
2	mM	$MgCl_2$
1.5	mM	$CaCl_2$

310 mosm; pH 7.4 adjusted with NaOH

2.13.2   SDS-PAGE and Western Blot solutions

Blocking buffer (in TBST)

5	%	Skimmed milk

Blotting buffer pH 8.3

20	%	Methanol
1	%	SDS
250	mM	Tris-HCl
1.92	M	Glycine

IP wash buffer pH 7.4

20	mM	Tris pH 7.4
100	mM	KCl
10	%	Glycerol
0.05	%	DDM

IP lysis buffer pH 7.4

20	mM	Tris pH 7.4
100	mM	KCl
10	%	Glycerol
0.1	%	DDM

Laemmli buffer 5x

125	mM	Tris pH 6.8
2.5	%	SDS
0.1	%	Brom phenol blue
60	%	Glycerine
25	%	β-Mercaptoethanol

Primary antibody solution (in PBS)

1	%	BSA
0.02	%	Sodium azide

RIPA lysis buffer pH 7.4

10	mM	Tris pH 7.4
1	%	Triton X-100
0.5	%	NP40
150	mM	NaCl

SDS electrophoresis buffer 10x

250	mM	Tris base
1	%	SDS
1.92	M	Glycine

Secondary antibody solution (in TBST)

5	%	Skimmed milk

Separation gel buffer pH 8.8

1.6	M	Tris-HCl
0.4	%	SDS

Stacking gel buffer pH 6.8

0.5	M	Tris-HCl
0.4	%	SDS

TBS 10x

500	mM	Tris base
1.5	M	NaCl

TBST pH 7.5

10	%	TBS
0.1	%	Tween

2.13.3   Additional solutions

FACS buffer pH 8.3 (in PBS)

5	%	FCS
0.5	%	BSA
0.07	%	NaN_3

LB medium pH 7.5

1	%	Select Peptone or Tryptone
1	%	Select Peptone or NaCl
0.5	%	Yeast Extract
100	µg/ml	Ampicillin /
60	µg/ml	Kanamycin
1.5	**%**	**Select Agar (LB agar plates)**

TBE 10x

10	mM	EDTA
89	mM	Tris base
89	mM	Boric acid

CHAPTER 3

3 Methods

3.1 Cell culture and transfection

3.1.1 Cell lines

Cell lines were cultured at 37 °C, 5 % CO_2 in a humidified incubator in their respective medium supplemented with 10 % fetal calf serum (FCS). Adherent cells were passaged twice weekly and detached using 0.05 % trypsin + 1x EDTA (Gibco). Cell passaging and experimental preparation was performed under a sterile cell culture bench with laminar air flow. Cell lines used and their respective medium are listed in Tab. 21.

Table 21 **Culture conditions**

Cell line	Medium	Supplements
HEK STIM1/2$^{-/-}$	DMEM	10 % FCS
HEK ORAI1/2/3$^{-/-}$	MEM	10 % FCS
SH-SY5Y WT	DMEM	10 % FCS + 1 % NEAA
SH-SY5Y STIM1$^{-/-}$	DMEM	10 % FCS + 1 % NEAA
SH-SY5Y STIM2$^{-/-}$	DMEM	10 % FCS + 1 % NEAA
SH-SY5Y STIM1/2$^{-/-}$	DMEM	10 % FCS + 1 % NEAA

3.1.2 Transfection

Transfection describes the introduction of foreign DNA into a cell. While transiently transfected cells only express the DNA of interest for a restricted time period, stably transfected cells integrated the foreign DNA into their genome.

Electroporation

During electroporation, the plasma membrane is briefly permeabilized by electrical impulses allowing foreign DNA being absorbed into the cell.

For imaging experiments, HEK STIM1/2$^{-/-}$ and HEK ORAI1/2/3$^{-/-}$ were detached using trypsin and $2x10^6$ cells/transfection were centrifuged at 1300 rpm for 5 min. The pellet was resuspended in 100 µl Opti-MEM (Gibco) and 1 µg DNA was added. Cells were transfected via electroporation using the program Q-001 of the Amaxa Nucleofector II (Lonza) according to the manufacturer's protocol. After the addition of 400 µl medium, transfected cells were seeded onto 25 mm coverslips in 35 mm dishes containing

medium and incubated at 37 °C and 5 % CO$_2$. Cells were analyzed 24 hours post transfection.

Lipofection

During lipofection, the foreign DNA is encapsuled in liposomes after incubation with lipophilic agents and integrated into the cell via endocytosis.

For imaging experiments, SH-SY5Y STIM2$^{-/-}$ and STIM1/2$^{-/-}$ cells were seeded into 35 mm dishes containing DMEM + 10 % FCS + 1 % NEAA 24 hours prior to transfection using JetPrime (Polyplus) reagent according to the manufacturer's protocol. 5 hours after the transfection, cells were re-seeded onto 25 mm coverslips in 35 mm dishes containing medium and analyzed after 24 hours. For co-immunoprecipitation (Co-IP) and bimolecular fluorescence complementation (BiFC), HEK STIM1/2$^{-/-}$ cells were seeded into 60 mm dishes or 6-well plates containing DMEM + 10 % FCS 24 hours prior to transfection using JetOptimus (Polyplus) reagent according to the manufacturer's protocol, respectively. Cells were analyzed 24 hours post transfection. The transfection conditions are listed in Tab. 22.

Table 22 **Transfection conditions**

Cell line	Experiment	Reagent	Method
HEK STIM1/2$^{-/-}$	Ca^{2+} imaging	Opti-MEM	electroporation
HEK STIM1/2$^{-/-}$	Imaging/BiFC/Co-IP	JetOptimus	lipofection
HEK ORAI1/2/3$^{-/-}$	Ca^{2+} imaging	Opti-MEM	electroporation
SH-SY5Y STIM1$^{-/-}$	Ca^{2+} imaging/NFAT assay	JetPrime	lipofection
SH-SY5Y STIM2$^{-/-}$	Ca^{2+} imaging	JetPrime	lipofection
SH-SY5Y STIM1/2$^{-/-}$	Ca^{2+} imaging/NFAT assay	JetPrime	lipofection

3.1.3 Generation of clonal cell lines

The CRISPR/Cas9 system, originally from bacteria, is a suitable tool for targeted genome editing in eukaryotic cells. The endonuclease Cas9 recognizes DNA sequences within the genome by binding of the guide RNA (gRNA), which is complementary to the targeted sequence of a gene. The artificially induced double-strand break is repaired by non-homologous end-joining leading to deletion, insertion or exchange of single bases. Due to a frameshift or stop codon, the edited gene is no longer translated into the functional protein.

The generation of SH-SY5Y STIM1 and/or STIM2 knockout cell lines using CRISPR/Cas9 was started by the group of Markus Grimm.

To generate clonal cell lines, SH-SY5Y STIM1$^{-/-}$ and/or STIM2$^{-/-}$ cells were detached using trypsin, resuspended in DMEM + 10 % FCS + 1 % NEAA and diluted to a final concentration of 5 cells/ml. After pipetting 100 µl medium into 96-well plates, 100 µl of the cell suspension was added to each well and the plates were incubated at 37 °C and 5 % CO_2. After 24 hours, each well was microscopically analyzed ensuring only one cell/well was present. After the cells started to grow into larger clusters, all the cells from each well were transferred into the next larger well plates until finally transferred into small cell culture flasks and regular passaging. The knockout of STIM1 and/or STIM2 in the individual clonal cell lines was confirmed by performing a PCR on genomic DNA (gDNA) using primers flanking the binding region of the gRNAs followed by sequencing of the obtained PCR product. gDNA was isolated using the QIAmp DNA Blod Mini Kit (Qiagen) according to the manufacturer's protocol. Western Blot analysis was used to confirm the knockout on protein level.

3.1.4 Generation of stable cell lines

To generate cell lines stably expressing HA-STIM2.2 or HA-STIM2.3, SH-SY5Y STIM2$^{-/-}$ cells were detached using trypsin and seeded into 60 mm dishes containing DMEM + 10 % FCS + 1 % NEAA 24 hours prior to transfection using JetPrime according to the manufacturer's protocol. 24 hours post transfection, medium was changed to DMEM + 10 % FCS + 1 % NEAA + 1 mg/ml G418 as the selection antibiotic. The selection medium was changed regularly until constant growing was observed. The sensitivity of SH-SY5Y STIM2$^{-/-}$ cells to G418 was determined beforehand using different concentrations ranging from 0.1 – 1 mg/ml G418 on untransfected cells. The stable over-expression of HA-STIM2.2 or HA-STIM2.3 was analyzed using Ca^{2+} imaging and Western Blot.

3.1.5 Differentiation of SH-SY5Y

The neuroblastoma cell line SH-SY5Y can be differentiated to a more mature neuronal-like phenotype using serum deprivation, retinoic acid (RA), and the neurotropic factor BDNF [Pezzini et al. 2017]. SH-SY5Y cells were seeded onto 25 mm coverslips coated with Poly-L-lysine in 6-well plates containing DMEM + 10 % FCS + 1 % NEAA and incubated at 37 °C and 5 % CO_2. After 24 hours, confluency should not exceed 60 % of the total area. For differentiation, medium was exchanged to DMEM/F12 + 1 % FCS +

10 µM RA and medium change was performed every second day. On day 7, medium was changed to DMEM/F12 + 1 % FCS + 50 ng/µl BDNF for additional two days (Fig. 5). After a total period of 9 days, cell differentiation was analyzed using Ca^{2+} imaging.
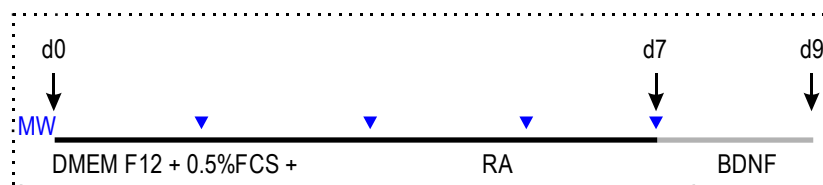
Figure 5 Differentiation protocol for SH-SY5Y cells. Blue arrow heads indicate timepoints of medium exchange every second day. Black arrows indicate number of days.

3.2 Recombinant DNA techniques

3.2.1 Polymerase chain reaction

The polymerase chain reaction (PCR) is used for targeted amplification of specific DNA regions in several temperature-dependent cycles. First, hydrogen bonds of the double stranded DNA are denatured using high temperature leading to two single stranded DNA molecules. During the subsequent annealing phase, oligonucleotides (primers) bind to the single stranded DNA at lower temperatures. Oligonucleotides are short synthetic single stranded DNA sequences that are complementary to the start and end of the targeted region. The optimal temperature during the annealing phase is dependent on the length and nucleotide composition of the primers and can be determined using the Wallace rule. During the elongation phase, the DNA polymerase binds to the 3' end of each primer and synthesizes the complementary strand in 3'-5' direction using free deoxynucleotides. The temperature used during this step is determined by the optimum activity temperature of the DNA polymerase and the elongation time by the length of the amplified region. These steps are repeated for several cycles leading to exponential amplification of a specific DNA region. The DreamTag Green DNA-Polymerase Master Mix was used for diagnostic PCRs and the high fidelity Phusion polymerase was used for cloning PCRs. The conditions for PCR reactions and protocols are listed in Tab. 23- 26.

Table 23 **Diagnostic PCR reaction**

Volume (µl)	
0.5 - 2	DNA
2.5	Primer forw. (10 pmol/µl)
2.5	Primer rev. (10 pmol/µl)
25	DreamTag Green Master Mix
Ad 50	$H_2O_{dest.}$

Table 24 **Diagnostic PCR protocol**

Temperature (°C)	Time (s)	Cycles
95	60	
95	30	
58	30	35x
72	1 kb/min	
72	600	
16	store	

Table 25 **Cloning PCR reaction**

Volume (µl)	
x	DNA (10ng)
1	Primer forw. (10 pmol/µl)
1	Primer rev. (10 pmol/µl)
1	dNTPs
10	HF/GC buffer (5x)
0,25	High fidelity Phusion polymerase
Ad 50	$H_2O_{dest.}$

Table 26 **Cloning PCR protocol**

Temperature (°C)	Time (s)	Cycles
98	60	
98	30	
58-62	30	35x
72	2 kb/min	
72	600	
16	store	

Site-directed mutagenesis

The site-directed mutagenesis is a PCR-based method for the targeted deletion, insertion, or exchange of one or several amino acids within a plasmid DNA. The desired mutation is inserted via two complement oligonucleotides spanning the mutation site. After amplification of the entire plasmid, the template DNA is digested using DpnI. The mutated plasmid is transformed into competent bacterial cells and the success of the site-directed mutagenesis was confirmed by sequencing. The PCR reaction and condition are listed in Tab. 25 and 27.

Table 27 **Site-directed mutagenesis PCR conditions**

Temperature (°C)	Time (s)	Cycles
98	60	
98	30	
58-62	60	17x
72	2 kb/min	
72	600	
16	store	

3.2.2 Colony PCR

Colony PCR is used for a wide screening of possible positive transformed bacterial clones containing the vector with the correct oriented insert. A small amount of the bacterial clone is picked with a sterile pipette tip and used directly as the template in the PCR reaction. During the initial phase, the high temperature leads to release of the bacterial DNA. To confirm the correct orientation of the insert, one primer is usually complementary to the vector sequence and the other one to the insert sequence. The colony PCR reaction and condition are listed in Tab. 28 and 23 (3.2.1).

Table 28 **Colony PCR reaction**

Volume (µl)	
-	DNA (bacterial clone)
1	Primer forw. (10 pmol/µl)
1	Primer rev. (10 pmol/µl)
10	DreamTaq™ Green PCR Mastermix
Ad 20	$H_2O_{dest.}$

After identification of correct clones, 5 ml LB media cultures were inoculated for further amplification of the plasmid (3.2.7).

3.2.3 Restriction

Restriction enzymes are originally found in bacteria as their native defense mechanism against invading viruses. Restriction enzymes cut the phosphodiesterase bonds of DNA at short specific palindromic sequences leading to either blunt ends or sticky ends with short single stranded DNA overhangs. The restriction enzyme DpnI recognizes methylated DNA allowing digestion of the methylated template DNA after amplification of an entire plasmid. DpnI is directly added to the PCR reaction and incubated at 37 °C for 90 min. All other restriction enzymes require specific buffer conditions. The restriction digestion reaction is listed in Tab. 29.

Table 29 **Restriction digestion reaction**

Volume (µl)	
X	DNA (1-2 µg)
1	restriction enzyme I
1	restriction enzyme II (optionally)
3	buffer (10x)
ad 30	H_2O

Incubation at 37 °C for 15-60 min
Optionally: heat inactivation at 80 °C for 20 min

3.2.4 Gel electrophoresis

Gel electrophoresis is a method used for separation of DNA fragments according to their size. Due to the negatively charged phosphate backbone, DNA fragments migrate within an electrical field towards the positively charged anode. The pore size of the gel is determined by the amount of agarose used, a poly saccharide consisting of D-galactose and 3.6-anhydro-L-galactose. While low-percentage gels are suitable for separating larger DNA fragments, high-percentage ones are used for separating smaller fragments. To determine the size of the fragments, a DNA size standard is used.

For diagnostic and colony PCRs, 1-1.5 % agarose gels were used. For cloning PCRs and restriction digestion reactions, 0.8-1 % GTQ (Gen technology quality) gels were used, which allow re-isolation of the DNA for further processing. The DNA was further isolated using the QIAquick Gel Extraction Kit according to the manufacturer's protocol.

3.2.5 Phosphorylation/Dephosphorylation

To avoid re-ligation of the vector after restriction digestion, the 5' phosphate of the vector backbone can be removed to increase uptake of the insert. Additionally, ligation efficacy can be increased by phosphorylation of the 5' end of the insert if the phosphate was not added via phosphorylated primers or sticky ends after restriction digestion. The dephosphorylation and phosphorylation conditions are listed in Tab. 30.

Table 30 **Dephosphorylation and phosporylation reaction**

dephosphorylation		phosphorylation	
Volume (µl)		Volume (µl)	
x	vector DNA	x	insert DNA
1	phosphatase (rSAP)	1	kinase (T4 PNK)
3	Cutsmart buffer	2	ligase buffer (T4)
ad 30	H_2O	ad 20	H_2O

3.2.6 Ligation

Ligation is the final step of generating recombinant DNA by connecting the insert DNA with the compatible vector backbone. The enzyme ligase catalyzes the formation of phosphodiester bonds covalently connecting the 3' hydroxy group with the 5' phosphate end. The obtained recombinant DNA can be directly used for transformation of competent bacteria. During ligation, a molar ratio of 3:1 insert:vector not exceeding 100 ng in total DNA amount is used. The ligation reaction is listed in Tab. 31.

Table 31 **Ligation reaction**

Volume (µl)	
x	vector DNA
x	insert DNA
1	T4 ligase
1.5	T4 ligase buffer (10x)
ad 15	H_2O

Incubation 16 °C over night (1 hour at RT)

3.2.7 Heterologous expression and DNA isolation

Heat shock transformation of competent bacteria

Transformation describes the absorption of non-viral foreign DNA into chemically competent bacteria. The chemical competency is achieved by treatment of the bacterial cells with potassium or magnesium chloride during the log phase of growth. During a

heat shock at 42 °C for 90 s, lipids from the bacterial membrane are released causing pores within the membrane. Additional transiently depolarization of the bacterial membrane allows the foreign DNA to enter the cell. The membrane is restored by incubation of 2 min on ice. After addition of 1 ml LB medium, the transformed bacteria were incubated at 37 °C for one hour on a shaker. The bacterial cells were plated onto LB agar plates containing the respective selection antibiotic and incubated at 37 °C over night.

Plasmid preparation

Depending on the culture volume, DNA was isolated using either the GeneJet Plasmid Mini Prep Kit for 5 ml cultures or the QIAprep Spin Maxi Prep Kit for 200 ml cultures according to the manufacturer's protocol. After addition of the respective selection antibiotic, the desired volume of LB medium was inoculated with one bacterial colony and incubated at 37 °C over night for ~ 16 hours. The principle of the GeneJet Plasmid Mini Prep Kit relies on alkaline lysis and binding of the released DNA onto a silica gel column under high salt buffer conditions. After two washing steps, the DNA is eluted using H_2O_{dest}. The principle of the QIAprep Spin Maxi Prep Kit relies on alkaline lysis followed by binding of the DNA to an anion exchange membrane under low salt conditions. The DNA is eluted from the membrane using a high salt buffer, precipitated using isopropanol and finally eluted in TE buffer. DNA concentration was measured using the NanoDrop One.

3.2.8 Cloned plasmids

In this thesis, several constructs have been cloned and verified via sequencing performed by SEQLAB (Göttingen). All cloned plasmids are listed in Tab. 32 including the construct, vector and strategy used for cloning.

Table 32 **Cloned plasmids**

Construct	Vector	Strategy
HA-STIM2.2	pEX	BAN1999+BAN2003
HA-STIM2.3	pEX	BAN1999+BAN2003
HA-STIM2.2-YFPc	pEX	BAN1546+BAN2046
HA-STIM2.3-YFPc	pEX	BAN1546+BAN2046
YFP-STIM2.2 I775N/P776N	pEX	BAN1661+BAN1662
YFP-STIM2.2 I807N/P808N	pEX	BAN1846+BAN1847
YFP-STIM2.2 2xIP	pEX	

Construct	Vector	Strategy
YFP-STIM2.2 2xIP+Δ5K	pEX	BAN1587+BAN1588
YFP-STIM2.2Δ711	pEX	BAN2287+BAN2289
YFP-STIM2.2Δ675-710	pEX	BAN2297+BAN2298
YFP-STIM2.2Δ675-710+2xIP	pEX	BAN2297+BAN2298
YFP-STIM2.2Δ675-710+2xIP+Δ5K	pEX	BAN2297+BAN2298
mKate2-STIM2.2	pEX	BAN1719+BAN1720; BAN1858+BAN1752
mKate2-STIM2.3	pEX	BAN1719+BAN1720; BAN1858+BAN1752
mKate2-STIM2.2Δ5K	pEX	BAN1719+BAN1720; BAN1858+BAN1752
mKate2-STIM2.2 2xIP+Δ5K	pEX	BAN1719+BAN1720; BAN1858+BAN1752
ORAI1-YFPn	pMax	BAN1435+BAN1433; BAN2034+BAN2046
ORAI1-YFPc	pMax	BAN1435+BAN1433; BAN1546+BAN2046
ORAI2-YFPn	pMax	BAN675+BAN1433; BAN2034+BAN2046
ORAI2-YFPc	pMax	BAN675+BAN1433; BAN1546+BAN2046
ORAI3-YFPn	pMax	BAN426+BAN1433; BAN2034+BAN2046
ORAI3-YFPc	pMax	BAN426+BAN1433; BAN1546+BAN2046

3.3 Quantitative real-time PCR

Quantitative real-time PCR (qRT-PCR) is a sensitive method based on a classic PCR to determine the relative expression level of a gene of interest using a DNA-intercalating fluorescent dye. The isolated RNA is transcribed into cDNA, which is used as the template in the qRT-PCR.

3.3.1 RNA Isolation

The RNA isolation from primary postmortem human brain samples or cell lines was performed using TRIzol™ according to the manufacturer's protocol. A total volume of 800 µl TRIzol™ was added to either 80-100 mg tissue or 3-5x10^6 cells. The samples were stored at -80 °C until further processing. The primary postmortem human brain samples

were provided by Prof. Thomas Tschernig (Anatomy, UKS). Additional RNA of different human tissues of several donors was provided by Dr. Nicole Ludwig (Human Genetics, UdS). The concentration of the isolated RNA was measured using the NanoDrop One.

3.3.2 cDNA synthesis

The reverse transcription of RNA into complementary DNA (cDNA) was performed using the Super Script II Reverse Transcriptase according to the manufacturer's protocol. A total amount of 0.8 µg RNA/cDNA reaction was used. The cDNA was stored at -20 °C until further processing.

3.3.3 qRT-PCR

Quantitative real-time PCR is based on a conventional PCR using a fluorescent dye, which intercalates with the DNA. In each cycle the fluorescence intensity is monitored allowing proportional correlation of the fluorescence intensity to the amount of amplified DNA. The cycle threshold (Ct) value defines the cycle at which the fluorescence signal overcomes the background signal. The higher a gene is expressed, the lower the Ct value is. A constitutively expressed housekeeping gene is used to normalize the expression of different genes within a sample and to compare the expression level among different samples. The QuantiTect SYBRgreen Kit was used according to the manufacturer's protocol. TATA box binding protein (TBP) was used as a housekeeping gene to normalize the expression levels of the analyzed genes. The specificity of the amplified products was based on their melting curve verified using the BioRad CFX96 Real Time System. The qRT-PCR conditions are listed in Tab. 33. The qRT-PCR data shown in this thesis were performed by Kathrin Förderer.

Table 33 **qRT-PCR conditions**

Temperature (°C)	Time (s)	Cycles
95	900	
95	30	
58	30	45x
72	30	
95	60	
65-95	1°C/5	melting curve

3.4 RNA sequencing

RNA sequencing is based on high-throughput next-generation sequencing to analyze the whole transcriptome including all kinds of RNA and to identify differentially expressed genes (DEGs) under certain conditions. After RNA isolation, cDNA transcription and second strand cDNA (ds cDNA) synthesis, the library is prepared by fragmenting the ds cDNA using restriction endonucleases. Adapter sequences are ligated to each fragment and the entire library is purified. The individual ds cDNA fragments are sequenced and aligned to a reference genome using the STAR software. The gene expression level is calculated by the number of mapped reads, i.e. the abundance of transcripts (count of sequencing) mapped to a genome is proportional to the expression level. The gene expression unit FPKM (expected number of fragments per kilobase of transcript sequence per millions base pairs sequenced) is used to normalize counts obtained from paired-end sequencing data and considers sequencing depth and gene length on counting of fragments. To determine whether a gene is expressed, threshold was set to FPKM > 1. Differential gene expression analysis was performed using the DESeq2 R package [Anders and Huber 2010] for the analysis of two conditions or groups. For samples without biological replicates, DEG analysis was performed using the EdgeR R package. Identified DEGs are displayed as volcano plots showing up- or downregulation (log2 foldchange) on the x-axis and the significant degree of changes (-log10(padjust)) on the y-axis compared to the control group/sample. By enrichment analysis of the DEGs using the clusterProfiler software [Yu et al. 2012], associated biological functions or pathways can be identified. The Gene Ontology (GO) identifies cellular components (CC), molecular functions (MF) and biological processes (BP), which are significantly affected by the differentially expressed genes.

For RNA sequencing, RNA was isolated as described in 3.3.1 and sent to Novogene (Cambridge, UK), who performed all further steps including the bioinformatic analysis.

3.5 Protein biochemistry

3.5.1 Lysate generation

After washing adherent cells once with ice cold PBS, cells were detached in ice cold RIPA containing cOmplete protease inhibitor cocktail using a cell scraper. Cells were lysed for 5 min at -80 °C. During thawing, the cell suspension was vortexed regularly for ~10 s. To

remove cell debris, the lysate was centrifuged at 18000 g and 4 °C for 30 min and the supernatant was transferred to a fresh 1.5 ml reaction tube. The lysates were stored at -80 °C until further processing.

3.5.2 Protein concentration determination

The protein concentration was determined using the bicinoquinic acid (BCA) assay based on calorimetric detection. Bivalent copper ions (Cu^{2+}) are reduced to monovalent copper ions (Cu^+) by larger peptides under alkaline conditions in a temperature-dependent reaction. The Cu^+ is chelated by four to six peptide bonds producing a violet complex which absorbs light at 540 nm. The resulting color intensity is proportional to the protein concentration. To determine protein concentration the Pierce BCA Assay Kit was used according to the manufacturer's protocol. A BSA protein standard (0; 0.01; 0.02; 0.04; 0.06; 0.08; 0.1 mg/ml) was used. In a 96-well plate, 200 μl of the BCA reagent was mixed with 25 μl of the diluted lysate (1:100; 1:200; 1:300) or of the protein standard. The plate was incubated at 60 °C for 45 min on a shaker and the absorption was measured at 562 nm using the plate reader Tecan M200.

3.5.3 SDS-PAGE & Western Blot

Western Blot is used to analyze and detect proteins based on their molecular weight after separation and transfer to a membrane using specific antibodies.

SDS-PAGE

Sodium-dodecyl-sulfate polyacrylamide gel electrophoresis (SDS-PAGE) is used to separate proteins by their molecular weight in a vertical electrical field. By heating the protein samples at 65 °C for 15 min and adding SDS, all proteins are denatured resulting in negatively charged linearized proteins. SDS-PAGE eliminates the influence of the original protein conformation and charge leading to a separation solely based on the molecular weight. The discontinuous gel consists of a stacking and separation gel, which differ in their pH and pore size. While the stacking gel is neutral with large pore size allowing proteins to accumulate at the separation gel, the separation gel is basic with smaller pore size leading to separation of the proteins by their molecular weight. 4-5 % stacking gels and 8.5-10 % separation gels were used. The Precision Plus Protein Dual Color Standard served as a protein standard. Electrophoresis was performed using 1x

SDS as the running buffer and after the proteins entered the separation gel, a constant voltage of 150 mV was used. The compositions of the stacking and separation gels are listed in Tab. 34.

Table 34 **Composition of stacking and separation gel**

stacking gel 4% (5%)		separation gel 8.5% (10%)
Volume (ml)		Volume (ml)
1.25	buffer	2.5
0.5 (0.63)	acrylamide	2.13 (2.5)
3.21 (3.08)	H_2O	5.28 (4.91)
37.5 µl	APS	75 µl
7.5 µl	TEMED	15 µl

Western Blot

After SDS-PAGE, the separated proteins are transferred to a membrane in a horizontal electrical field. Depending on the protein size, a nitrocellulose (large proteins) or PVDF (small proteins) membrane was used. The PVDF membrane requires equilibration in methanol for 1 min before use. Blotting was performed at 0.35 mV and 4 °C for 90 min. The membrane was blocked in 5 % skimmed mild (in TBST) for one hour at room temperature (RT) to avoid unspecific binding of the antibody. Primary antibodies were incubated over night at 4 °C. After washing the membrane 3 times for 10 min in TBST, the respective secondary antibodies coupled to horseradish peroxidase were incubated in blocking buffer for one hour at RT. After washing 2 times for 10 min in TBST followed by 10 min in TBS, the antibody signal was detected using the Clarity Western ECL Kit based on chemiluminescence and the ChemiDoc™ XRS. For quantification, non-saturated signals were analyzed using the software Image Lab.

3.6 Protein interaction

3.6.1 Co-immunoprecipitation

Co-immunoprecipitation (Co-IP) is a biochemical method to identify protein-protein interactions. A specific antibody, coupled to magnetic beads or agarose, is used to enrich the protein of interest (POI) and all interacting proteins within a lysate. The POI and interacting proteins can be either endogenously expressed in cells and tissues or overexpressed coupled to a tag to facilitate precipitation. By subsequent SDS-PAGE and Western Blot, all precipitated proteins can be detected using specific antibodies. To

analyze protein-protein interactions, HEK STIM1/2$^{-/-}$ cells were transfected with HA-STIM2.2 or HA-STIM2.3 as described in 3.1.2. Cell lysis was performed using IP lysis buffer and protein concentration was determined using BCA assay. The concentration of the lysate was diluted to 3 µg/µl. For co-immunoprecipitation, 800 µg of protein and 30 µl of Anti-HA agarose were used per condition. The Co-IP was incubated over night at 4 °C end-over-end tumbling. After 4 times washing with IP wash buffer for 5 min and centrifugation at 300 g for 30 s, the bound proteins were eluted at 90°°C for 5 min using 30 µl 50 mM Tris-HCl + 2 % SDS. The entire eluate, 25 µg of input and flowthrough were analyzed on a Western Blot.

3.6.2 Bimolecular fluorescence complementation

Besides co-immunoprecipitation and FRET (Förster resonance energy transfer), bimolecular fluorescence complementation (BiFC) is also suitable to identify protein-protein interactions under more physiological conditions. The principle of BiFC is based on the complementation of a split YFP with each half coupled to a POI (Fig. 6). Either the N-terminal (aa 1-155) or C-terminal part (aa 156-720) of the YFP is fused to the C-terminal region of the POI via a linker sequence to ensure proper quaternary structure of the protein. If two proteins interact, the YFP fluorescence is restored, which can be measured using flow cytometry.
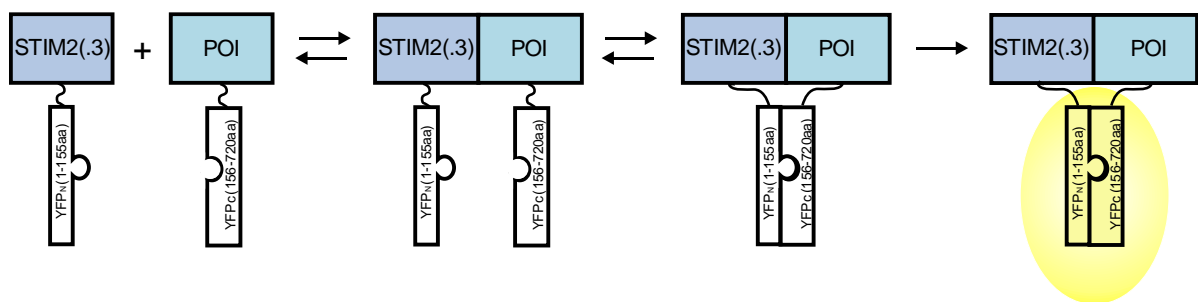
Figure 6 Principle of bimolecular fluorescent complementation (BiFC).

Flow cytometry

Flow cytometry is a sensitive method to measure single cells in suspension based on different optical parameters. Flow cytometry can be used to determine the expression of intracellular and surface molecules allowing a multi-parameter analysis of individual cells and cell populations. The cell suspension flows rapidly through a flow cell in a narrow stream of liquid. A vibrating mechanism breaks the stream into individual droplets, which are measured by different laser beams resulting in characteristic

scattered light and fluorescent signals. The forward scatter (FSC) measures diffracted light providing information about the cell size. The sideward scatter (SSC) measures refraction providing information about the granularity of a cell. Further fluorescence signals can be measured using different laser beams and their respective filter sets. Flow cytometry is a high-throughput method for acquiring representative information of a cell population within a short period of time.

To analyze protein-protein interactions, HEK STIM1/2$^{-/-}$ cells were transfected with HA-STIM2.2-YFPc or HA-STIM2.3-YFPc as the hunter construct and POI-YFPn as the bait construct as described in 3.1.2. Due to the size differences of the vector backbones, hunter and bait constructs were transfected in an equimolar ratio. 24 hours post transfection, cells were activated using 1 µM Tg for 10 min at RT. Cells were detached using PBS, centrifuged at 320 g for 10 min and resuspended in 400 µl ice cold FACS buffer containing Zombie Aqua™ Fixable Viability Kit (according to manufacturer's protocol). After 15 min incubation, cells were measured using the FACSVerse and BD FACSuite software.

The analyzed gates were as followed and dependent on the previously set gate:

1. Total cell population (excluding cell debris)
2. Single cells (excluding doublets)
3. Viable cells (using Zombie Aqua Fixable Viability Kit)
4. YFP positive cells.

Protein-protein interaction was characterized by the percentage of YFP positive cells. A non-interacting bait (EFEMP-YFPn) served as the negative control, while the interaction of each hunt with itself (e.g. STIM2.2-YFPc+STIM2.2-YFPn) served as the positive control. The obtained data was analyzed using the FlowJo Software 10.0.7.

3.7 Microscopy

3.7.1 Calcium Imaging

Method

Fura2-based Ca^{2+} imaging is a microscopic method to measure changes in global cytosolic Ca^{2+} concentration over time. The fluorescent dye Fura2-AM is coupled to an acetoxymethyl ester (AM) group allowing it to diffuse into the cell. Endogenous esterases catalyze the cleavage of the AM group abolishing excretion of the indicator. The ratiometric dye Fura2 chelates free cytosolic Ca^{2+} via its four negatively charged

carboxymethyl groups, changing the excitation maximum from 380 nm (Ca^{2+} unbound) to 340 nm (Ca^{2+} bound). Emission is constantly measured at 510 nm. Hence, the emission ratio, measured at 510 nm, after excitation with 340 nm and 380 nm (ratio 340/380) is proportional to the cytosolic Ca^{2+} concentration independently of the loading efficacy of the indicator. As reported in Grynkiewicz et al. (1985), the ratio 340/380 can be converted into Ca^{2+} concentrations using the following equation:

$$Calcium\ (nM) = K_d(Fura2)\ x\ \frac{(R-Rmin)}{(Rmax-R)}\ x\ \frac{Fmax}{Fmin}$$

K_d is the dissociation constant of Fura2, R is the background corrected ratio value at any time during the measurement. $Rmin$ is the minimum ratio measured during calibration after store depletion with Tg and ionomycin in the absence of extracellular Ca^{2+}. $Rmax$ is the measured maximum ratio in the plateau state after addition of 20 mM Ca^{2+}. $Fmax$ is the maximum measured value at 380 nm in the absence of Ca^{2+} and $Fmin$ the minimum measured value at 380 nm in the presence of 20 mM Ca^{2+}.

Protocols

For Ca^{2+} imaging experiments HEK STIM1/2$^{-/-}$, SH-SY5Y STIM2$^{-/-}$ or SH-SY5Y STIM1/2$^{-/-}$ cells were transfected as described in 3.1.2. Cells were loaded with 1 μM Fura2-AM at RT for 30 min. The coverslips were placed in a perfusion chamber connected to a perfusion system. Fura2 was excited alternately at 340 nm and 380 nm every 5 s and emission was measured at 510 nm. The set up consists of an Observer.A1 microscope, a transmitted light source, a polychrome V, an Imago CCD Camera Andor clara and an Imaging Control Unit. Acquisition was controlled by and background-subtracted 340nm/380nm ratio values were calculated using VisiView Software. 340nm and 380nm images were acquired with 10-30ms exposure times and 1x1 or 2x2 pixel binning through a 20x0.75 Fluar (Zeiss) objective. Transfected cells were identified before each measurement. Store-operated (SOCE; ORAI) as well as voltage-gated (VGCE; Ca$_V$) Ca^{2+} entry was analyzed using different perfusion protocols. To investigate SOCE, the Ca^{2+} readdition protocol was used. Cells were washed with 0.5 – 1.5 mM Ca^{2+} ringer solution to analyze basal Ca^{2+} levels. After the internal Ca^{2+} stores were depleted using 1 μM Tg in 0 mM Ca^{2+} ringer, Ca^{2+} influx through store-operated channels was induced by perfusion with an external 0.5 – 1.5 mM Ca^{2+} solution. To identify dying cells, the Ca^{2+} solution was again changed to 0 mM Ca^{2+} at the end of each measurement (Fig. 7 upper panel). Ratio data was further analyzed using IgorPro (Wavemetrics).

Store operated Ca^{2+} entry Ca^{2+} readdition protocol					
0.5-1.5	0	0+Tg	0.5-1.5	0	Ca^{2+}[mM]
resting Ca^{2+}		store depletion (inhibition of SERCA)	Ca^{2+} influx = SOCE		

Store operated Ca^{2+} entry global protocol		
0.5-1.5	0.5-1.5 +Tg	0	Ca^{2+}[mM]
resting Ca^{2+}	store depletion (inhibition of SERCA) + Ca^{2+} influx (SOCE)	

Figure 7 Perfusion protocols. Ca^{2+} readdition (upper panel) and global (lower panel) protocol with indicated Ca^{2+} solutions for each perfusion step.

For kinetic parameters, average (5-10 frames) basal and plateau ratio values and maximal Tg- or Ca^{2+} readdition-induced peak ratio values were determined. To obtain Δs, the average ratio before addition of Tg or Ca^{2+} was subtracted, respectively. The influx rate is represented by the slope of a linear fit performed on the ratio values of 1 frame before and 4 frames after Ca^{2+} readdition. The data was then imported into GraphPad 9 (Prism) for further statistical analysis and plotting. To analyze VGCE, voltage-gated Ca^{2+} channels were activated after baseline recording by perfusion of a high potassium (K$^+$) solution leading to depolarization of the membrane and subsequent channel activation. In the combined protocol, the perfusion of the high K$^+$ solution was added before store depletion and Ca^{2+} readdition protocol was performed as previously described (Fig. 8).

Voltage gated + Store operated Ca^{2+} entry combined Ca^{2+} readdition protocol					
0.5-1.5	0.5-1.5 + K$^+$	0	0+Tg	0.5-1.5 +Tg	0	Ca^{2+}[mM]
resting Ca^{2+}	K$^+$ induced depolarization = VGCE		store depletion (inhibition of SERCA)	Ca^{2+} influx = SOCE	

Figure 8 Combined voltage-gated and Ca^{2+} readdition protocol with indicated Ca^{2+} solutions used for each perfusion step.

In the global protocol, store depletion and Ca^{2+} influx occurred simultaneously by perfusion of 1 μM Tg in Ca^{2+} containing ringer solution after baseline recording (Fig. 7 lower panel). Increase in cytosolic Ca^{2+} concentration was quantified by area under the curve (AUC) using Graph Pad Prism 9.

3.7.2 Localization analysis

Localization analysis was performed using the Cell Observer (Zeiss), a widefield epifluorescence microscope suitable to record cells over a long period of time and to acquire defined z-stacks. The temperature and CO_2 module allow the observation of cells under incubator-like conditions. To analyze co-localization of STIM proteins, HEK STIM1/2$^{-/-}$ cells were transfected as described in 3.1.2 with the in Tab. 35 listed plasmids in a 1:1 ratio.

z-stacks before (-Tg) and after store depletion (+Tg) induced by 1 µM Tg in 0.5 mM Ca^{2+} ringer solution were acquired using the 100x oil objective. YFP and mCherry were excited using LED 470 (470/40) and filter cube 54HE and LED N-White + Ex (556/20) and filter cube 56HE, respectively. Each stack was defined by a total width of 6.5 µm consisting of 25 levels with spacing of 0.26 µm. The excitation of each fluorophore was calculated by the software corresponding to 30 % of the maximum camera saturation.

Table 35 **Plasmid combinations used for transfection**

plasmid 1	plasmid 2
YFP-STIM2.2	STIM2.2-mCherry
YFP-STIM2.3	STIM2.2-mCherry
YFP-STIM2.3	STIM1-mCherry
YFP-STIM2.2Δ5K	STIM2.2-mCherry
YFP-STIM2.2Δ674	STIM2.2-mCherry

Image editing

Editing of the acquired z-stacks was performed using the software Huygen's Essentials. Images were deconvoluted to minimize scattered light followed by background subtraction using the rolling ball algorithm (Fjii) and processed as maximum intensity projections (MIP) for visualization. All editing steps were performed equally on each channel. Co-localization analysis was quantified by the Mander's overlapping co-efficient using the JACoP plugin (Fiji) on single stacks. Threshold was set as mean fluorescence plus two times standard deviation (SD). M1 quantifies the co-localization of the red channel with the green one, M2 quantifies the co-localization of the green channel with the red one. Further data analysis and plotting was performed in GraphPad Prism 9.

3.7.3 Total internal reflection fluorescence microscopy

The principle of total internal reflection fluorescence microscopy (TIRFM) is based on totally internally reflected excitation light at the solid-liquid interface between the coverslip and the specimen. At the interface, an evanescent wave is generated, which exponentially decays with distance and excites fluorescent molecules only within a few hundred nanometers (< 200 nm) of the solid surface efficiently. Thus, TIRFM is suitable to particularly analyze molecules near the plasma membrane. The penetration depth of the evanescent wave is dependent on the incident illumination angle, wavelength, and the refractive index. In comparison to other light microscopes, the advantages of TIRFM are higher signal-to-background ratios, less out-of-focus fluorescence, and lower exposure times.

To analyze cluster formation, HEK STIM1/2$^{-/-}$ cells were transfected with YFP-STIM2.X and PH-PLCγ-mCherry in a 3:1 ratio as described in 3.1.2. Images were acquired using a 100x/1.47 HCX PlanApo oil objective and the Leica AM TIRF MC System. YFP and mCherry were excited using 488 nm or 561 nm lasers with BP525/50 and BP600/40 (DRT) emission filters, respectively. For co-localization analysis, images were acquired after store depletion using 1 µM Tg in 0.5 mM Ca^{2+} ringer solution for 10 min at RT. The exposure time was set to 100 ms and the penetration depth was set to 150 nm. After 1 min baseline recording and subsequent store depletion using 1 µM Tg in 0.5 mM Ca^{2+} ringer solution, cluster formation was monitored for 20 min acquiring an image every 20 sec. The TIRF focal plane was set according to the PH-PLCγ-mCherry signal and penetration depth was set to 90 nm.

Image editing

Image editing was performed using the software Fiji. After background subtraction using the *rolling ball* algorithm, co-localization analysis was quantified by the Mander's overlapping co-efficient using the JACoP plugin. Threshold was set as mean fluorescence plus two times SD. M1 quantifies the co-localization of the red channel with the green one, M2 quantifies the co-localization of the green channel with the red one. All editing steps were performed equally on each channel. After background subtraction using the *rolling ball* algorithm, analysis of cluster formation was performed using *Analyze particles* (size = 0; circularity = 0), *Gaussian blur*, thresholding with *Moments* and *Watershed*. All editing steps were performed equally on each time point. Further data analysis and plotting was performed in GraphPad Prism 9.

3.7.4 NFAT translocation assay

SH-SY5Y STIM1/2$^{-/-}$ cells were transfected with 1 μg mKate2-STIM2.X or empty vector and 1 μg NFAT1-GFP as described in 3.1.2. NFAT translocation into the nucleus was detected on the Axio Observer 7 (Zeiss) equipped with a Prime95B sCMOS camera using with a 63x/1.40 Plan Apochromat oil objective. GFP and mKate2 signals were excited using a HXP 120 V compact light source with 480-498nm/560-584nm excitation filters and Fura8 (BS488nM, BP500-550nm)/63 HE Red (BP559-585nm, BS590nm, BP600-690nm) emission filter cubes. Cells were imaged in a Z-plane near the nucleus stained with 1 mg/ml Hoechst 33342 dye for 3 min at RT immediately before the measurement. Images were acquired before (-Tg) and after stimulation with 1 μM Tg in 1 mM Ca^{2+} ringer solution (+Tg) for 30 min. The ratio of GFP signal in the cytoplasm vs. nucleus was quantified using the *polygonal selection tool* (Fiji).

3.8 Statistical analysis

Statistical analysis was performed using the software GraphPad Prism 9. The statistical test was chosen according to the normal distribution and number of conditions. Significances are as follows: * p<0.05, ** p<0.01, *** p<0.001. Data is displayed as mean $\pm$ SEM obtained from 3 independent transfections.

4 Results

4.1 Expression of the shorter splice variant STIM2.3

Both conventional *STIM1* and *STIM2* genes are encoded by 12 exons. Despite their similar exon numbers and structure, *STIM1* and *STIM2* translate into mature proteins with a diverging cytosolic region. The number of exons increases the probability of alternative splicing leading to several predicted splice variants for STIM1 and at least three predicted variants for human STIM2, namely STIM2.1, STIM2.2 and STIM2.3 (Fig. 9A). Compared to the conventional STIM2.2, an additional short exon 9 within the CAD converts STIM2.1 to a potent inhibitor of SOCE, which is no longer able to activate ORAI [Miederer et al. 2015; Rana et al. 2015]. Insertion of an alternative 36 bp long exon 13 (STIM2.3) between the exons 12 and 14 leads to a premature stop resulting in a
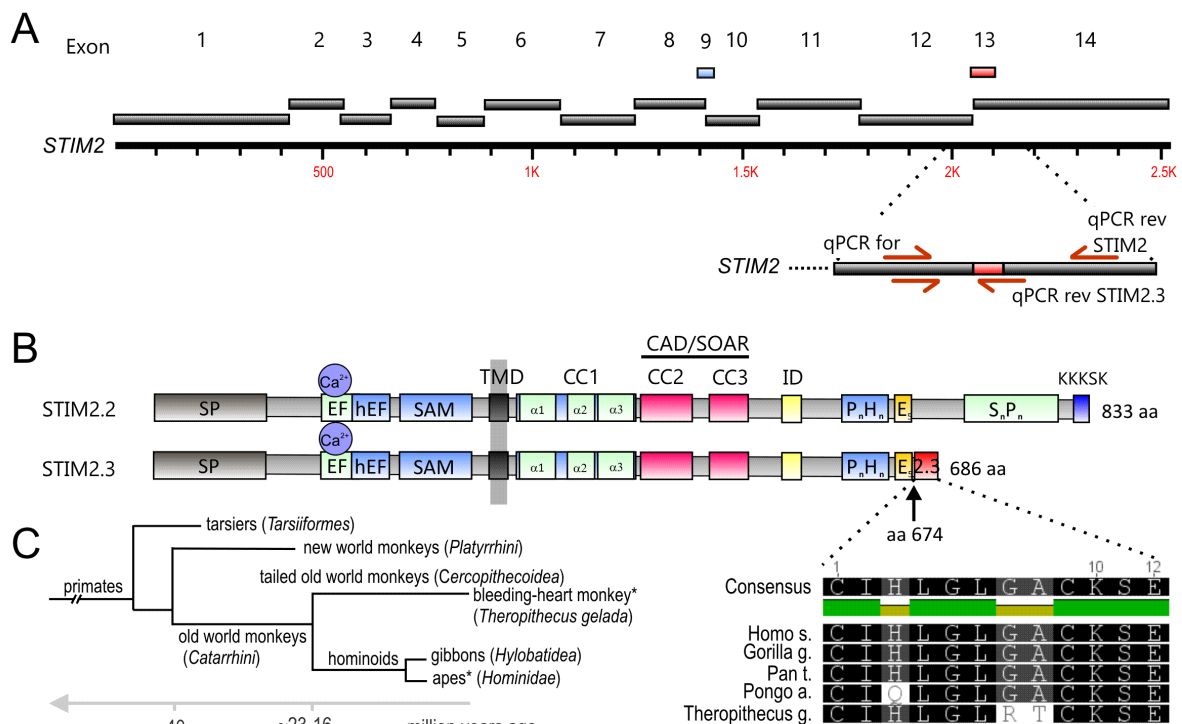
Figure 9 Evolution and structure of the splice variant STIM2.3. A: Schematic exon structure of STIM2 gene with conventional exons depicted in grey. Alternative exon 9 (STIM2.1) is highlighted in blue, alternative exon 13 (STIM2.3) is highlighted red. Schematic representation of primer annealing sites on coding mRNA. **B**: Schematic protein structure of STIM2 showing functional domains. STIM2.3-specific domain (red) is inserted after poly E domain at aa 674 and evolutionary amino acid conservation is depicted below with identical aa within black boxes. **C**: Phylogenetic tree of the emergence of exon STIM2.3, expression is indicated with an asterix.

translated protein lacking the C-terminal microtubule-associated EB binding sites, serine/proline rich region and the polybasic domain. The last common residue between STIM2.2 and STIM2.3 is at position 674 (Fig. 9B). Previous expression analysis revealed *STIM2.3* expression in human brain while it was not detected in mice or immune cells [Miederer et al. 2015; Gilson 2016]. Searching for the STIM2.3 specific amino acid sequence (CIHLGLGACKSE) using BLAST revealed existence of STIM2.3 in old world monkeys (*Catarrhini*) such as gorilla and chimpanzee, but not in new world monkeys or other mammals such as mice (Fig. 9C). Concluding, the short STIM2.3 specific exon evolved ~15-20 million years ago with the emergence of hominoids, suggesting a need for alternative STIM isoforms with the increased tissue complexity. Hence, expression levels of *STIM* and *ORAI* were quantified using cDNA derived from several postmortem human brain regions of six different donors. The brain regions cerebellum, thalamus, hippocampus as well as frontal and occipital lobe, which both belong to the cortex, were examined. In human cerebellum, *STIM1* and *ORAI2* are the predominantly expressed homologues (Fig. 10A). Expression of total *STIM2* was quantified using *STIM2* calibrated primers, detecting both *STIM2.2* and *STIM2.3*, revealing similar expression in the analyzed brain regions. Using splice specific primers, *STIM2.3* expression was confirmed in all analyzed regions with the highest abundance in cerebellum and frontal lobe followed by occipital lobe, hippocampus, and thalamus (Fig. 10B). Overall, a slightly higher expression was observed in female donors (Fig. 10, red points). However, expression variability might be due to different postmortem and sample preparation times.
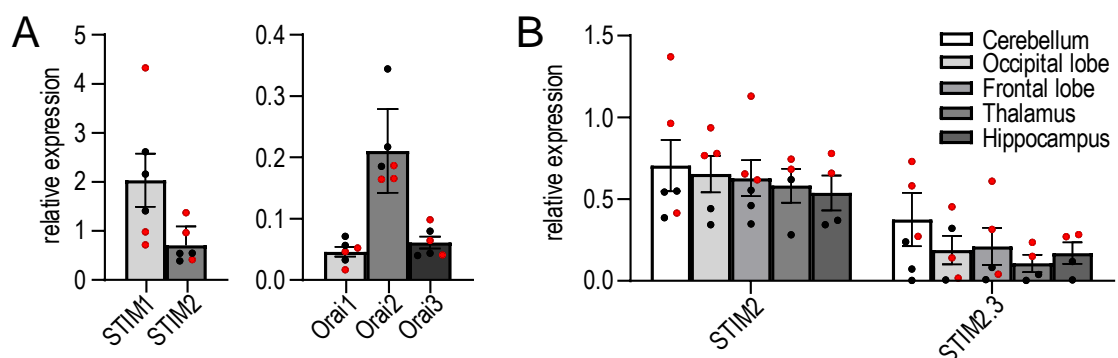
Figure 10 Expression of STIM2.3 in human brain. A: Relative expression of STIM1 and STIM2 (left panel) and Orai1-3 (right panel) in human postmortem cerebellum derived from six different donors. **B**: Relative expression of total STIM2 and STIM2.3 in different postmortem human brain regions as indicated. Male donors are displayed in black, female donors are displayed in red.

4.2 Generation of clonal SH-SY5Y STIM knockout cell lines

The neuroblastoma cell line SH-SY5Y, originally derived from the parental SK-N-SH cell line, is a suitable system to investigate more neuron-like functions without using primary neurons. The time in culture of isolated neurons and fully differentiated stem cells is limited since they stop dividing once fully maturated. The SH-SY5Y cell line is commonly used in neuroscience as an in vitro model to study neuronal diseases such as Alzheimer's and Parkinson's disease [reviewed in Kovalevich and Langford 2013]. SH-SY5Y is an adherent cell line which can be easily propagated, thus, offering certain advantages over primary cells.

To investigate potential physiological functions of the two STIM2 variants in a more neuronal background, the SH-SY5Y cell lines lacking endogenous STIM1 and/or STIM2 were used. After knockout of both STIM homologues performed by the group of Markus Grimm using the CRISPR/Cas9 system, clonal cell lines derived from a single cell were generated. The knockout of the different SH-SY5Y STIM1$^{-/-}$ and/or STIM2$^{-/-}$ clones was confirmed on genomic DNA level using sequencing and on protein level using Western Blot. Sequencing of the gRNA targeted region in STIM1 confirmed a deletion of one base (c.25delC) within exon 1 resulting in a premature stop after 74 amino acids in SH-SY5Y STIM1$^{-/-}$ clone #3 and #8 and STIM1/2$^{-/-}$ clone #11 (Fig. 11A upper panel). Sequencing of the targeted region in STIM2 revealed a nucleotide insertion (c.393insA) within exon 1 leading to a premature stop after 131 amino acids in SH-SY5Y STIM2$^{-/-}$ clone #4 and
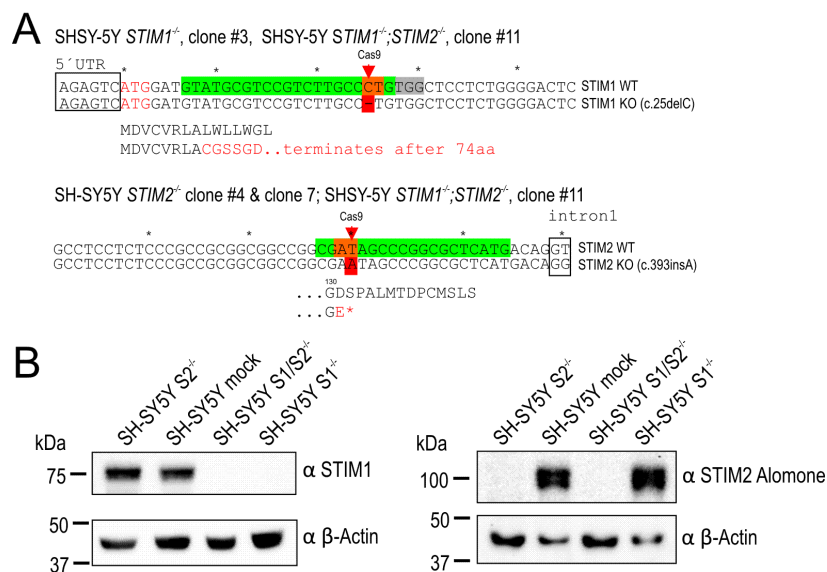
Figure 11 Generation of clonal SH-SY5Y STIM$^{-/-}$ cell lines. A: Genomic DNA sequences of WT and clonal SH-SY5Y STIM$^{-/-}$ cell lines with targeted gRNA sequences indicated in green and CRISPR event indicated in red. Translation of the sequences is indicated below. **B**: Western blot demonstrating absence of STIM1 in SH-SY5Y STIM1$^{-/-}$ and STIM1/2$^{-/-}$ (left) and absence of STIM2 in SH-SY5Y STIM2$^{-/-}$ and STIM1/2$^{-/-}$ cells (right). (Modified from Ramesh et al. 2021)

clone #7 as well as STIM1/2$^{-/-}$ clone #11 (Fig. 11A lower panel). The corresponding STIM1 and STIM2 bands on Western Blot were absent in the single and double-knockout cells compared to the mock transfected cell line, respectively (Fig. 11B).

4.3 Functional characterization of STIM2 variants

4.3.1 STIM2.3 is a gain-of-function variant

To investigate the effect of the naturally occurring C-terminal truncation on STIM2 mediated SOCE, Fura2-based Ca^{2+} imaging experiments were performed using HEK STIM1/2$^{-/-}$ cells transfected with YFP-STIM2.2, YFP-STIM2.3 or control vector. HEK STIM1/2$^{-/-}$ cells showed no SOCE with mock transfection, which was rescued by re-expression of STIM2.2 (Fig. 12A). Surprisingly, expression of STIM2.3 rescued SOCE and displayed significantly increased influx rate, Δpeak and Δplateau compared to STIM2.2 (Fig. 12A,B). Moreover, STIM2.3 increased basal Ca^{2+} concentration compared to control transfected cells, but with no significant difference compared to STIM2.2, which is known to increase basal Ca^{2+} levels due to its sensitive EF hand (Fig. 12B). To exclude expression artefacts, YFP fluorescence intensity was quantified for both YFP-STIM2.2 and YFP-STIM2.3, showing no significant differences (Fig. 12C).
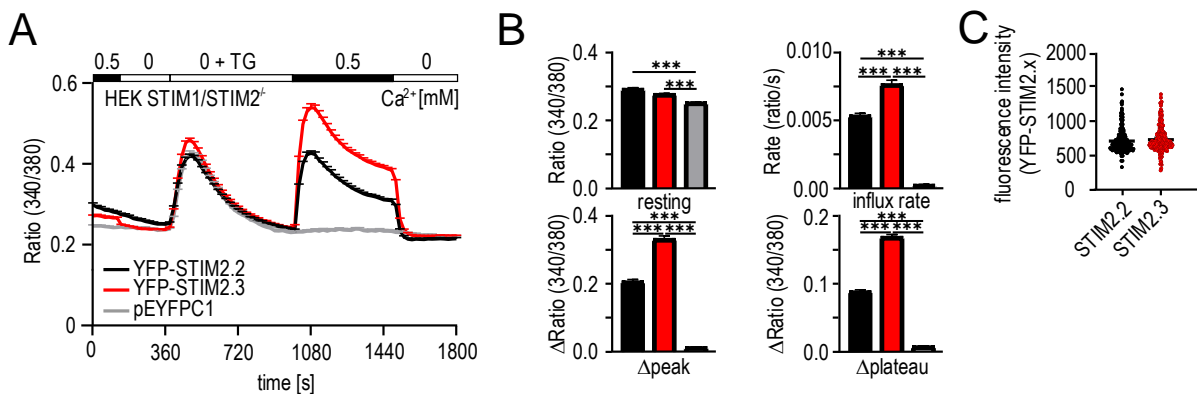
Figure 12 STIM2.3 is a gain-of-function variant. A: Average traces showing changes (mean+SEM) in intracellular Ca^{2+} (Ratio 340/380) over time in response to perfusion of different external Ca^{2+} [mM] as indicated in the upper bar in HEK STIM1/2$^{-/-}$ cells transfected with YFP-STIM2.2 (black, n=227), YFP-STIM2.3 (red, n=232) or empty vector (grey, n=27). **B**: Quantification of changes in resting Ca^{2+}, influx rate, Δpeak and Δplateau measured in A. *** p< 0.001; Kruskal-Wallis ANOVA. **C**: Quantification of YFP fluorescence intensity from cells measured in A.

STIM2.3 was also expressed in SH-SY5Y cells only lacking STIM2 (SH-SY5Y STIM2^{-/-}) or co-overexpressed with STIM2.2 at a 1:1 ratio in HEK STIM1/2[-/-] cells demonstrating a gain-of-function phenotype on both STIM1 and STIM2 function. In SH-SY5Y STIM2^{-/-}, expression of STIM2.3 increased resting Ca^{2+} levels and STIM1-mediated SOCE with significantly increased influx rate, Δpeak and Δplateau (Fig. 12A,B).
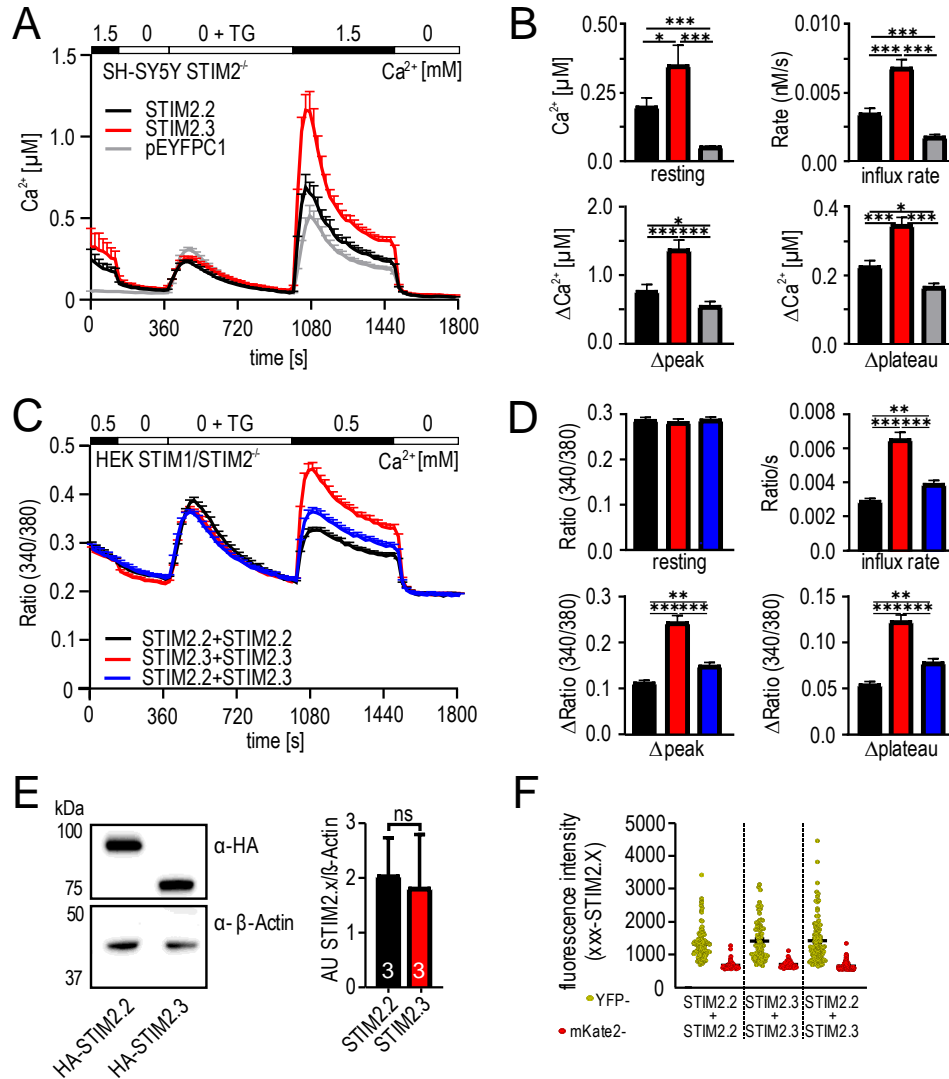
Figure 13 STIM2.3 increases STIM1 and STIM2 mediated SOCE. A: Calibrated traces showing changes (mean+SEM) in intracellular Ca^{2+} (μM) over time in response to perfusion of different external Ca^{2+} [mM] as indicated in the upper bar after transfection with HA-STIM2.2 (black, n=85), HA-STIM2.3 (red, n=89) or empty vector (grey, n=94) in SH-SY5Y STIM2^{-/-} cells. **B**: Quantification of changes in resting Ca^{2+}, influx rate, Δpeak and Δplateau measured in A. *** $p < 0.001$, * $p < 0.05$; Kruskal-Wallis ANOVA. **C**: Average traces showing changes (mean+SEM) in intracellular Ca^{2+} (Ratio 340/380) over time in response to perfusion of different external Ca^{2+} [mM] as indicated in the upper bar in HEK STIM1/2[-/-] cells transfected with YFP-STIM2.2+mKate-STIM2.2 (black, n=100), YFP-STIM2.3+mKate-STIM2.3 (red, n=77) and YFP-STIM2.2+mKate-STIM2.3 (blue, n=99). **D**: Quantification of changes in resting Ca^{2+}, influx rate, Δpeak and Δplateau measured in C. *** $p < 0.001$, ** $p < 0.01$; Kruskal-Wallis ANOVA. **E**: Western Blot showing HA-STIM2.2 and HA-STIM2.3 following heterologous expression in HEK STIM1/2[-/-] cells (left), quantification from 3 independent transfections (right). **F**: Quantification of YFP and mKate fluorescence intensity from cells measured in C.

Co-overexpression of STIM2.2 or STIM2.3 with STIM1 in a 1:1 ratio in HEK STIM1/2$^{-/-}$ cells showed similar results [Poth 2018]. Interestingly, expression of STIM2.2 in SH-SY5Y STIM2$^{-/-}$ significantly increased SOCE, but with only little effect on Δpeak and Δplateau compared to cells only expressing endogenous STIM1 (empty vector) (Fig. 12A,B). No significant differences in resting Ca^{2+} levels were observed in HEK STIM1/2$^{-/-}$ cells expressing STIM2.2, STIM2.3 or both variants in a 1:1 ratio (Fig. 12D). However, co-overexpression of STIM2.3 and STIM2.2 displayed an intermediate SOCE phenotype significantly increasing influx rate, Δpeak and Δplateau compared to only STIM2.2 expressing cells but not to the extent of cells solely expressing STIM2.3 (Fig. 12C,D). Insertion of the short STIM2.3 specific exon leads to a 17 kDa shift in molecular weight and does not alter protein levels as quantified in Fig. 12E or after quantification of YFP and mKate2 fluorescence intensities after heterologous expression in HEK STIM1/STIM2$^{-/-}$ cells (Fig. 12F). Albeit different fluorescence intensities of YFP and mKate2, no differences were observed in the intensity between the two STIM2 variants labeled with the same fluorescent protein.

4.3.2 STIM2.3 colocalizes with STIM1 and STIM2.2

In STIM2, the PBD domain functions as an ER retention signal. To investigate whether the C-terminal deletion including the PBD affects localization of STIM2.3, HEK cells lacking endogenous STIM were transfected with YFP-STIM2.3 and mCherry-STIM1 or STIM2.2-mCherry in a 1:1 ratio. Co-localization before and after store depletion was analyzed using the Mander's overlapping coefficients. Under resting conditions, STIM2.3 co-localizes with STIM1 (Fig. 14A left panel). Strikingly, STIM2.3 co-localizes with STIM2.2 at the focal plane near the nucleus but does not display the characteristic pre-clustering at the focal plane near the plasma membrane despite the identical sensitive EF hand as in the conventional STIM2 (Fig. 14A right panel). After store depletion, STIM2.3 clusters in the same ER-PM junctional regions as STIM1 and STIM2.2 (Fig. 14B). Analysis of Mander's overlapping coefficients were as follows before (-Tg) store depletion S1+S2.3 M1 = 0.91, M2 = 0.95; S2.2+S2.3 at the nucleus M1 = 0.9, M2 = 0.89; S2.2+S2.3 at the PM M1 = 0.97, M2 = 0.58 revealing no difference in the localization of STIM2.3 compared to STIM1 and STIM2.2 at the nucleus but demonstrating that STIM2.3 does not precluster in contrast to STIM2.2 (Fig. 14C).

After store depletion, Mander's coefficients were as follows for S1+S2.3 M1 = 0.78, M2 = 0.81 and for S2.2+S2.3 M1 = 0.74, M2 = 0.75 (Fig. 14D). Comparison of the cluster sizes of STIM2.3 with STIM1 or STIM2.2 after Tg induced store depletion revealed no significant differences as quantified in (Fig. 14E).
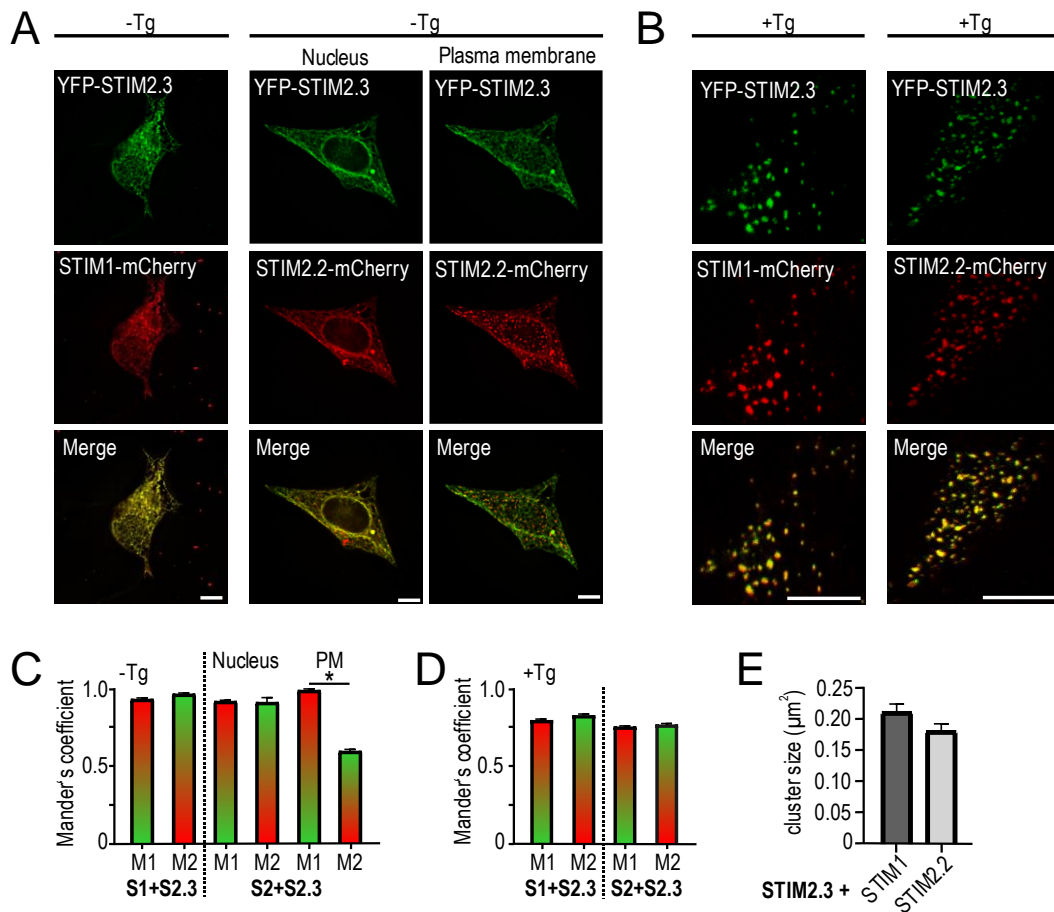

Figure 14 STIM2.3 co-localizes with STIM1 and STIM2.2. A-B: Representative images of HEK STIM1/2$^{-/-}$ cells co-transfected with YFP-STIM2.3 (green) and STIM1-mCherry (red) (left) or STIM2.2-mCherry (red) (right) and merged images before (A) and after (B) stimulation with 1 μM Thapsigargin. Scale bar indicates 10μm. **C-D**: Co-localization analysis of cells from (A,B). For each condition 5-45 cells from 3 independent transfections were analyzed using Mander's overlapping coefficients (M1, M2) (mean + SEM): S1+S2.3 –Tg M1:0.91 M2: 0.95; S2.2+S2.3 –Tg nucleus M1: 0.90 M2: 0.89; S2.2+S2.3 –Tg plasma membrane M1: 0.97 M2: 0.58; S1+S2.3 +Tg M1: 0.78 M2: 0.81; S2.2 +S2.3 +Tg M1: 0.74 M2: 0.75. **E**: Quantification of cluster size (μm^2) after store depletion of cells measured in B.

4.3.3 Increased interaction of STIM2.3 with ORAI2

Expression of the SOCE components varies upon different cell types adapting Ca^{2+} signaling to individual cellular needs. The human cell lines HEK and SH-SY5Y are of distinct origins, thus, differentially express *STIM* and *ORAI*. To investigate whether enhanced interaction of STIM2.3 with ORAI is responsible for the gain-of-function SOCE phenotype, expression levels of the three *ORAI* homologues (*ORAI1-3*) were quantified

in SH-SY5Y STIM2$^{-/-}$, SH-SY5Y STIM1/2$^{-/-}$ and HEK STIM1/2$^{-/-}$ using RNA sequencing (Fig. 15A). In both SH-SY5Y STIM$^{-/-}$ cell lines, *ORAI2* is the predominantly expressed isoform with the highest FPKM values. In contrast, in HEK STIM1/2$^{-/-}$, *ORAI1* is the most abundant *ORAI* homologue with a higher FPKM value than *ORAI2* and *ORAI3*. Furthermore, interaction of both STIM2 variants with STIM and ORAI was quantified using bimolecular fluorescence complementation assay as the alternative for FRET analysis (Fig. 15B). Both methods are based on fluorescence detection if two proteins of interest interact within a maximum distance of 10 nm. For BiFC, HEK STIM1/2$^{-/-}$ cells were transfected with HA-STIM2.2-YFPc or HA-STIM2.3-YFPc as the hunter construct and STIM-YFPn or ORAI-YFPn as the bait constructs. After Tg-induced store depletion, reconstitution of the YFP fluorescence following an interaction of hunter and bait was measured using flow cytometry. EFEMP1 showed no interaction with either STIM2 variant and therefore served as the negative control. Interaction of the hunter construct with its own bait (e.g. STIM2.2-YFPc+STIM2.2-YFPn) served as the positive control, which was at 30 % YFP-positive cells for STIM2.2 and 50 % YFP-positive cells for STIM2.3. Interaction of STIM2.2 and STIM2.3 as the hunter and the other STIM2 variant (i.e. STIM2.2-YFPn or STIM2.3-YFPn) as the bait was similar to the corresponding positive control with 27 % and 41 % YFP positive cells, respectively. STIM2.3 showed an increased interaction with STIM1 (51 %) compared to STIM2.2 (34 %), which was similar to the positive control for STIM2.3. No significant differences were observed for STIM2.2 or STIM2.3 and ORAI1 (21 %, 23 %) or ORAI3 (4 %; 9 %), respectively. Strikingly, interaction of STIM2.3 with ORAI2 (17 %) was significantly increased compared to STIM2.2 (10 %) (Fig. 15B).
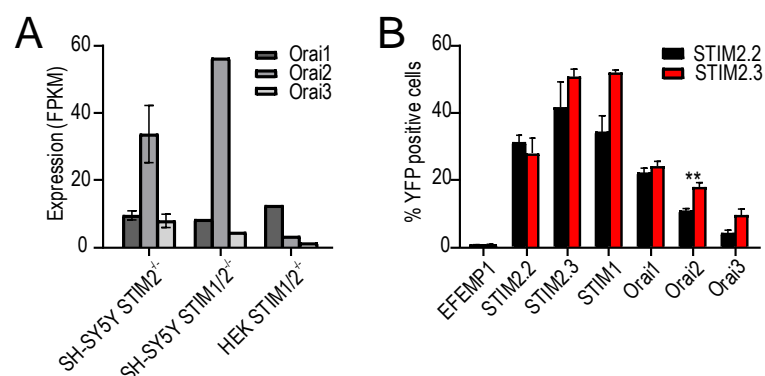
Figure 15 Increased interaction of STIM2.3 with Orai2. A: FPKM values of Orai 1-3 genes in SH-SY5Y STIM2$^{-/-}$, SH-SY5Y STIM1/2$^{-/-}$ and HEK STIM1/2$^{-/-}$ cells from RNA Seq analysis. **B**: Interaction of STIM2.2-YFPc (black) or STIM2.3-YFPc (red) with POI-YFPn in HEK STIM1/2$^{-/-}$ cells was quantified as % YFP positive cells with bimolecular fluorescence complementation via flow cytometry. Data (mean+SEM) was obtained from 3 independent transfections with 10,000 measured cells each.

### 4.3.4 STIM2.3 mediated phenotype is residue independent

To investigate whether the STIM2.3 specific residues or the C-terminal deletion are responsible for the observed gain-of-function phenotype, a mutant terminating at the last common amino acid (STIM2.2Δ674) and a mutant only lacking the last 5 amino acids, i.e. the PBD (STIM2.2Δ5K), were generated (Fig. 16A). For better visualization, quantification of the analyzed parameters is displayed as fold change normalized to STIM2.2. Ca^{2+} imaging experiments of HEK STIM1/2$^{-/-}$ cells expressing YFP-STIM2.2, YFP-STIM2.3, YFP-STIM2.2Δ5K or YFP-STIM2.2Δ674 revealed that the larger C-terminal deletion in STIM2.2Δ674 indeed is sufficient to reproduce the STIM2.3-mediated SOCE phenotype while deletion of the PBD significantly reduced STIM2-mediated SOCE (Fig. 16B). Expression of STIM2.2Δ674 led to significantly increased Δpeak and Δplateau but did not increase influx rate compared to STIM2.2. In contrast, STIM2.2Δ5K significantly reduced resting Ca^{2+}, influx rate, Δpeak and Δplateau compared to STIM2.2 (Fig. 16C). These results indicate, that, indeed, the larger C-terminal deletion and not the splice-specific residues encode the gain-of-function SOCE phenotype of STIM2.3. Moreover, full-length STIM2 requires the PBD for proper unfolding and subsequent ORAI activation. Co-localization analysis of STIM2.2-mCherry with YFP-STIM2.2Δ674 or STIM2.2Δ5K at the focal plane near the plasma membrane under resting conditions were performed to examine whether deletion of the PBD abolishes the characteristic pre-clustering as seen with STIM2.3. As shown in Fig. 16D, neither STIM2.2Δ674 nor STIM2.2Δ5K display pre-clustering despite their differential regulation of resting Ca^{2+} levels (Fig. 16C). Analysis of Mander's overlapping coefficients were as follows for STIM2.2Δ674+STIM2.2 M1 = 0.48 , M2 = 0.37 and for STIM2.2Δ5K+STIM2.2 M1 = 0.58, M2 = 0.45 demonstrating inadequate co-localization of STIM2.2Δ674 and STIM2.2Δ5K with STIM2.2 compared to co-localization of STIM2.2 with itself (Fig. 16E).

Indeed, these results indicate that characteristic pre-clustering is mediated by the PBD, anchoring STIM2 at phospholipids at the inner leaflet of the plasma membrane under resting conditions.
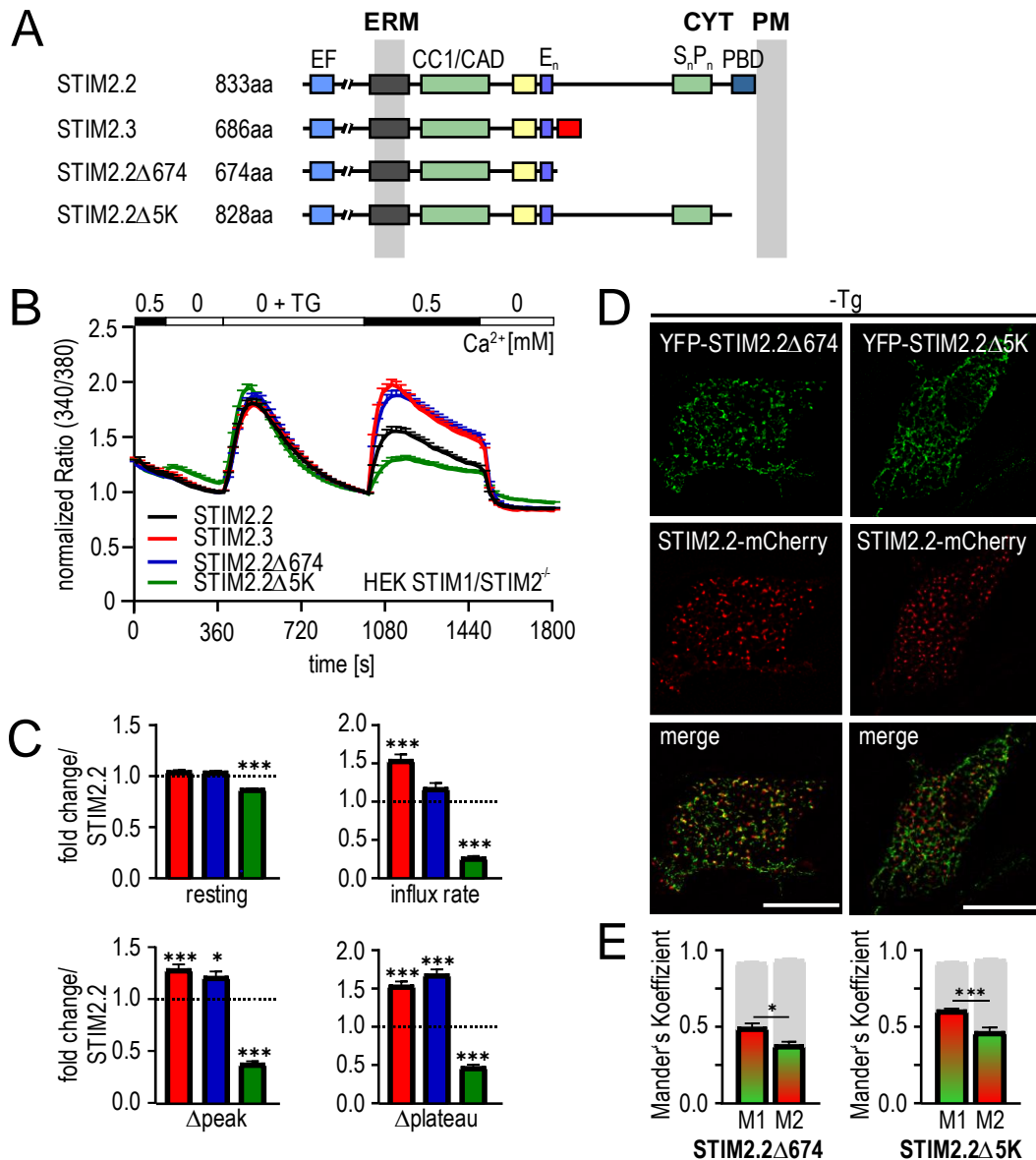
Figure 16 STIM2.3 mediated SOCE phenotype is independent of the splice specific residues. A: Schematic protein structure with functional domains of STIM2.2, STIM2.3 and the STIM2 mutants terminating after aa674 (STIM2.2Δ674) or lacking the PBD (STIM2.2Δ5K). **B:** Normalized average traces showing changes (mean+SEM) in intracellular Ca^{2+} (Ratio 340/380) over time in response to perfusion of different external Ca^{2+} [mM] as indicated in the upper bar after transfection of YFP-STIM2.2 (black, n=144), YFP-STIM2.3 (red, n=145), YFP-STIM2.2Δ674 (blue, n=132) or YFP-STIM2.2Δ5K (green, n=164) in HEK STIM1/2$^{-/-}$ cells. **C:** Quantification of changes in resting Ca^{2+}, influx rate, Δpeak and Δplateau measured in B as fold change normalized to STIM2.2. *** p< 0.001, * p< 0.05; Kruskal-Wallis ANOVA. **D:** Representative images of HEK STIM1/2$^{-/-}$ co-transfected with STIM2.2-mCherry (red) and YFP-STIM2.2Δ674 (green; left) or YFP-STIM2.2Δ5K (green, right) and merged images under resting conditions. Scale bar indicates 10 μm. **E:** Co-localization analysis of cells from (D). For each condition 16-29 cells from 3 independent transfections were analyzed using Mander's overlapping coefficients (M1, M2) (mean+SEM): STIM2.2+Δ674 M1: 0.48 M2: 0.37; STIM2.2+Δ5K M1: 0.58 M2: 0.45. Mander's overlap coefficients of YFP-STIM2.2 and STIM2.2-mCherry transfected cells are indicated by grey bars, M1: 0.90 M2: 0.92. * p < 0.05; *** p < 0.001, Mann-Whitney test.

4.3.5 C-terminal EB binding motifs mediate negative SOCE phenotype of Δ5K

The negative effect of STIM2.2Δ5K on SOCE suggests an inhibitory binding partner or C-terminal folding responsible for the observed phenotype. In full-length STIM2, there are two EB binding sites (S-x-I-P) within the Ser/Pro rich region lacking in STIM2.3. End binding (EB) proteins track the plus-ends of growing microtubules facilitating movement of STIM1 within the ER membrane under resting conditions. However, EB1 binding diminishes translocation of STIM1 to ER PM junctional regions preventing excess Ca^{2+} influx. Association of STIM1 and EB1 was disrupted by mutation of isoleucine and proline within the S/T-x-I-P motif to asparagine [Chang et al. 2018]. Pulldown experiments confirmed binding of EB3 to STIM2 under resting conditions, which was abolished by the same mutation of the S-x-I-P motif as in STIM1 [Pchitskaya et al. 2017]. In contrast to Pchitskaya et al. (2017) only analyzing the first Eb binding site, either one or both binding motifs within full-length STIM2.2 or STIM2.2Δ5K were mutated as described in Pchitskaya et al. (2017) to investigate the role of potential microtubular tracking on STIM2-mediated SOCE (Fig. 17A). Since SH-SY5Y cells endogenously express all three EB isoforms (EB1, EB2, EB3), SH-SY5Y STIM1/2$^{-/-}$ cells were transfected with either YFP-STIM2.2, YFP-STIM2.3, YFP-STIM2.2Δ5K, the single (YFP-STIM2.2 IP_NN) or double IP mutant (YFP-STIM2.2 2xIP) or YFP-STIM2.2 2xIP+Δ5K. Quantification of resting Ca^{2+} levels and the SOCE parameters influx rate, Δpeak and Δplateau are displayed as fold change normalized to STIM2.2. SH-SY5Y STIM1/2$^{-/-}$ cells showed no Ca^{2+} influx with mock transfection (Fig. 27C), which was rescued by expression of YFP-STIM2.2. Expression of YFP-STIM2.3 led to the previously observed enhanced SOCE with significantly increased influx rate, Δpeak and Δplateau compared to STIM2.2. While the single mutation of either EB binding motif reduced SOCE with significantly reduced influx rate, Δpeak and Δplateau, the double mutation (STIM2.2 2xIP) did not affect Ca^{2+} influx compared to wildtype STIM2.2 (Fig. 17B,C). Interestingly, STIM2.3 and both single mutations displayed reduced resting Ca^{2+} levels (Fig. 17C). Moreover, neither mutation of the EB binding motifs reproduced the STIM2.3 gain-of-function phenotype.
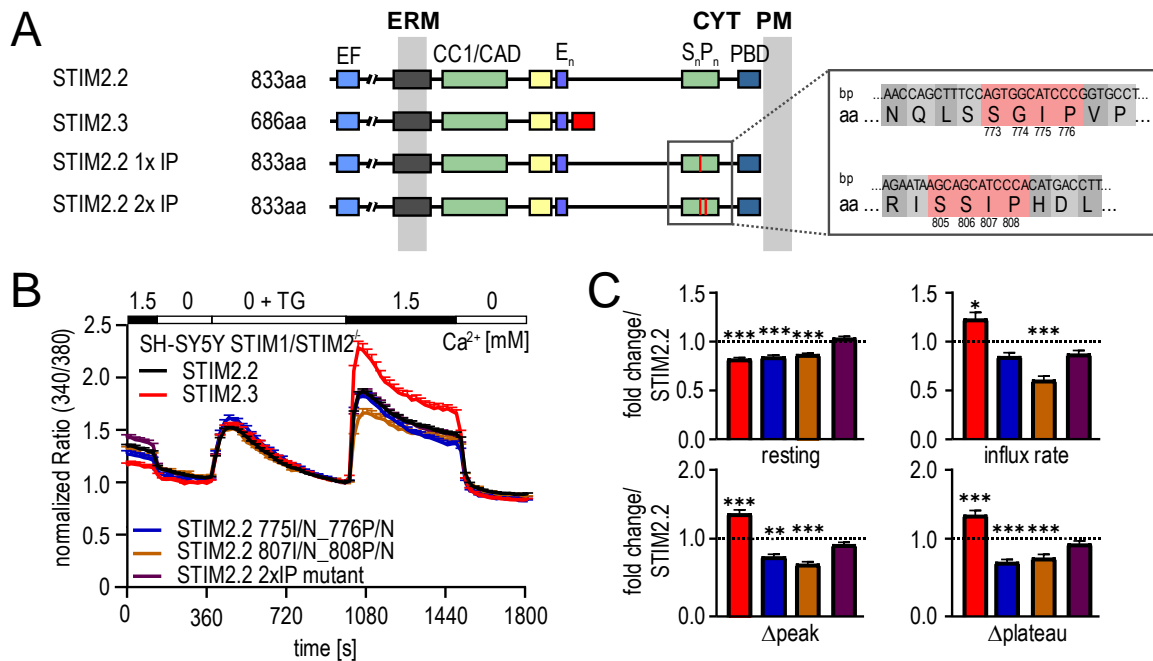
Figure 17 Mutation of EB binding motifs did not reproduce STIM2.3 mediated SOCE phenotype.
A: Schematic protein structure with functional domains of STIM2.2, STIM2.3 and the STIM2.2 IP mutants. EB binding motifs are indicated in red within the S_n/P_n rich region. Corresponding sequence (bp and aa) information is displayed in the grey box (right) with relevant aa indicated in red and corresponding aa position. **B**: Normalized average traces showing changes (mean+SEM) in intracellular Ca^{2+} (Ratio 340/380) over time in response to perfusion of different external Ca^{2+} [mM] as indicated in the upper bar in SH-SY5Y STIM1/2$^{-/-}$ cells transfected with YFP-STIM2.2 (black, n=198), YFP-STIM2.3 (red, n=130), the single IP mutants I775N/P776N (blue, n=162) and I807N/P808N (brown, n=184) or STIM2.2 2xIP (violet, n=158). **C**: Quantification of changes in resting Ca^{2+}, influx rate, Δpeak and Δplateau measured in B as fold change normalized to STIM2.2. *** p< 0.001, ** p< 0.01, * p< 0.05; Kruskal-Wallis ANOVA.

However, to investigate whether microtubular binding is responsible for the negative effect on SOCE observed with STIM2.2Δ5K, both EB binding motifs were mutated in combination with deletion of the PBD (STIM2.2 2xIP+Δ5K) (Fig. 18A). Surprisingly, the simultaneous mutation of both EB binding motifs in STIM2.2 2xIP+Δ5K rescued the negative effect on SOCE observed with STIM2.2Δ5K with no significant differences on influx rate and Δplateau, but slightly reduced Δpeak compared to STIM2.2. In contrast, deletion of the PBD (STIM2.2Δ5K) alone drastically reduced SOCE with significantly reduced influx rate, Δpeak and Δplateau (Fig. 18B,C). These results indicate competitive functions of EB binding and the PBD in regulating STIM2 functions, with microtubular tracking negatively affecting STIM2 mediated SOCE. Interestingly, all STIM2 proteins lacking the PBD showed significantly reduced resting Ca^{2+} levels compared to STIM2.2 demonstrating that not only pre-clustering but also basal activity of STIM2 under resting conditions is regulated by the PBD.
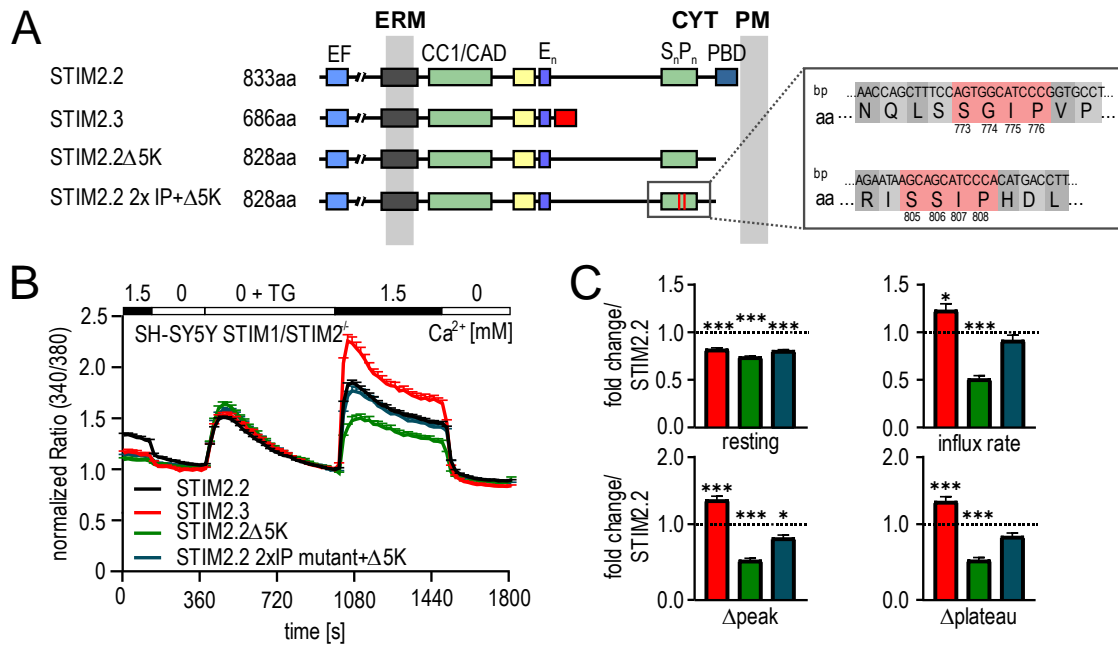
Figure 18 Simultaneous mutation of both EB binding motifs rescued the negative effect of STIM2.2Δ5K on SOCE. A: Schematic protein structure with functional domains of STIM2.2, STIM2.3, STIM2.2Δ5K and STIM2.2 2xIP+Δ5K. EB binding motifs are indicated in red within the S_n/P_n rich region. Corresponding sequence (bp and aa) information is displayed in the grey box (right) with relevant aa indicated in red and corresponding aa position. B: Normalized average traces showing changes (mean+SEM) in intracellular Ca^{2+} (Ratio 340/380) over time in response to perfusion of different external Ca^{2+} [mM] as indicated in the upper bar in SH-SY5Y STIM1/2$^{-/-}$ cells transfected with YFP-STIM2.2 (black, n=198), YFP-STIM2.3 (red, n=130), YFP-STIM2.2Δ5K (green, n=214) or STIM2.2 2xIP+Δ5K (petrol blue, n=168). C: Quantification of changes in resting Ca^{2+}, influx rate, Δpeak and Δplateau measured in B as fold change normalized to STIM2.2. *** $p < 0.001$, * $p < 0.05$; Kruskal-Wallis ANOVA.

4.3.6 Absence of the PBD reduces cluster formation

The PBD functions as an anchor to attach STIM proteins to phospholipids at the inner leaflet of the PM upon activation. To further examine cluster formation, HEK STIM1/2$^{-/-}$ cells were transfected with YFP-STIM2.3, YFP-STIM2.2 or the mutants lacking the PBD (YFP-STIM2.2Δ5K) and EB binding sites (YFP-STIM2.2 2xIP+Δ5K) using a PIP$_2$ sensor (PH-PLC-mCherry) as a PM marker (Fig. 19A). All proteins naturally or artificially lacking the PBD, i.e. STIM2.3, STIM2.2Δ5K and STIM2.2 2xIP+Δ5K, showed an ER distribution at rest and reduced Tg-induced cluster formation despite their previously described differential SOCE phenotype. In contrast, STIM2.2 was already pre-clustered under basal conditions and displayed prominent clustering after store depletion. All proteins lacking the PBD showed significantly reduced cluster sizes and integrated densities compared to STIM2.2 as quantified in Fig. 19B.
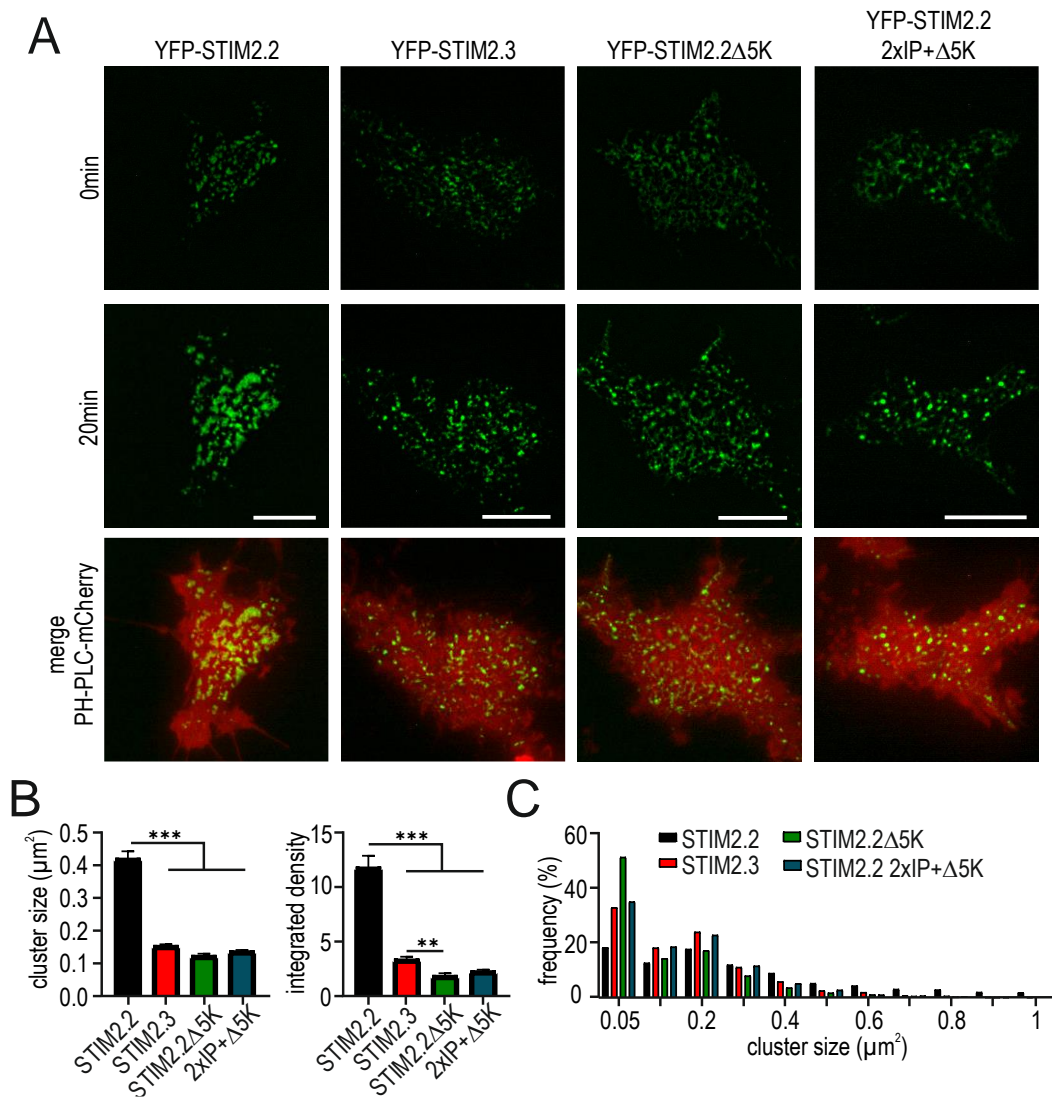
Figure 19 Absence of PBD reduces cluster formation and cluster size. A: Representative images of HEK STIM1/2$^{-/-}$ cells co-transfected with PH-PLC-mCherry (red) and YFP-STIM2.2 (green), YFP-STIM2.3 (green), YFP-STIM2.2Δ5K (green) or YFP-STIM2.2 2xIP+Δ5K (green) before (0min) and after (20min) stimulation with Tg. Scale bar indicates 10 μm. **B**: Quantification of cluster size (μm^2) and integrated density measured in A. For each condition 34-50 cells from 3 independent transfections were analyzed. *** p< 0.001, ** p< 0.01, Kruskal-Wallis ANOVA. **C**: Cluster size distribution (frequency %) from cells measured in A.

Accordingly, cluster size distribution is shifted towards smaller values in cells expressing YFP-STIM2.3, YFP-STIM2.2Δ5K and YFP-STIM2.2 2xIP+Δ5K, while larger cluster sizes as seen with STIM2.2 are absent, respectively (Fig. 19C). Tracking of STIM2.2Δ5K along microtubules was not detected in HEK STIM1/2$^{-/-}$ cells. These results indicate, that full-length STIM2 may not track along microtubules due to its sensitive EF hand and subsequent pre-clustering. However, PBD-mediated anchoring of STIM2 at the PM is not a prerequisite for Tg induced ORAI activation.

4.3.7 Additional C-terminal deletions did not reproduce STIM2.3 mediated SOCE phenotype

To further characterize the underlying mechanism of the increased SOCE phenotype, additional mutants with several C-terminal deletions were generated. The mutant STIM2.2Δ711 terminates after amino acid 711 lacking the Ser/Pro rich region and the PBD (Fig. 20A). Ca^{2+} imaging experiments showed significant reduction in resting Ca^{2+} levels with STIM2.2Δ711, but no significant effect on SOCE after Ca^{2+} readdition with similar influx rate, Δpeak and Δplateau as STIM2.2 (Fig. 20B,C). Interestingly, the slightly shorter deletion in STIM2.2Δ711 is not sufficient to reproduce the STIM2.3 mediated phenotype in contrast to STIM2.2Δ674 only lacking additional 36 amino acids. The differential phenotypes of the C-terminal deletions suggest that these 36 amino acids may be involved in the observed gain-of-function SOCE phenotype.
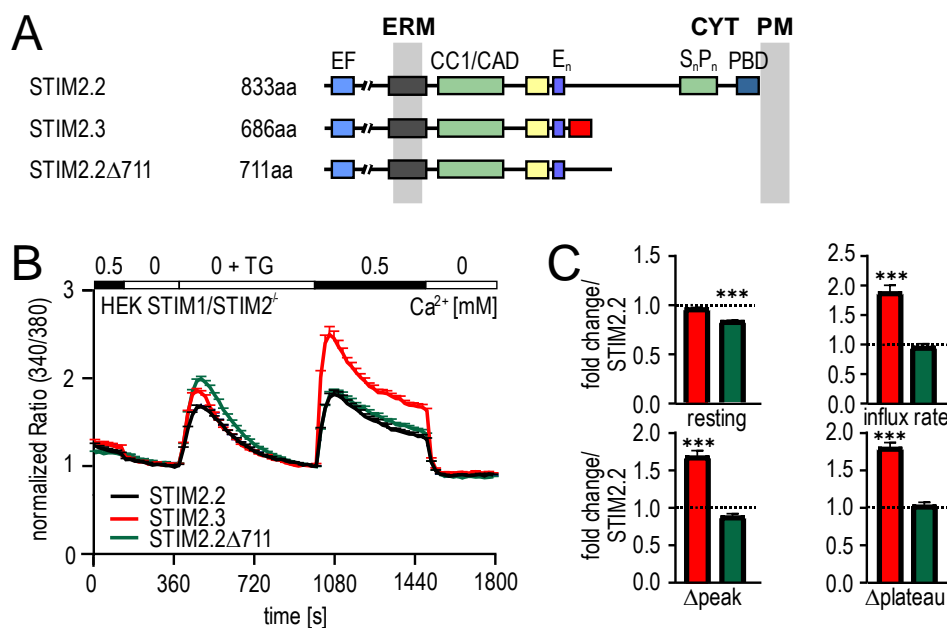
Figure 20 C-terminal deletion at amino acid 711 did not affect STIM2.2 mediated SOCE. A: Schematic protein structure with functional domains of STIM2.2, STIM2.3 and STIM2.2Δ711 terminating after aa 711. **B**: Normalized average traces of intracellular Ca^{2+} (Ratio 340/380) over time in response to perfusion with different external Ca^{2+} [mM] as indicated in the upper bar after transfection with YFP-STIM2.2 (black, n=165), YFP-STIM2.3 (red, n=207) or YFP-STIM2.2Δ711 (green, n=187) in HEK STIM1/2$^{-/-}$ cells. **C**: Quantification of changes in resting Ca^{2+}, influx rate, Δpeak and Δplateau measured in B as fold change normalized to STIM2.2. *** p< 0.001; Kruskal-Wallis ANOVA.

Therefore, mutants internally lacking these 36 aa (STIM2.2Δ675-710+X) were generated in the background of STIM2.2, STIM2.2 2xIP and STIM2.2 2xIP+Δ5K (Fig. 21A). Ca^{2+} imaging experiments were performed using HEK STIM1/2$^{-/-}$ transfected with YFP-STIM2.2, YFP-STIM2.3 and either YFP-STIM2.2Δ675-710+X mutant. Remarkably, the mutant only lacking the internal amino acids STIM2.2Δ675-710 and the deletion mutant with additional mutation of both EB binding motifs STIM2.2Δ675-710+2xIP displayed increased resting Ca^{2+} levels, but reduced SOCE with significantly reduced Δpeak and Δplateau, but no effect on influx rate compared to STIM2.2. In contrast, the mutant with deletion of the internal amino acids as well as the PBD in combination with mutation of both EB binding motifs STIM2.2Δ675-710+2xIP+Δ5K displayed reduced resting Ca^{2+} levels but did not alter SOCE compared to wildtype STIM2.2 (Fig. 21B,C). Neither of these mutants did reproduce the increased SOCE phenotype observed with STIM2.3. The reduced SOCE of the deletion mutants, that still contain the PBD, suggests an artificially induced backfolding of the positively charged PBD onto the negatively charged poly E or inhibitory domain, which was not observed in
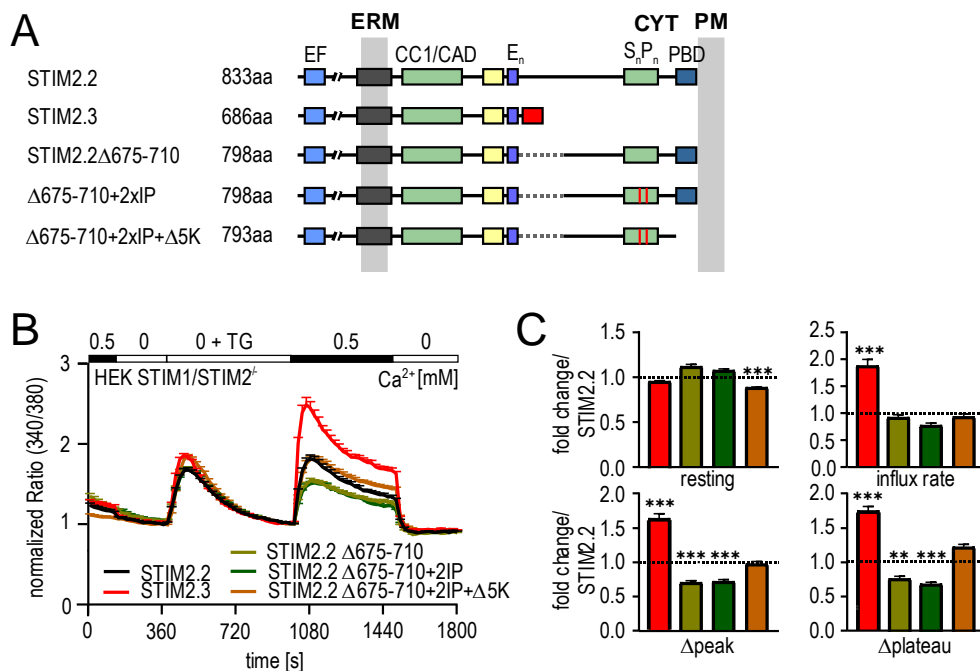

Figure 21 The internal deletion Δ675-710 reduced SOCE in the presence of the PBD. A: Schematic protein structure with functional domains of STIM2.2, STIM2.3, and the mutants lacking the internal aa 675-710. Mutation of the EB binding motifs are indicated in red within the S_n/P_n rich region. **B**: Normalized average traces of intracellular Ca^{2+} (Ratio 340/380) over time in response to perfusion with different external Ca^{2+} [mM] as indicated in the upper bar after in HEK STIM1/2$^{-/-}$ cells transfected with YFP-STIM2.2 (black, n=76), YFP-STIM2.3 (red, n=53), STIM2.2Δ675-710 (light green, n=117), YFP-STIM2.2Δ675-710+2xIP (dark green, n=140) or YFP-STIM2.2Δ675-710+2xIP+Δ5K (brown, n=157). **C**: Quantification of changes in resting Ca^{2+}, influx rate, Δpeak and Δplateau measured in B as fold change normalized to STIM2.2. *** $p < 0.001$, ** $p < 0.01$; Kruskal-Wallis ANOVA

STIM2.2Δ675-710+2xIP+Δ5K additionally lacking the PBD. However, this does not explain the increased resting Ca^{2+} levels.

4.3.8 External H_2O_2 did not significantly reduce STIM2 mediated SOCE

Reactive oxygen species such as H_2O_2 do not only cause oxidative damage to DNA, proteins and lipids, but rather function as intracellular signaling molecules at low concentrations [reviewed in Auten and Davis 2009]. In addition to phosphorylation, ROS-induced redox modification of reactive cysteines regulates protein function by reversibly altering its redox state [Sauer et al. 2001]. Compared to STIM1, STIM2 contains ten additional cysteine residues within its C-terminal region suggesting increased susceptibility for redox modifications. In 2020, Gibhardt et al. identified within the STIM2 CC1 domain C313 as the critical residue sensitive to thiol oxidation leading to altered STIM2 activation and SOCE inhibition. Compared to STIM2.2, the C-terminal truncated STIM2.3 is lacking five of these ten additional cysteines but in addition it contains two extra cysteines within its short specific domain. In ORAI1, residue C195 at the transmembrane region 3 (TM3), which is absent in ORAI3, is responsible for H_2O_2-induced current inhibition by interacting with S239 in TM4 [Alansary et al. 2016]. To exclude the inhibitory effect of extracellular H_2O_2 on ORAI1-mediated SOCE, the ORAI1 triple cysteine mutant (TCM) insensitive to oxidation was used for the following experiments. To investigate whether STIM2.3 is less redox sensitive and whether the two additional cysteines regulate STIM2.3 function, Ca^{2+} imaging experiments were performed using HEK ORAI1/2/3$^{-/-}$ cells transfected with YFP-STIM2.2, YFP-STIM2.3 or YFP-STIM2.2Δ674 and ORAI1-TCM-IRES-RFP in a 3:1 ratio. To induce oxidative stress, 1 mM H_2O_2 was added to the extracellular 0 mM Ca^{2+} ringer containing Tg and 0.5 mM Ca^{2+} ringer solution. Incubation with H_2O_2 reduced STIM2.2 mediated SOCE with only significantly reduced influx rate but did not alter Δpeak and Δplateau compared to the condition without H_2O_2 (Fig. 22). Interestingly, H_2O_2 did not drastically affect SOCE in cells expressing STIM2.3 or its phenotype-mimicking mutant STIM2.2Δ674. For STIM2.3, only Δplateau was significantly reduced while influx rate and Δpeak were not affected by H_2O_2. Moreover, incubation with H_2O_2 did not significantly affect STIM2.2Δ674 mediated SOCE (Fig. 22).
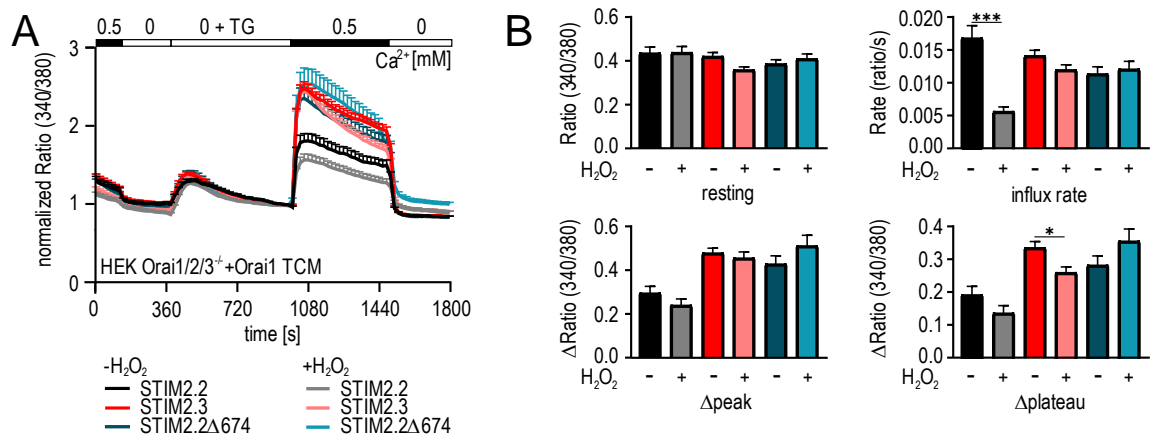
Figure 22 External H₂O₂ did not significantly reduce STIM2.2- or STIM2.3-mediated SOCE. A: Normalized average traces of intracellular Ca²⁺ (Ratio 340/380) over time in response to perfusion with different external Ca²⁺ [mM] as indicated in the upper bar after transfection with Orai1 TCM-IRES-RFP and YFP-STIM2.2 (black, n=30; grey, n=26), YFP-STIM2.3 (red, n=94; light red, n=77) or YFP-STIM2.2Δ674 (blue, n=58; light blue, n=41) in the absence (dark colors) or presence (light colors) of external H₂O₂. **B**: Quantification of changes in resting Ca²⁺, influx rate Δpeak and Δplateau measured in A. *** p< 0.001, * p< 0.05; Kruskal-Wallis ANOVA

In conclusion, the STIM2.3 gain-of-function phenotype is independent of the splice-specific residues and was only reproduced by the larger C-terminal deletion (Δ674). Neither mutation of both EB binding motifs nor the shorter or internal C-terminal deletion were sufficient to mimic the phenotype observed with STIM2.3. Notably, loss of the PBD does not necessarily negatively affect Tg induced Ca²⁺ influx in the absence of MBP attachment sites, but rather reduces STIM2-characteristic pre-clustering under resting conditions and Tg induced cluster formation. However, PBD mediated anchoring of STIM2 at the PM is not a prerequisite for ORAI activation upon full store depletion.

4.4 Voltage-gated calcium entry in SH-SY5Y STIM$^{-/-}$ cell lines

4.4.1 STIM knockout increases voltage-gated Ca^{2+} entry

The neuroblastoma cell line SH-SY5Y derived from human sympathetic neuronal tissue endogenously express functional voltage-gated Ca^{2+} channels (VGCC, Ca$_v$) and their auxiliary subunits providing a useful in vitro model to study neurotransmission [Sousa et al. 2013]. STIM1 inhibits the L-type Ca^{2+} channel Ca$_v$1.2 in a negative feedback mechanism coupling the filling state of the ER to voltage-gated Ca^{2+} entry [Park et al. 2010; Youjun Wang et al. 2010; Dittmer et al. 2017]. To investigate the influence of both STIM homologues on VGCE, expression levels of the pore-forming α-subunit of the L-type Ca$_v$1.2 (CACNA1C) and Ca$_v$1.3 (CACNA1D), the N-type Ca$_v$2.2 (CACNA1B) and the T-type Ca$_v$3.1 (CACNA1G) were quantified in SH-SY5Y STIM$^{-/-}$ and WT cells using RNA sequencing and qRT-PCR (Fig. 23A,B). In WT cells, all analyzed CACNA genes are at a relatively similar low expression level using RNA sequencing, while qRT-PCR data identified Ca$_v$2.2 as the most abundant VGCC. For SH-SY5Y STIM1$^{-/-}$, RNA sequencing
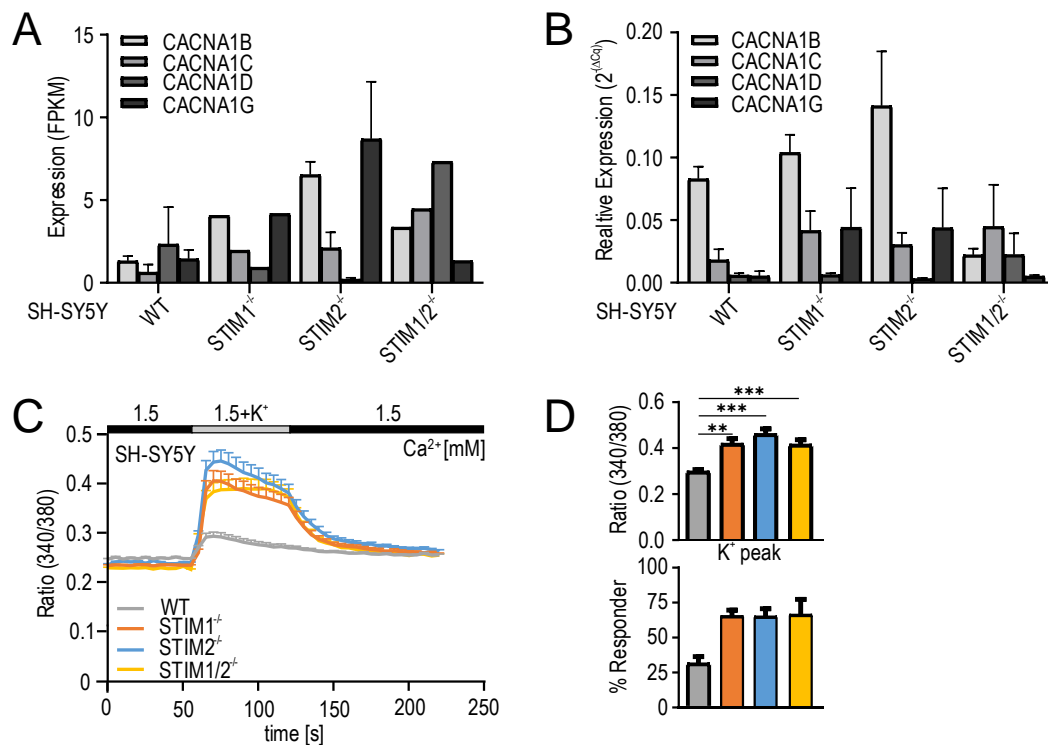

Figure 23 STIM knockout increases K$^+$ induced VGCE in SH-SY5Y cells. A: FPKM values of CACNA genes as indicated in SH-SY5Y wild-type, STIM1-, STIM2- or STIM1/2-deficient cells from RNA Seq analysis. **B**: Relative expression of CACNA genes in SH-SY5Y WT or STIM-/-. Data is displayed as mean+SEM from 3 independent qRT-PCR. **C**: Average traces of changes in intracellular Ca^{2+} (Ratio340/380) over time after perfusion of different external Ca^{2+} [mM] as indicated in the upper bar in SH-SY5Y WT (grey, n=150), STIM1$^{-/-}$ (orange, n=149), STIM2$^{-/-}$ (blue, n=150) or STIM1/2$^{-/-}$ (yellow, n=150) cells. **D**: Quantification of K$^+$ peak and % Responder measured in A. *** p< 0.001, ** p< 0.01, * p< 0.05; Kruskal-Wallis ANOVA

and qRT-PCR display similar results with $Ca_v2.2$ being the most abundant channel. For SH-SY5Y STIM2$^{-/-}$, the results are slightly different. While in RNA sequencing, $Ca_v3.1$ showed the highest FKPM value, qRT-PCR identified $Ca_v2.2$ as the predominantly expressed VGCC. In SH-SY5Y cells lacking both, STIM1 and STIM2, expression levels of the analyzed CACNA genes are similar using RNA sequencing or qRT-PCR. VGCE was analyzed in SH-SY5Y STIM$^{-/-}$ and WT cells using an external high potassium (K$^+$) Ca^{2+} ringer solution, which leads to membrane depolarization shifting the negative resting membrane potential to ~10 mV. Ca^{2+} imaging experiments revealed that knockout of STIM1, STIM2 or both homologues significantly increased K$^+$-induced Ca^{2+} influx which may have been due to an increased number of cells responding to K$^+$-mediated depolarization compared to WT cells (Fig. 23C,D).

4.4.2 Effect of STIM2 OE on K$^+$ induced Ca^{2+} influx

Recently, Ramesh et al. (2021) showed that re-expression of the STIM1 variants, STIM1 and STIM1B, had only little effect on K$^+$-induced Ca^{2+} influx in SH-SY5Y STIM1$^{-/-}$ cells. In contrast, previous reports demonstrated a negative feedback regulation of voltage-gated channel $Ca_v1.2$ by STIM1 [Park et al. 2010; Youjun Wang et al. 2010; Dittmer et al. 2017]. To examine the effect of STIM2 on VGCE, Ca^{2+} imaging experiments were performed
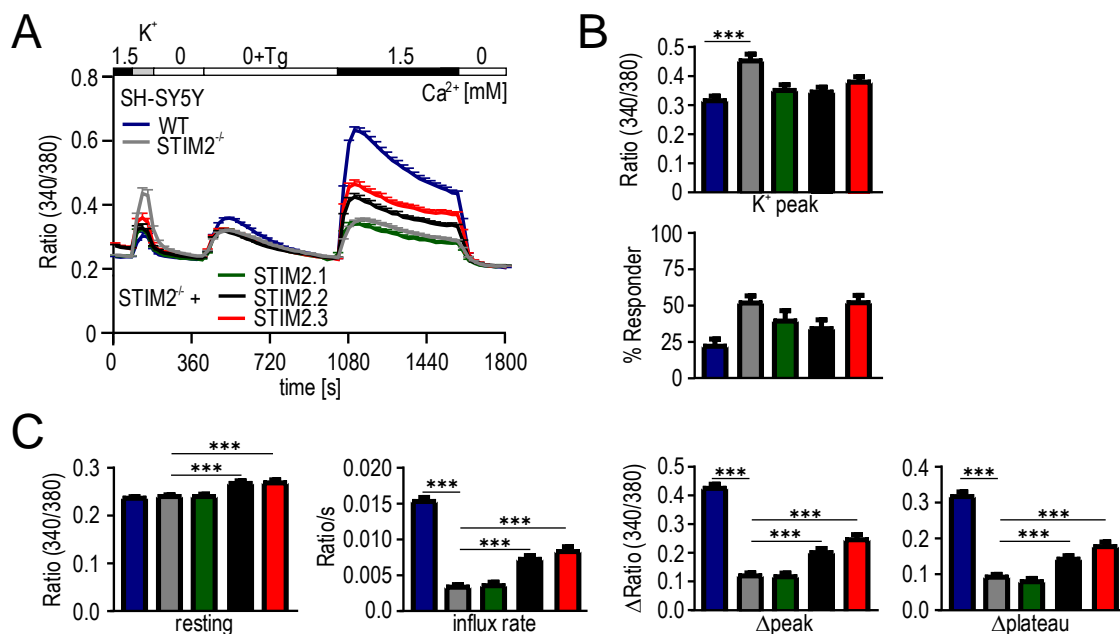

Figure 24 Overexpression of STIM2 reduces K$^+$ induced Ca^{2+} influx. A: Average traces of changes in intracellular Ca^{2+} (Ratio 340/380) over time in response to perfusion with different external Ca^{2+} [mM] as indicated in the upper bar in SH-SY5Y WT (blue, n=208), STIM2$^{-/-}$ (grey, n=213) or STIM2$^{-/-}$ cells transfected with YFP-STIM2.1 (green, n=105), YFP-STIM2.2 (black, n=113) or YFP-STIM2.3 (red, n=111). **B**: Quantification of K$^+$ peak and % Responder measured in A. **C**: Quantification of changes in resting Ca^{2+}, influx rate, Δpeak and Δplateau measured in A. *** p< 0.001; Kruskal-Wallis ANOVA.

using SH-SY5Y STIM2$^{-/-}$ cells transfected with STIM2.1, STIM2.2 or STIM2.3. After baseline recording, a short depolarization stimulus using an external high K$^+$ containing Ca^{2+} ringer solution was followed by the Ca^{2+} readdition protocol. K$^+$ peak and % Responder as well as the SOCE parameters influx rate, Δpeak and Δplateau were quantified (Fig. 24). As previously shown, knockout of STIM2 increased K$^+$ peak and % Responder while decreasing SOCE with significantly reduced influx rate, Δpeak and Δplateau compared to WT cells. Heterologous expression of either STIM2.1, STIM2.2 or STIM2.3 in SH-SY5Y STIM2$^{-/-}$ cells partially reduced K$^+$ peak to the level of WT cells, while the number of cells responding to depolarization was only slightly reduced compared to SH-SY5Y STIM2$^{-/-}$ cells. Both STIM2.2 and STIM2.3 significantly increased resting Ca^{2+} levels, influx rate, Δpeak and Δplateau, while the inhibitory STIM2.1 had no significant effect on resting Ca^{2+} levels and SOCE compared to SH-SY5Y STIM2$^{-/-}$ cells. In conclusion, these results indicate a negative feedback regulation of voltage-gated and store-operated Ca^{2+} entry in SH-SY5Y cells.
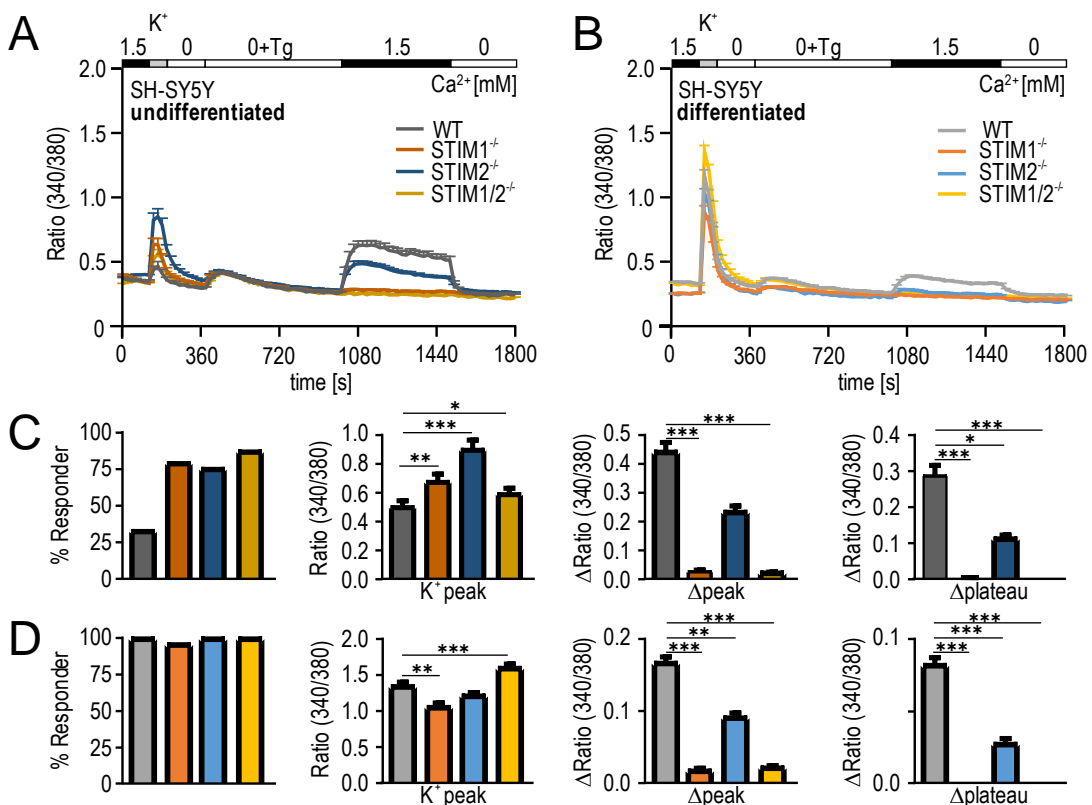
4.4.3 Differentiation of SH-SY5Y cells alters SOCE and VGCE

SH-SY5Y cells can be differentiated into a more mature neuron-like phenotype leading to expression of neuronal markers and change in morphology. For differentiation, a modified protocol as described in Pezzini et al. (2017) was used. To analyze the effect of differentiation on VGCE and SOCE, SH-SY5Y WT and STIM$^{-/-}$ cells were treated with retinoic acid for seven days followed by incubation of BDNF for additional two days. While undifferentiated cells displayed only a few truncated processes, differentiation induced elongation and branching (Fig. 25).
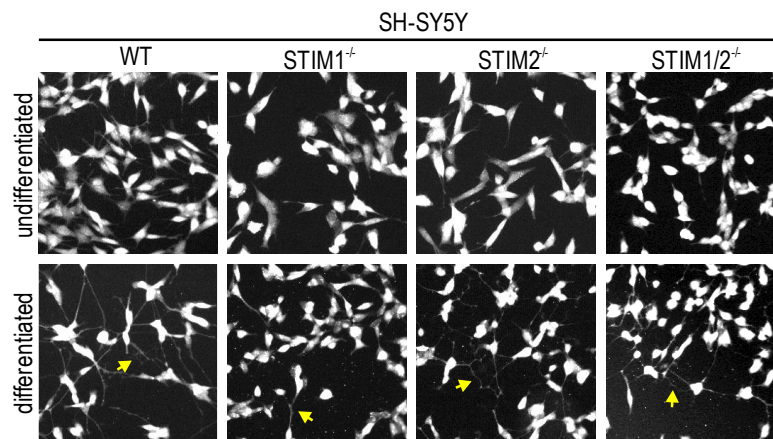
Figure 25 Morphological changes of SH-SY5Y cells after differentiation. A: Representative images of the morphology of undifferentiated (upper panel) or differentiated (lower panel) SH-SY5Y WT or STIM-deficient cells loaded with Fura2. Yellow arrows indicate cell processes.

To analyze the effect of differentiation on VGCE and SOCE in SH-SY5Y WT and STIM$^{-/-}$ cells, Ca^{2+} imaging experiments were performed. After baseline recording, a short depolarization stimulus using an external high K$^+$ containing Ca^{2+} ringer solution was followed by the Ca^{2+} readdition protocol. K$^+$ peak and % Responder as well as the SOCE parameters Δpeak and Δplateau were quantified. In undifferentiated SH-SY5Y STIM$^{-/-}$ cells, % Responder and K$^+$ peak were increased, while SOCE parameters were reduced with significantly reduced Δpeak and Δplateau compared to WT cells (Fig. 26A,C). Upon differentiation, the number of cells responding to depolarization (% Responder) increased in all analyzed cell lines to almost 100 %. At the same time, K$^+$ induced Ca^{2+} influx increased after differentiation but no longer showed potential STIM-mediated inhibition of VGCE (Fig. 26B,D). While SH-SY5Y STIM1 $^{-/-}$ cells showed significantly reduced K$^+$ peak, SH-SY5Y STIM1/2$^{-/-}$ cells showed significantly increased K$^+$ influx compared to WT cells. In differentiated cells, SOCE was almost absent with significantly reduced Δpeak and Δpeak in SH-SY5Y STIM$^{-/-}$ compared to WT. Even though expression levels of VGCC and SOCE components were not quantified, these results suggest that

Figure 26 Differentiation alters SOCE and VGCE in SH-SY5Y cells. A-B: Average traces of changes in intracellular Ca^{2+} (Ratio340/380) over time in response to perfusion with different external Ca^{2+} [mM] as indicated in the upper bar in undifferentiated (A) and differentiated (B) SH-SY5Y WT (grey, n=51; 48), STIM1$^{-/-}$ (orange, n=50; 50), STIM2$^{-/-}$ (blue, n=50; 50) or STIM1/2$^{-/-}$ (yellow, n=52; 50) cells. **C-D**: Quantification of % Responder, K$^+$ peak, Δpeak and Δplateau measured in A-B of undifferentiated (C) and differentiated (D) SH-SY5Y cells.

after differentiation Ca$_v$, STIM and ORAI are differentially expressed or regulated. Rather, STIM no longer appears to regulate VGCE in any direct or indirect manner.

4.5 Potential physiological functions of STIM2.3

4.5.1 STIM2 PBD is not necessarily required for NFAT translocation

One of the most prominent physiological processes triggered by STIM mediated Ca^{2+} influx is activation followed by nuclear translocation of the transcription factor NFAT. In 2020, Son et al. showed that STIM2 promotes assembly of the signalosome complex consisting of STIM1, ORAI1, calcineurin and the scaffolding protein AKAP79, thereby coupling Ca^{2+} influx through ORAI1 to NFAT1 activation [Son et al. 2020; Kar, Lin, et al. 2021]. While deletion of the PBD in STIM1, which attenuates NFAT1 translocation, was rescued by STIM2 over-expression, replacement of the PBD in STIM1 with that of STIM2 eliminated the requirement of STIM2 for NFAT1 translocation [Son et al. 2020]. To investigate whether the PBD is required for STIM2 induced NFAT1 translocation independent of STIM1, SH-SY5Y STIM1/2$^{-/-}$ cells were transfected with NFAT1-GFP and mKate2-STIM2.2, mKate2-STIM2.3, mKate2-STIM2.2Δ5K, mKate2-STIM2.2 2xIP+Δ5K or empty vector (mKate2) (Fig. 27A). NFAT1 translocation into the nucleus was quantified before and after store depletion and the corresponding Ca^{2+} influx was quantified as area under the curve (AUC). No SOCE and translocation were observed for mock transfected cells (mKate2) after store depletion indicating that Ca^{2+} efflux from the ER is not sufficient for NFAT1 activation. Under resting conditions, STIM2.2 already led to a significantly increased NFAT1 translocation in contrast to STIM2.3, STIM2.2Δ5K and the STIM2.2 2xIP+Δ5K mutant, which showed no basal translocation compared to control transfected cells. While STIM2.2 mediated translocation was only slightly increased, STIM2.3 showed significantly increased NFAT1 translocation after store depletion to the same extent as STIM2.2 (Fig. 27A,B). These results demonstrate that NFAT1 activation does not linearly correlate with Ca^{2+} influx, which is significantly increased with STIM2.3 compared to STIM2.2 (Fig. 27C,D). Deletion of the PBD (STIM2.2Δ5K) abolished Tg-induced NFAT translocation due to the negative effect on SOCE, which were both rescued by the simultaneous mutation of both EB binding motifs in combination with deletion of the PBD (STIM2.2 2xIP+Δ5K) (Fig. 27B,C). Analysis of resting Ca^{2+} levels demonstrated that basal NFAT1 activation as seen with STIM2.2 is not dependent on

resting Ca^{2+} influx, which was significantly increased in STIM2.2, STIM2.3 and STIM2.2 2xIP+Δ5K transfected cells (Fig. 27D). Rather, basal NFAT translocation is regulated by the PBD, which most likely stabilizes the signalosome complex under resting conditions.
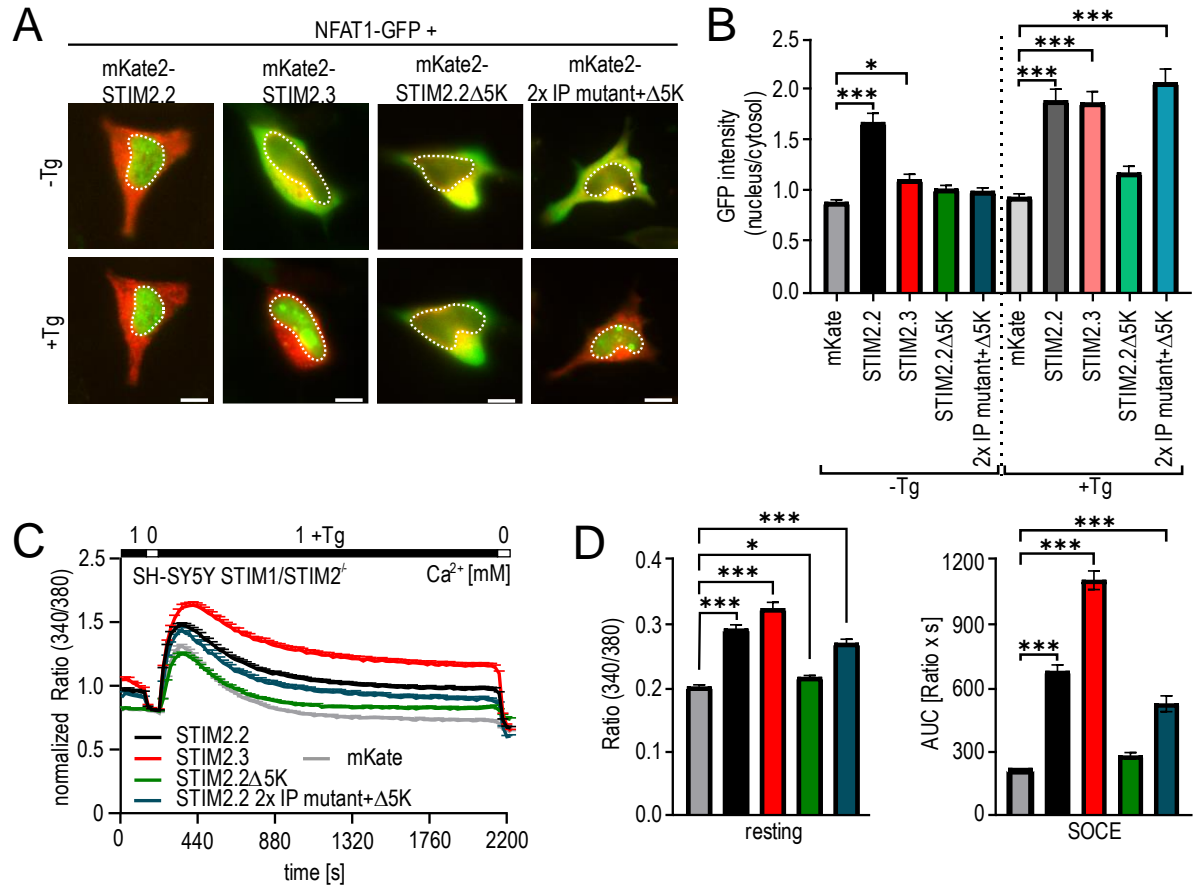
Figure 27 PBD is not necessarily required for activation-induced STIM2-mediated NFAT translocation in the absence of MBP attachment sites. A: Representative images of SH-SY5Y STIM1/2$^{-/-}$ cells transfected with NFAT1-GFP (green) and mKate2-STIM2.2 (red), mKate2-STIM2.3 (red), mKate2-STIM2.2Δ5K (red) or mKate2-STIM2.2 2xIP+Δ5K (red) before (upper panel, -Tg) and after (lower panel, +Tg) stimulation with Tg. The white dotted line indicates the nucleus. Scale bar indicates 10 µm. **B**: Quantification of NFAT1 translocation into the nucleus (NFAT1-GFP N/C) measured in A. For each condition 39 - 114 cells were analyzed from 3 independent transfections. *** $p < 0.001$, * $p < 0.05$; Kruskal-Wallis ANOVA. **C**: Normalized average traces of intracellular Ca^{2+} (Ratio 340/380) over time in response to perfusion with different external Ca^{2+} [mM] as indicated in the upper bar of SH-SY5Y STIM1/2$^{-/-}$ cells transfected with mKate2-STIM2.2 (black, n=184), mKate2-STIM2.3 (red, n=160), mKate2-STIM2.2Δ5K (green, n=156), mKate2-STIM2.2 2xIP+Δ5K (blue, n=164) or empty vector, (mKate2, grey, n=241). **D**: Quantification of resting Ca^{2+} and area under the curve (AUC) measured in C.

4.5.2 Differential results for synaptotagmin 2 as a STIM2 interaction partner

In addition to functional characterization, the identification of interaction partners provides insights into a potential physiological function of a protein, its regulatory mechanisms and involvement in other cellular processes. In recent years, several interaction partners for STIM1 and STIM2 have been described such as POST, STIMATE or EB proteins, which regulate STIM function and shape SOCE-induced Ca^{2+} signals [Krapivinsky et al. 2011; Jing et al. 2015; Chang et al. 2018]. To investigate whether the C-terminal deletion in STIM2.3 prevents interaction with already known or so far unknown proteins, bimolecular fluorescence complementation as a fast-screening assay was performed using bait constructs of proteins, which have been already established for this method. In three independent experiments, no differential interaction partner was identified. Both STIM2.2 and STIM2.3 displayed similar interaction with all so far analyzed proteins. The strongest interaction was observed with STIM2, synaptotagmin 2
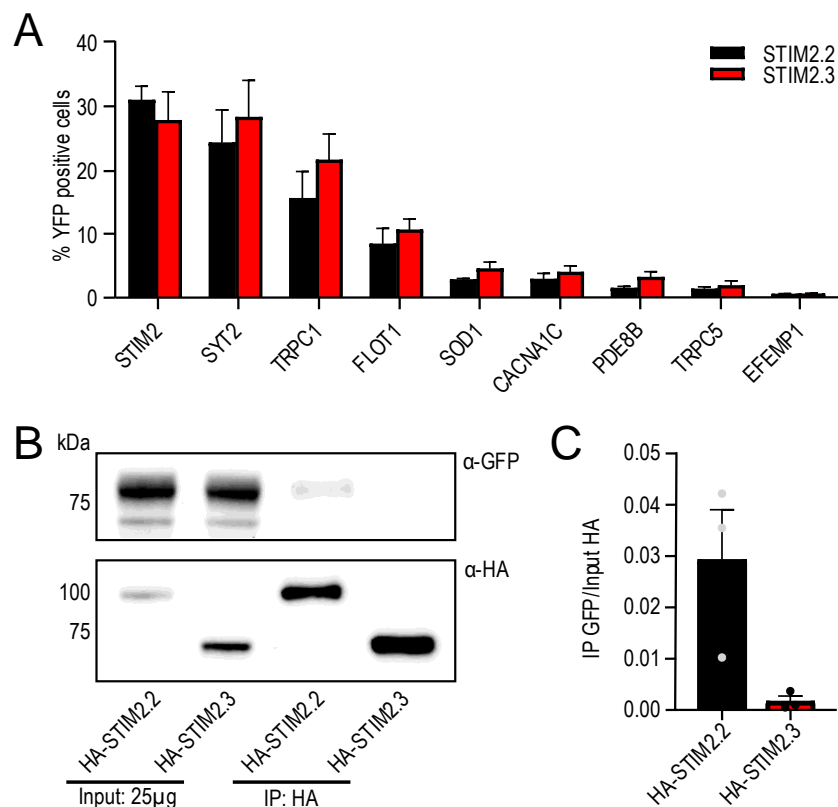

Figure 28 Differential results for synaptotagmin 2 as a interaction of STIM2. A: Interaction of STIM2.2-YFPc (black) or STIM2.3-YFPc (red) and POI-YFPn in HEK STIM1/2$^{-/-}$ was quantified as % YFP positive cells in flow cytometry using bimolecular fluorescence complementation. Data is displayed as mean+SEM obtained from 3 independent transfections. **B**: Co-immunoprecipitation using anti-HA agarose of HEK STIM1/2$^{-/-}$ transfected with HA-STIM2.2 or HA-STIM2.3 and Syt2-YFPn followed by Western blot and incubation with the indicated antibodies. **C:** Quantification of precipitated Syt2-YFPn from 3 independent transfections.

(Syt2) and the ion channel TRPC1 (transient receptor potential canonical 1) at ~ 15 - 30 % followed by flotilin1 (FLOT1) at ~10 %, superoxide dismutase1 (SOD1), phospho-diesterase 8B (PDE8B), TRPC5 and EFEMP1 at 2 – 5 % (Fig. 28A). As synaptotagmin 2 was one of the strongest hits, co-immunoprecipitation and Western Blot were performed to validate previous results. HEK STIM1/2$^{-/-}$ cells were transfected with HA-STIM2.2 or HA-STIM2.3 and Syt2-YFPn, which was also used in the BiFC experiments. Both STIM2 variants and synaptotagmin 2 were detected in the input lane using an anti-GFP or anti-HA antibody, respectively, confirming successful transfection and antibody specificity (Fig. 28B). In contrast to BiFC, STIM2 only showed a weak interaction with Syt2 with an IP/Input ratio of ~0.03 in pull down experiments. However, for STIM2.3, interaction with synaptotagmin 2 was not confirmed in IP experiments with an IP/Input ratio of precipitated Syt2 almost at 0 despite similar BiFC results as STIM2.2 (Fig. 28B,C). These results demonstrate that identified interaction partners can differ depending on the method and experimental conditions but are not necessarily mutually exclusive.

4.5.3 STIM2.3 shows reduced interaction with AMPKα

In 2019, Chauhan et al. identified STIM2 as a novel regulator of AMPK signaling. AMPK regulates energy homeostasis in response to energy stress and is phosphorylated at threonine 172 within the catalytic α-subunit upon activation. Ca^{2+} dependent activation of AMPK is mediated by the Ca^{2+}/Calmodulin dependent kinase kinase II which is activated by STIM2 via its CAD domain, which is identical for both STIM2.2 and STIM2.3 [Chauhan et al. 2019]. For AMPK, however, Chauhan et al. identified in STIM2 the C-terminal region spanning the amino acids 646 to 833 as the interacting domain. The last common amino acid between STIM2.2 and STIM2.3 is at position 674. Hence, it was not clear whether the truncated splice variant interacts with AMPK. To investigate whether the C-terminal deletion in STIM2.3 prevents interaction with and subsequent activation of AMPK, HEK STIM1/2$^{-/-}$ cells, which endogenously express AMPKα, were transfected with HA-STIM2.2 or HA-STIM2.3. To further elucidate whether the interaction is dependent on STIM2 activation, cells were stimulated with Thapsigargin to deplete the stores. Strikingly, pull down experiments revealed that STIM2.3 still interacts with the catalytic α-subunit of AMPK independent of the filling state of the ER (Fig. 29A,B).

However, STIM2.3 displayed a weaker interaction with AMPKα compared to STIM2.2 before and after store depletion (Fig. 29C). These results demonstrate that the interacting domain is overlapping with the region spanning the amino acids 646 to 674. Using a phosphorylation specific antibody, AMPKα activation was only detected in IP lanes indicating that phosphorylation requires direct interaction of STIM2.2 and STIM2.3 with AMPKα. As quantified in Fig. 29D, STIM2.3 led to a poorer AMPKα activation before and after store depletion compared to STIM2.2 demonstrating that AMPKα phosphorylation correlates with the direct interaction but does not correlate with the total amount of Ca^{2+} influx.
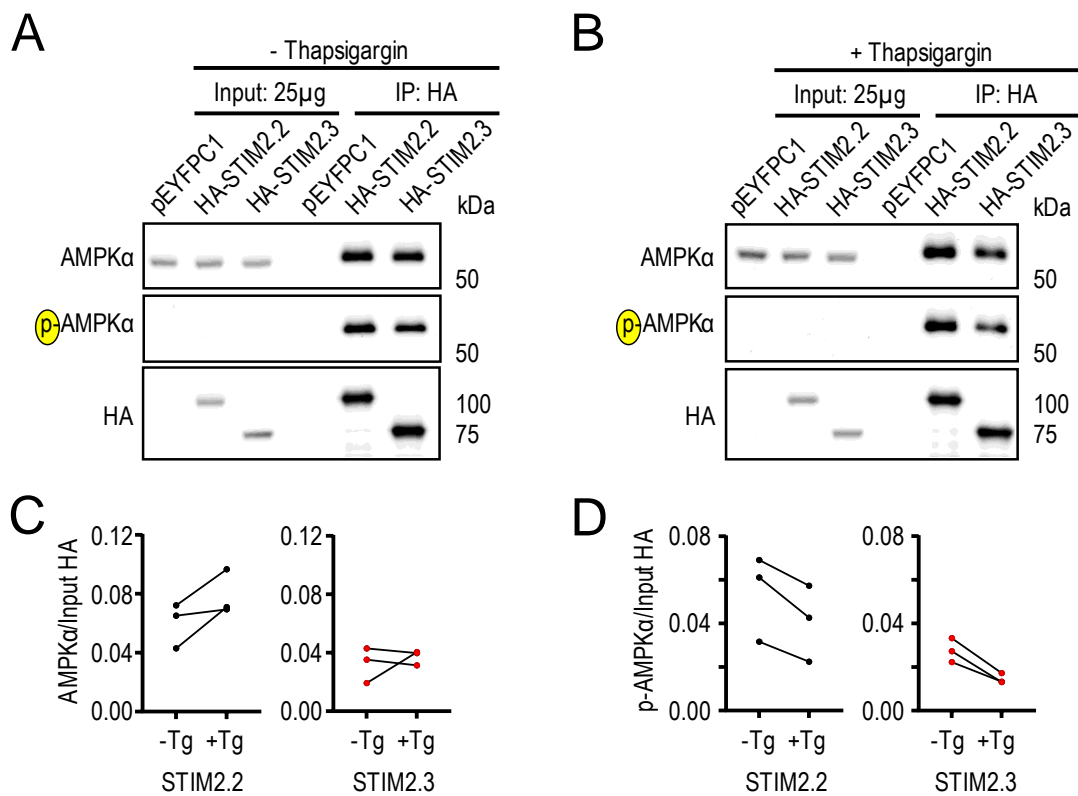
Figure 29 STIM2.3 shows reduced interaction with and activation of AMPKα. A-B: Co-immunoprecipitation using anti-HA agarose of HEK STIM1/STIM2$^{-/-}$ transfected with HA-STIM2.2 or HA-STIM2.3 before (A) and after (B) stimulation with Tg followed by Western Blot and incubation with the indicated antibodies. **C**: Quantification of precipitated total AMPKα before and after treatment with Tg of cells expressing STIM2.2 (left) or STIM2.3 (right). **D**: Quantification of precipitated phosphorylated AMPKα before and after treatment with Tg of cells expressing STIM2.2 (left) or STIM2.3 (right) expression. Co-IP from 3 independent transfections.

4.5.4 Generation of STIM2.2 and STIM2.3 stable cell lines

The generation of cell lines stably expressing STIM2.2 or STIM2.3 should provide further information about potential physiological functions of the novel STIM2 splice variant. As described in the first part, STIM2.3 is dominantly expressed in human brain, thus, the neuroblastoma cell line SH-SY5Y offers almost physiological conditions. To generate stable cell lines, SH-SY5Y STIM2$^{-/-}$ were transfected with HA-STIM2.2 or HA-STIM2.3. Selection of transfected cells was performed using G418 and clonal cell lines were generated. Western Blot identified for each condition only one clone stably expressing STIM2.2 (G11.1) or STIM2.3 (E12.1). Using an anti-HA antibody, HA-STIM2.3 was detected at the correct molecular weight of ~75 kDa in clone E12.1, whereas HA-STIM2.2 was only detected in clone G11.1 using a STIM2 antibody specific for full-length STIM2 (Fig. 30A). All other analyzed clones as well as SH-SY5Y STIM2$^{-/-}$ did not show any STIM2 band with neither antibody. Stable expression in the identified clones was further validated using Ca^{2+} imaging. To exclude the inhibitory effect of G418 on STIM2
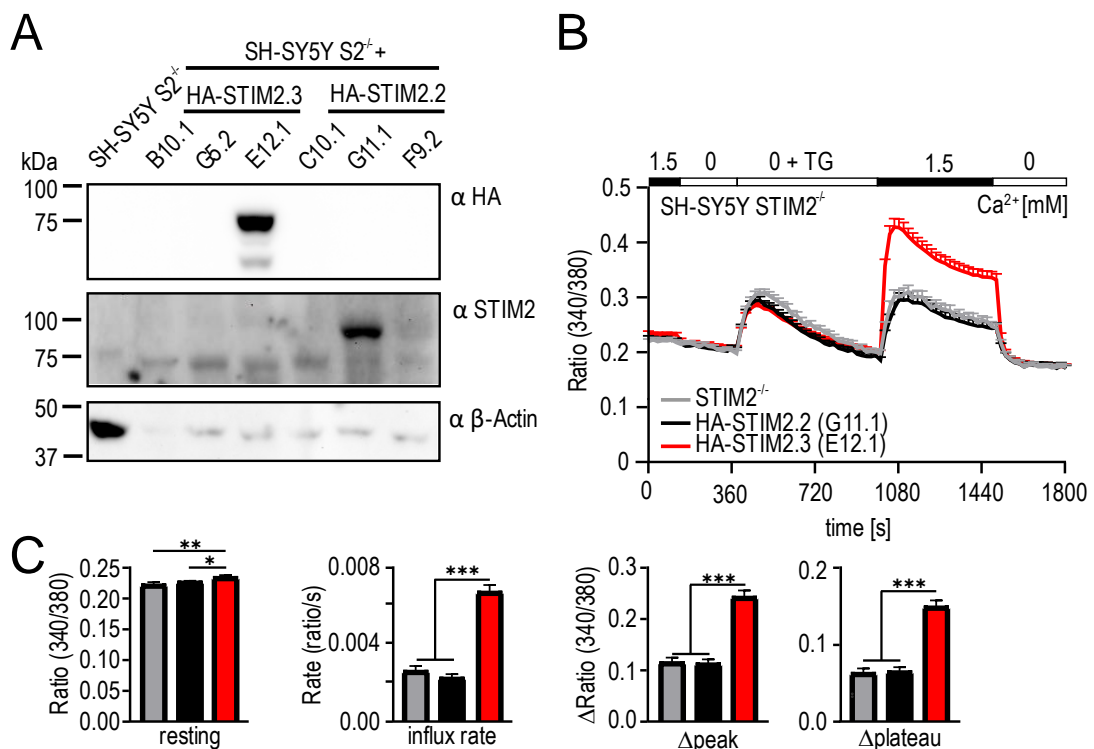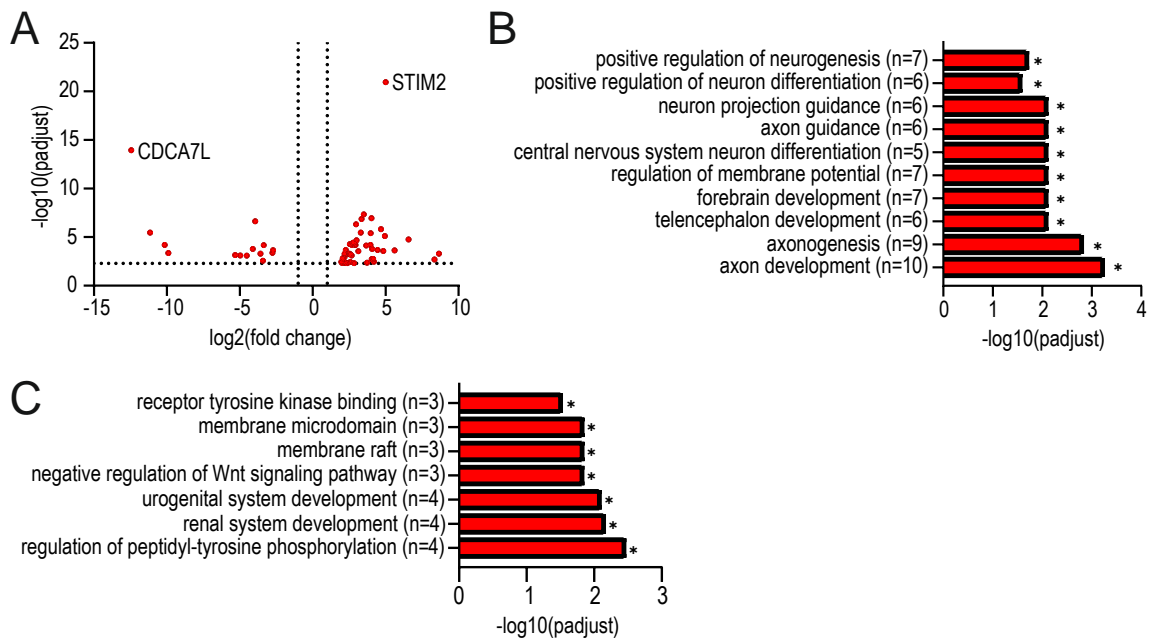

Figure 30 Generation of SH-SY5Y STIM2$^{-/-}$ stably expressing HA-STIM2.2 or HA-STIM2.3. A: Western Blot of different clonal SH-SY5Y STIM2$^{-/-}$ cell lines expressing HA-STIM2.3 or HA-STIM2.2. Membrane was incubated with the indicated antibodies. **B**: Average traces of changes in intracellular Ca^{2+} (Ratio 340/380) over time in response to perfusion with different external Ca^{2+} [mM] as indicated in the upper bar in SH-SY5Y STIM2$^{-/-}$ (grey, n=31) and HA-STIM2.2 (G11.1, black, n=44) or HA-STIM2.3 (E12.1, red, n=93) expressing clonal SH-SY5Y STIM2$^{-/-}$ cell lines. **C**: Quantification of changes in resting Ca^{2+}, influx rate, Δpeak and Δplateau measured in B. *** $p<0.001$, ** $p< 0.01$, * $p< 0.05$; Kruskal-Wallis ANOVA.

function, the stable cell lines were cultured without the selection antibiotic for three weeks. The STIM2.3 stable clone E12.1 showed increased resting Ca^{2+} levels and SOCE with significantly increased influx rate, Δpeak and Δplateau compared to SH-SY5Y STIM2$^{-/-}$ cells confirming expression of HA-STIM2.3 (Fig. 30B,C). The increase in SOCE resembles that of transient expression of STIM2.3 in SH-SY5Y STIM2$^{-/-}$ cells as shown in Fig. 30A and B. In contrast, the STIM2.2 stable clone G11.1 did not alter resting Ca^{2+} or SOCE suggesting that stable expression could differentially regulate STIM2 function to compensate the constantly increased Ca^{2+} influx compared to a transient expression (Fig. 30B,C). As shown in Fig. 13A and B, transient expression of STIM2.2 in SH-SY5Y STIM2$^{-/-}$ cells slightly increased SOCE, which was not observed in stable transfected cells. The integration of the plasmid DNA coding HA-STIM2.2 or HA-STIM2.3 into the genome was confirmed on genomic DNA level using primers amplifying the HA-tagged N terminus and the specific C terminus for each clone (data not shown).

4.5.5 GO analysis identified several neuronal processes regulated by STIM2.3

The identification of differentially expressed genes (DEGs) and associated processes should provide first information about the physiological role of the neuronal splice variant STIM2.3. As the stable expression of STIM2.2 in SH-SY5Y STIM2$^{-/-}$ cells could not be clearly demonstrated, further expression analysis using RNA sequencing was only performed in the clone E12.1 stably expressing STIM2.3. Since the stable cell line expresses both, the STIM2 variant and STIM1, SH-SY5Y WT cells were used as the control condition for identification of differentially expressed genes. RNA Seq analysis identified 64 DEGs for E12.1 compared to WT. While STIM2 is the most significantly upregulated gene as expected for an STIM2 over-expressing cell line, CDCA7L is the most significantly downregulated gene, which positively regulates cell population proliferation (Fig. 31A). Further Gene Ontology (GO) analysis was performed to associate the identified DEGs with biological processes, molecular functions, or cellular components, revealing that STIM2.3 expression positively regulates a variety of neuronal processes. Axon development and axonogenesis are the most significantly up-regulated processes with 9 and 10 genes of the identified DEGs being involved, respectively (Fig. 31B). Some prominent genes regulating neuronal processes are *MAP6*

KCNQ3, *GABRB3* and *NRCAM* (Table A1). GO analysis of the downregulated DEGs showed that expression of STIM2.3 negatively affects development of the urogenital and renal system with 4 of the identified DEGs being involved such as *ROBO2*, *TBX18* and *IGF2* (Table A2). Three of the downregulated DEGs are involved in membrane raft and microdomain and receptor tyrosine kinase binding (Fig. 31C). The genes involved in these processes are *ANGPT1*, *LRP4* and *CNTN1* (Table A2). In conclusion, STIM2.3 positively regulates neuronal development and differentiation indicating that STIM2.3 might play a role in synaptic transmission.


Figure 31 RNA Seq analysis of SH-SY5Y STIM2$^{-/-}$ stably expressing HA-STIM2.3. A: Identified differential expressed genes in SH-SY5Y STIM2$^{-/-}$ E12.1 using RNA Seq. The y-axis indicates signficance and the x-axis indicates up- or downregulation as log2(fold change) compared to SH-SY5Y WT. **B-C**: Selected up- (B) and downregulated (C) Gene Ontology terms including biological processes, molecular functions or cellular components, which are associated with the identified DEGs in A.

To validate the obtained GO results of the STIM2.3 stable cell line, RNA Seq and subsequent GO analysis was also performed for the single knockout cell lines SH-SY5Y STIM1$^{-/-}$ and SH-SY5Y STIM2$^{-/-}$. While deletion of STIM2 negatively affected axonogenesis, axon development and synapse assembly (Fig. 32A), the processes embryonic morphogenesis, voltage-gated ion channel activity and heart development were upregulated (Fig. 32B). Although some processes such as axonogenesis, neuron projection guidance, axon guidance and axon development were identified for both, deletion of STIM2 and STIM2.3 overexpression, the associated genes were different (Table A1, Table A3). Although the SH-SY5Y WT cell line, which expresses both STIM1 and STIM2.2, functioned as the control, validation of the specificity of STIM2.3-

expression on the identified neuronal processes requires analysis of a STIM2.2-stable cell line to exclude overexpression artefacts. In contrast, cell substrate adhesion, extracellular matrix and cluster of actin-based cell projections were downregulated in cells only lacking endogenous STIM1, while the processes growth cone, unfolded protein binding and axon part were upregulated (Fig. 32C,D; Table A5; Table A6). Strikingly, deletion of STIM1 did not identify the same GO terms as STIM2 deletion or STIM2.3-expression indicating that axonal development might be mainly regulated by STIM2.
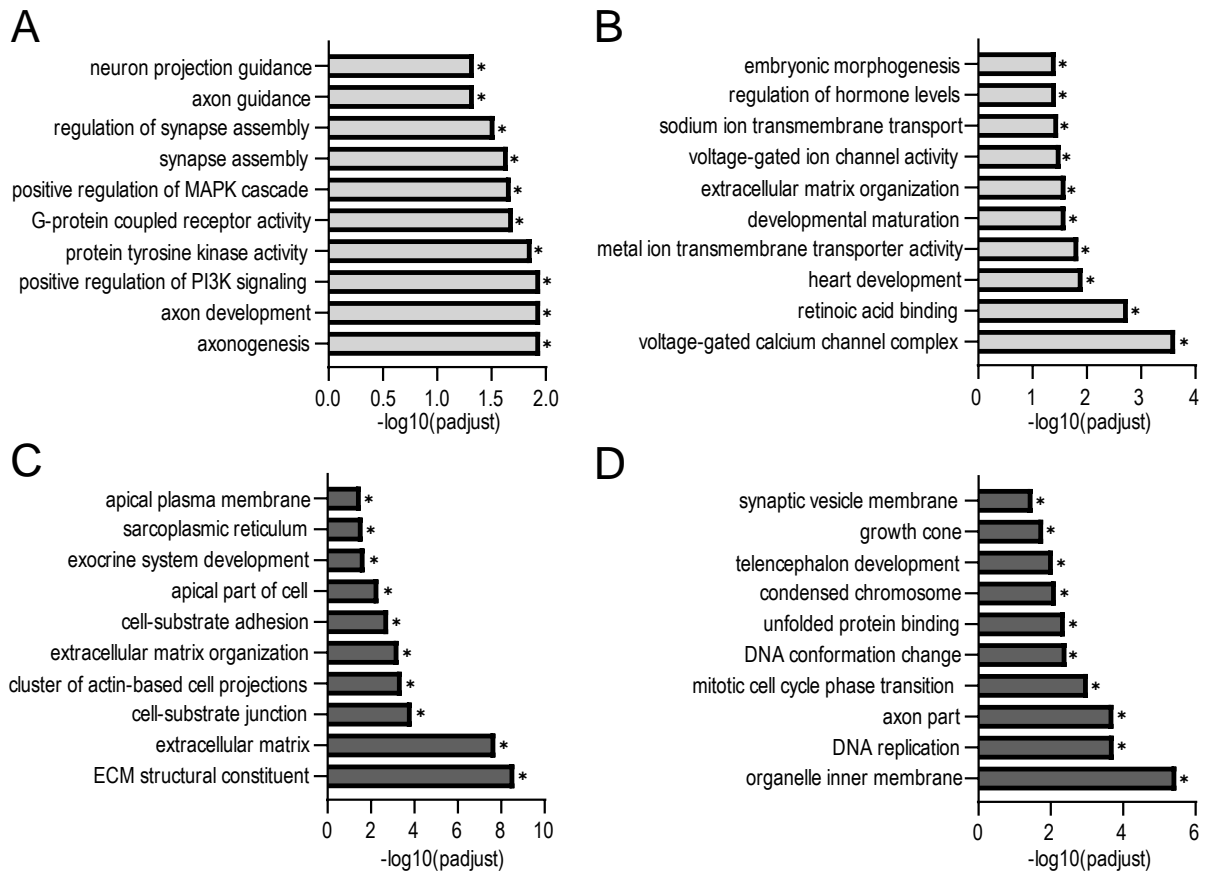

Figure 32 GO analysis of SH-SY5Y STIM1-/- and SH-SY5Y STIM2-/-. A/C: Selected downregulated Gene Ontology terms of SH-SY5Y STIM2-/- (A) and STIM1-/- (C) cells. **B/C:** Selected upregulated GO terms of SH-SY5 STIM2-/-(B) and STIM1-/- (D).

4.6 Characterization of STIM1 splice variants

During this work, additional experiments were performed for the STIM1 variants STIM1A and STIM1B to complete recent publications by Ramesh et al. (2021) and Knapp et al. (2022). In STIM1A, the in frame insertion of a 31 amino acid domain directly after the inhibitory domain results in an extended C terminus while all subsequent domains are preserved [Knapp et al. 2022]. In contrast, splicing of the short exon B results in a truncated STIM1 protein lacking the C-terminal S_n/P_n rich region and the PBD similar to splicing of STIM2.3 [Ramesh et al. 2021]. Both STIM1A and STIM1B lead to a reduced SOCE in a partially residue-dependent manner [Ramesh et al. 2021; Knapp et al. 2022].

4.6.1 The PBD is required for STIM1- and STIM1A-mediated NFAT activation

The scaffolding protein AKAP79 tethers a signalosome complex comprised of calcineurin, calmodulin, NFAT, PKA and phosphodiesterase 4 (PDE4) to ORAI1 following store depletion, ensuring tight regulation of NFAT activation [Kar, Barak, et al. 2021; Kar, Lin, et al. 2021]. While cAMP-activated PKA phosphorylates NFAT keeping it in an inactive state, calcineurin dephosphorylates NFAT in a Ca^{2+}-dependent manner allowing its translocation into the nucleus. In this signalosome complex, PDE4 leads to cAMP degradation, thereby ensuring spatially limited cAMP signaling and PKA activation in the close vicinity of activated ORAI1 [Kar, Barak, et al. 2021]. In addition, the PBD in STIM1 is required for the assembly of this signalosome complex as shown by Son et al. (2020). Recently, Knapp et al. (2022) identified the isoform PDE8B as a differential interaction partner of STIM1A, suggesting that PDE8B might be involved in the cAMP-regulated NFAT activation. STIM1A led to an enhanced Tg-induced NFAT translocation in SH-SY5Y STIM1$^{-/-}$ cells despite reducing SOCE. To examine NFAT activation under more physiological conditions, SH-SY5Y STIM1$^{-/-}$ cells expressing STIM1-mCherry or STIM1A-mCherry were stimulated with 100 μM carbachol (Cch) to activate the IP_3 signaling pathway through stimulation of muscarinic receptors. Despite a slightly altered global Ca^{2+} entry compared to stimulation with Thapsigargin, carbachol more efficiently depleted the stores leading to enhanced STIM1- and STIM1A-mediated NFAT translocation (Fig. 33). However, Cch-induced NFAT translocation was reduced in STIM1A-expressing compared to STIM1-expressing cells (Fig. 33C).
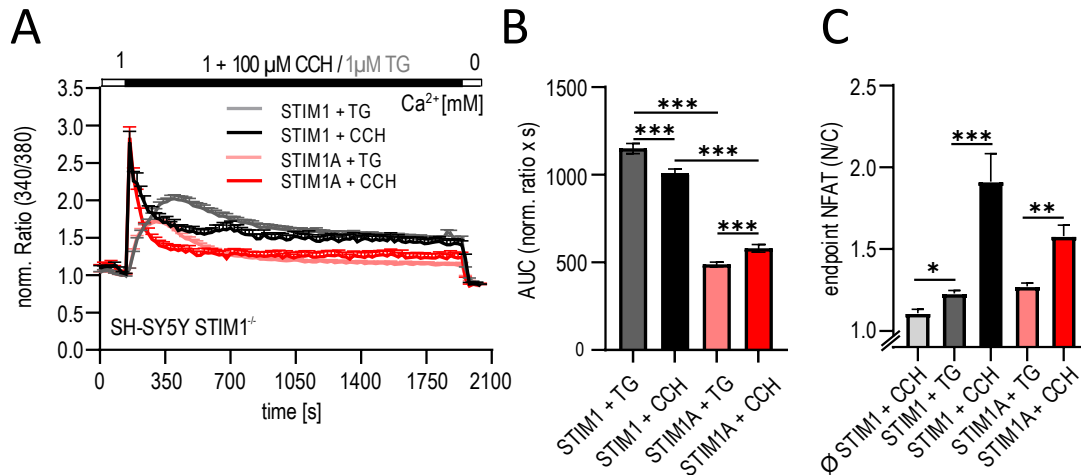
Figure 33 Stimulation with carbachol enhances NFAT translocation. A: Normalized average traces of intracellular Ca²⁺ (Ratio 340/380) over time in response to perfusion with different external Ca²⁺ [mM] as indicated in the upper bar of SH-SY5Y STIM1⁻/⁻ cells transfected with STIM1-mCherry (black, n=27; grey, n=105) or STIM1A-mCherry (red, n=26; light red, n=75). Darker colors indicate stimulation with carbachol (CCH) **B:** Quantification of area under the curve (AUC) measured in A. **C:** Quantification of NFAT1 translocation into the nucleus (NFAT1-GFP N/C). For each condition 13-20 cells were analyzed from 3 independent transfections. *** p< 0.001, * p< 0.05; Kruskal-Wallis ANOVA. [Knapp et al., 2022]

While inhibition of PDE8B using the inhibitor PF-04957325 (PF) [Vang et al. 2016] had a stronger effect on STIM1-mediated NFAT activation without altering global cytosolic Ca²⁺ levels, application of cAMP analogs specifically activating the PKA or Epac pathway triggered a similar increase in Tg-induced NFAT translocation for both STIM1 and STIM1A. These results indicate a higher PDE8B activity in STIM1-expressing cells. However, saturating the cells with cAMP eliminated the observed differences between the STIM1 variants [Knapp et al. 2022]. To investigate whether deletion of the PBD in both STIM1 and STIM1A would obliterate the effect of PDE8B inhibition, mutants were generated lacking the last 13 amino acids (i.e. PBD, ΔKK) (Fig. 34A). SH-SY5Y STIM1⁻/⁻ cells were co-transfected with NFAT1-GFP and STIM1-mCherry, STIM1ΔKK-mCherry, STIM1A-mCherry or STIM1AΔKK-mCherry and preincubated with PF-04957325 for 2 hours using 1 µM to inhibit PDE8B. The inhibitor was kept in all solutions during the measurement. While deletion of the PBD reduced global Ca²⁺ entry with STIM1, it did not reduce STIM1A-mediated Ca²⁺ influx (Fig. 34B,C). However, NFAT translocation was completely abolished with STIM1 variants lacking the PBD despite the presence of endogenous STIM2. Moreover, inhibition of PDE8B using the inhibitor PF-04957325 did not increase NFAT translocation with STIM1 variants lacking the PBD in contrast to full-length proteins (Fig. 34D).
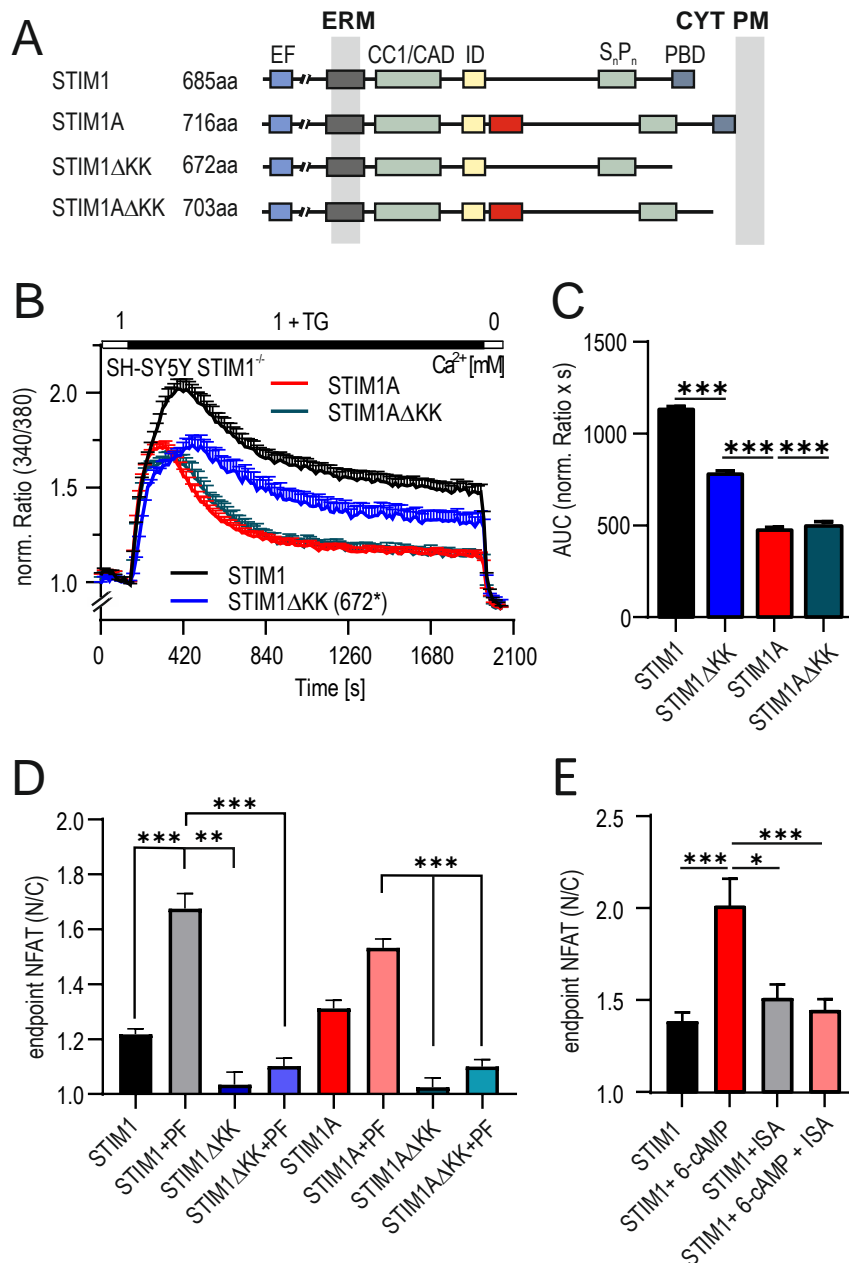
Figure 34 Deletion of the PBD in STIM1 abolished NFAT translocation. **A:** Schematic protein structure of full-length STIM1 and STIM1A and deletion of the PBD (ΔKK). **B:** Traces showing average changes (mean + SEM) in intracellular Ca^{2+} (Ratio 340/380) over time in response to perfusion of different external Ca^{2+} [mM] as indicated in the upper bar in SH-SY5Y STIM1^{-/-} cells transfected with mCherry-tagged constructs as indicated (n = 46–105). **C:** Quantification of area under the curve (AUC, mean + SD) measured in A with STIM1 (n = 105), STIM1ΔKK (n = 56), STIM1A (n = 75), and STIM1AΔKK (n = 46). *** p< 0.001, Kruskal–Wallis ANOVA with Dunn's multiple comparisons test. **D:** Normalized endpoint NFAT translocation (mean + SEM) of control constructs (STIM1, STIM1A; n=56-120) and STIM variants with deleted PBD (ΔKK, n=18-19) with or without addition of 1 μM PF-04957325, ** p< 0.01 and *** p< 0.001, Kruskal–Wallis ANOVA with Dunn's multiple comparisons test. For clarity, not all differences are shown. **E:** Normalized endpoint NFAT translocation (mean + SEM) of cells transfected with indicated constructs that were treated ON with 1 μM ISA with or without addition of 1 μM 6-Bnz-cAMP 30 min before measurement. * p< 0.05, ** p< 0.01, and *** p< 0.001, Kruskal–Wallis ANOVA, n = 26-50 from 3 independent transfections. [Knapp et al., 2022]

These results suggest, that increased cAMP levels could lead to elevated PIP2 levels in the plasma membrane and thereby facilitate assembly of the signalosome complex by attachment of STIM at the PM. Indeed, in *S. cerevisiae*, cAMP regulates the generation of PIP2 by the phosphatidylinositol-4-phosphate 5-kinase (PIP5K) [Kato et al. 1989]. To test this hypothesis, SH-SY5Y STIM1$^{-/-}$ cells expressing NFAT1-GFP and STIM1-mCherry were preincubated with the PIP5K inhibitor ISA-2011B [Kunkl et al. 2017] over night using 1 µM. The cAMP analog (6-Bnz-cAMP) was preincubated for 30 min at and all substances were kept in all solutions during the measurement. Indeed, inhibition of PIP5K obliterated the increased cAMP-mediated NFAT translocation, whereas it did not affect only STIM1-mediated NFAT activation (Fig. 34E). These results identify a hitherto unknown cAMP-dependent target in the regulation of NFAT activation independent of the PKA and calcineurin signaling pathway.

4.6.2 Neither STIM1 nor STIM1B significantly alter K$^+$ induced Ca^{2+} entry

Several studies report a negative feedback mechanism coupling ER filling and STIM1 activation to inhibition of the voltage-gated L-type Ca^{2+} channel Ca$_v$1.2, thereby regulating neurotransmission [Park et al. 2010; Youjun Wang et al. 2010; Dittmer et al. 2017]. Given the neuronal expression of the C-terminally truncated STIM1B (Fig. 35A)
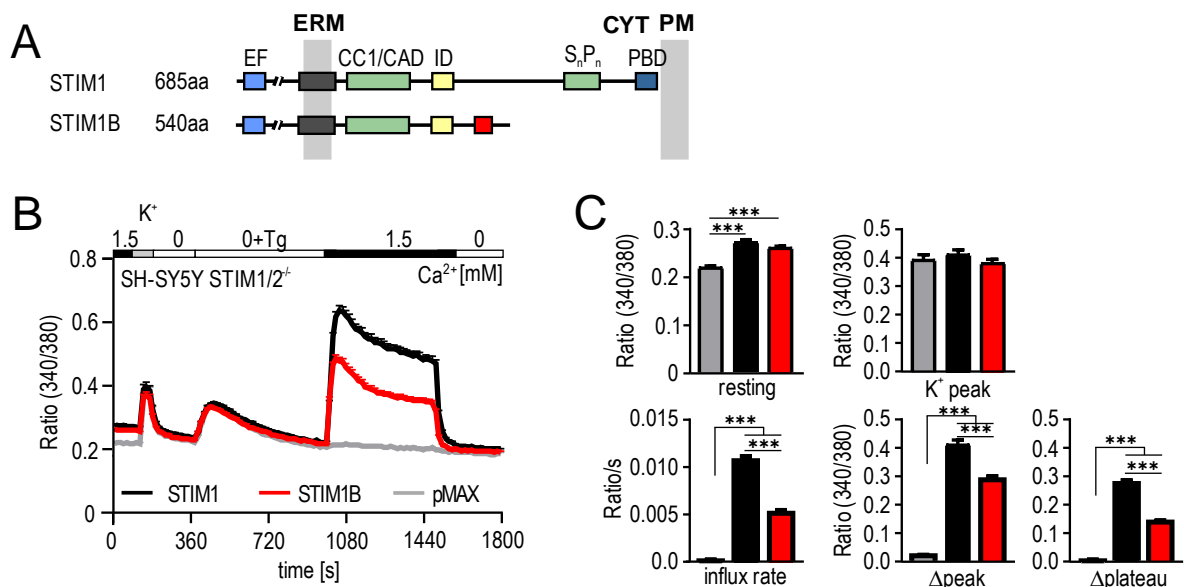
Figure 35 STIM1 and STIM1B rescue SOCE in SH-SY5Y STIM1/2$^{-/-}$ cells. A: Schematic protein structure of STIM1 and STIM1B with functional domains. Domain B is indicated in red. **B:** Average traces of intracellular Ca^{2+} (Ratio 340/380) over time in response to perfusion with different external Ca^{2+} [mM] as indicated in the upper bar of SH-SY5Y STIM1$^{-/-}$ cells transfected with YFP-STIM1 (black, n=27), YFP-STIM1B (red, n=26) or empty vector (grey, n=). **C:** Quantification of resting Ca^{2+}, K$^+$ peak, influx rate, Δpeak and Δplateau measured in B. *** p< 0.005, Kruskal-Wallis-ANOVA.

[Ramesh et al. 2021], SH-SY5Y STIM1/2$^{-/-}$ cells, which endogenously express functional VGCC [Sousa et al. 2013], were transfected with YFP-STIM1, YFP-STIM1B or empty vector. After baseline recording, a short depolarization stimulus using a high K$^+$ solution was followed by the Ca^{2+} readdition protocol. Strikingly, both STIM1 and STIM1B increased resting Ca^{2+}, whereas K$^+$ induced peak was not significantly altered compared to control transfected cells (Fig. 35C). SH-SY5Y STIM1/2$^{-/-}$ cells did not show Tg-induced Ca^{2+} influx with mock transfection, whereas re-expression of STIM1 rescued SOCE (Fig. 35B). However, expression of STIM1B only partially restored Ca^{2+} influx with significantly decreased influx rate, Δpeak and Δplateau compared to STIM1 (Fig. 35C).

5 Discussion

SOCE constitutes the main Ca^{2+} influx pathway for immune cell function with STIM proteins as the ER resident Ca^{2+} sensors initiating SOCE and ORAI proteins forming the Ca^{2+} selective channel in the plasma membrane. However, STIM proteins are involved in a variety of Ca^{2+} dependent processes besides the canonical SOCE pathway, which also exists to different extents in every other cell. The characterization of several recently described STIM variants demonstrate that alternative splicing is a potent tool to adjust protein function and to adapt Ca^{2+} signaling to individual cellular needs [Darbellay et al. 2011; Miederer et al. 2015; Ramesh et al. 2021; Knapp et al. 2022].

5.1 Evolution of the splice variant STIM2.3

The aim of this work was the functional characterization of the novel STIM2 splice variant STIM2.3, in which splice insertion of a short exon results in a truncated protein lacking the C-terminal S_n/P_n region and the PBD. In contrast to the hitherto characterized STIM1 and STIM2 variants, which can be detected in several tissues among different species including fish, mice and human, previous data revealed expression of STIM2.3 in human brain but not in any murine or further human tissues [Miederer et al. 2015; Gilson 2016]. Searching for the specific amino acid sequence using BLAST further restricted existence of STIM2.3 to old world monkeys, which includes homo sapiens (Fig. 9B, C), suggesting an advantage of STIM2.3 with the increasing tissue complexity. Using cDNA derived from different postmortem human brain regions of several donors, STIM2.3 showed the highest expression in cerebellum, whereas total STIM2 displayed similar expression levels among the analyzed regions (Fig. 10B). During evolution, the expansion rates of the neocortex and cerebellum are correlated. However, the cerebellar expansion rate significantly increased relative to neocortical expansion in the phylogenetic branch of apes compared to related non-ape branches. This cerebellar specialization indicates an important role of the cerebellum in human cognitive evolution including technical complexity such as production and use of tools, language and learning of complex motor skills [Barton and Venditti 2014]. These findings indicate a role of STIM2.3 in the cognitive evolution of complex motor behavior.

In human cerebellum, STIM1 and ORAI2 are the predominant homologues (Fig. 10A) indicating that STIM2.3 most likely affects STIM1/ORAI2-mediated SOCE. However, the samples overall have a high variability due to different postmortem and sample preparation times affecting RNA integrity. Furthermore, the efficiency of the splice specific primers has not been tested, hence, these results cannot be directly correlated to total STIM2 expression. In addition, more studies are required to unravel the mechanism of STIM2.3 splicing. It remains to be investigated how splicing of STIM2.3 is regulated either by different splice factors or in an age- or gender-related manner, since the qPCR data indicate higher STIM2.3 expression in female donors. Due to the lack of further brain samples, it is still unclear whether STIM2.3 is associated with human neurodegenerative diseases such as Alzheimer's or Parkinson's disease. Downregulation of STIM2 and the resulting impaired nSOC is responsible for CaMKII-dependent loss of synaptic spines in familial AD models and during amyloid synaptotoxicity [Sun et al. 2014; Popugaeva et al. 2015]. A recent study analyzing mis-splicing in Huntington's disease (HD) identified *STIM2* as being affected with the genomic boundaries of the mis-spliced exon corresponding to *STIM2.3* (genome.ucsc.edu). Splicing of *STIM2.3* is down-regulated in the striatum of HD patients compared to age-matched control donors [Elorza et al. 2021]. These results imply that splicing of STIM2.3 may be cell type specific, and mis-splicing may be associated with neurodegenerative diseases.

5.2 Functional characterization

STIM2.3 is a gain-of-function variant

After identifying STIM2.3 as a naturally expressed STIM2 splice variant, overexpression of STIM2.3 in the two distinct cell lines HEK and SH-SY5Y demonstrated that STIM2.3 is capable to activate ORAI following full store depletion independent of endogenous STIM proteins (Fig. 12). Moreover, STIM2.3 even increased Tg-induced Ca^{2+} influx in both cell lines compared to wildtype STIM2.2 (Fig. 12, Fig.13). These results validate the power of alternative splicing to increase protein diversity. In addition to STIM1L, STIM2.3 is the second naturally occurring gain-of-function splice variant, while the other STIM variants reduce Ca^{2+} influx. The eight-residue insertion in STIM2.1 interferes with ORAI1 coupling responsible for the abolished SOCE [Miederer et al. 2015; Rana et al. 2015], whereas the specific domain in STIM1A directly after the ID might interfere with channel gating by disabling a stabilized interaction between STIM1 and the ETON region

of ORAI1 [Knapp et al. 2022]. Interaction analysis using BiFC revealed no difference in the interaction of STIM2.2 and STIM2.3 with ORAI1 but significantly enhanced coupling of STIM2.3 to ORAI2 (Fig. 15B). However, enhanced interaction with ORAI2 does not solely explain the increased SOCE phenotype as both, expression of STIM2.3 in HEK STIM1/2$^{-/-}$ cells dominantly expressing ORAI1 or in SH-SY5Y STIM1/2$^{-/-}$ cells dominantly expressing ORAI2, increased SOCE (Fig. 15A). Nonetheless, these results support a physiological relevance of STIM2.3 in the human brain where ORAI2 is the dominant isoform. STIM1L more efficiently activates TRPC1 responsible for the increased SOCE, while STIM1L-induced I$_{CRAC}$ was reduced compared to STIM1 [Dyrda et al. 2020]. Recently, Shalygin et al. (2021) demonstrated that store depletion-induced Ca^{2+} influx trough ORAI triggered TRPC1 activation, while subsequent STIM2-mediated TRPC1 activity was independent of Ca^{2+} influx. Consequently, the increased SOCE phenotype observed with STIM2.3 could potentially be mediated by additional activation of TRPC1. However, further patch clamp experiments are required to assess the contribution of TRPC-induced Ca^{2+} influx to STIM2.3-mediated SOCE. In contrast to Z. Li et al. (2007) demonstrating that deletion of the S$_n$/P$_n$ region and the PBD in STIM1 reduced SOCE, the comparable deletion in STIM2.3 neither abolished ORAI activation nor reduced SOCE. Furthermore, the absent proposed calmodulin binding site at the PBD, which is responsible for Ca^{2+} dependent SOCE inactivation [Bauer et al. 2008], could theoretically prolong STIM2.3-mediated Ca^{2+} influx due to enhanced cluster stability. Despite increasing STIM1- and STIM2-mediated Ca^{2+} influx, the impact of the novel STIM2 splice variant on SOCE under physiological conditions would be dependent on the endogenous expression levels of the SOCE components. STIM and ORAI are expressed in various tissues with cell type specific ratios fine-tuning intracellular Ca^{2+} signals [reviewed in Prakriya and Lewis 2015]. Thus, STIM2.3 expression could vary during distinct developmental or differentiation processes. The availability of primary human brain samples, especially of younger individuals, is very limited and the utilization requires ethical permission. Publicly available RNA Seq data of different human brain samples could help to investigate STIM2.3 splicing during different developmental stages. While heterologous expression of the STIM variants is similar in Ca^{2+} imaging experiments, endogenous levels of STIM2.3 are likely much lower suggesting a potential additional role outside the canonical SOCE pathway. One of these roles could include competing away C-terminal binding partners from the SOCE complex.

Like STIM2.2, STIM2.3 seems to be a regulator of basal Ca^{2+} concentration. However, the results were not consistent between different experiments. Regulation of resting $[Ca^{2+}]$ by STIM2.3 is likely dependent on the dominant ORAI homologue. In HEK cells, ORAI1 is the most abundant isoform exhibiting a higher conductance compared to ORAI2 [Lis et al. 2007], which is the dominant isoform in SH-SY5Y cells. Thus, expression of STIM2.3 in HEK STIM1/2$^{-/-}$ increased resting Ca^{2+} similar to STIM2.2 (Fig. 12B, Fig. 16C), while STIM2.3-mediated resting Ca^{2+} levels were significantly reduced compared to STIM2.2 in SH-SY5Y STIM1/STIM2$^{-/-}$ cells despite significantly increased interaction with ORAI2 (Fig. 15B, Fig. 17C, Fig. 18C). Furthermore, the presence of STIM1 affects basal Ca^{2+} levels. Over-expression of STIM1 and STIM2.3 in a 1:1 ratio [Poth 2018] and the presence of endogenous STIM1 in SH-SY5Y STIM2$^{-/-}$ cells significantly increased resting Ca^{2+} compared to STIM2.2 (Fig. 13B) indicating that the novel STIM2 variant also recruits STIM1 to ER PM junctions and facilitates ORAI activation under conditions with only mild fluctuations in luminal Ca^{2+} concentration [Subedi et al. 2018]. However, the different resting Ca^{2+} indicate that STIM2.3 likely requires stronger store depletion to activate ORAI. In addition, the PBD facilitates SOCE activation by stabilizing the STIM2/ORAI complexes and promoting subsequent Ca^{2+} influx under resting conditions [S. Zheng et al. 2018], supporting a reduced sensitivity of the C-terminal truncated STIM2.3 to mild store depletion. To confirm this hypothesis, different Thapsigargin concentrations ranging from $10\,nM$ to $1\,mM$ could be used to determine activity of STIM2.3 under conditions with only partial store depletion.

Gain-of-function mutations in STIM1 result in pathological Ca^{2+} signals associated with tubular aggregate myopathy and Stormorken syndrome [Böhm et al. 2017]. Whether the increased STIM2.3-mediated SOCE is involved in physiological or pathophysiological processes remains to be investigated.

STIM2.3-specific SOCE phenotype is independent of specific spliced-in residues

In the hitherto characterized STIM1 variants (STIM1L, STIM1B and STIM1A) the observed SOCE phenotype is mediated by their specific domain. While an actin-binding site enables STIM1L to form permanent cluster with ORAI1 leading to faster SOCE activation [Darbellay et al. 2011], specific residues have been identified to be at least partially responsible for the STIM1A- and STIM1B-mediated SOCE phenotype [Ramesh et al. 2021; Knapp et al. 2022]. In contrast, a larger deletion terminating STIM2.2 at the

last common amino acid 674 (STIM2.2Δ674) reproduced the enhanced STIM2.3-mediated SOCE phenotype, thereby the phenotype is likely independent of the specific amino acids. On the other hand, deletion of only the PBD in STIM2 significantly reduced Ca^{2+} influx (Fig. 16). Ong et al. (2015) and Subedi et al. (2018) already reported that deletion of only the PBD prevented Tg-induced cluster formation and interaction with ORAI1 resulting in drastically reduced Ca^{2+} influx. These findings demonstrate that for full-length STIM2 the PBD is required for C-terminal unfolding and attachment to the PM. Hence, deletion of the PBD stabilizes the inactive state, preventing exposure of the CAD. However, simultaneous ORAI1 over-expression may rescue the negative effect of STIM2.2Δ5K as reported by Son et al. (2020), demonstrating that store depletion-induced coupling of STIM1 to ORAI1 seems to be sufficient to trigger C-terminal unfolding despite deletion of the PBD. Interestingly, in STIM2.3 the lack of the PBD did not hinder C-terminal unfolding and subsequent ORAI activation. Conformational change of the truncated C terminus in STIM2.3 following store depletion is likely facilitated suggesting an additional binding partner or intramolecular interaction negatively regulating STIM2.2 function. Compared to STIM1, containing one single microtubular binding protein (MBP) attachment site, STIM2 contains two MBP (here EB) binding motifs within its C terminus, which are absent in STIM2.3. In STIM1, microtubular tracking competes with binding of the PBD to the PM reducing STIM1-mediated SOCE [Chang et al. 2018]. Mutation of only one binding motif as described in Pchitskaya et al. (2017) reduced STIM2-mediated SOCE in SH-SY5Y STIM1/STIM2^{-/-} indicating enhanced EB3 binding, whereas the simultaneous mutation of both binding sites did not significantly affect Tg-induced Ca^{2+} influx in our hands (Fig. 17). Due to the spatial vicinity of both EB binding motifs, which are only separated by 31 amino acids, EB binding and thus also microtubular tracking could be sterically prevented if MBP bind to one site. In conclusion, these findings suggest that STIM2 may not constantly track along the microtubular network in contrast to STIM1, displaying comet like structures under resting conditions [Ahmand et al. 2022]. However, simultaneous mutation of both EB binding sites in STIM2.2 2xIP+Δ5K rescued the negative effect of STIM2.2Δ5K on SOCE (Fig. 18), demonstrating competitive functions between the PBD and EB binding motifs similar to previous findings in STIM1 [Chang et al. 2018]. However, PM tethering in STIM2 is the stronger stimulus compared to microtubular tracking. Neither mutation reproduced the STIM2.3-gain-of-function SOCE phenotype. A

slightly shorter deletion in STIM2.2 compared to STIM2.3 deleting the amino acids 712 - 833 (STIM2.2Δ711) had no effect on SOCE (Fig. 20) indicating that the additional 37 amino acids compared to the mimicking mutant STIM2.2Δ674 may be involved in the STIM2.3-mediated SOCE phenotype. Surprisingly, internal deletion of these amino acids (Δ675-710), while maintaining the remaining C-terminal domains, decreased SOCE in combination with the PBD, whereas the simultaneous deletion of both neutralized this negative effect (Fig. 21). Neither internal deletion reproduced the increased phenotype of STIM2.3 but may have induced an artificial backfolding of the positively charged PBD onto the negatively charged inhibitory or poly-glutamate (E_5) domain potentially explaining the observed negative effect on SOCE. However, additional mutagenesis would be necessary to prove this hypothesis.

PBD mediates STIM2 clustering

In STIM2, the PBD functions as an ER retention signal (KKXK) but also mediates anchoring of STIM at the plasma membrane following activation [Ercan et al. 2012]. Despite the truncated C terminus lacking the PBD, STIM2.3 still displayed ER distribution in resting HEK STIM1/STIM2$^{-/-}$ cells and colocalized with STIM1 and STIM2.2 as quantified by the Mander's coefficients (Fig. 14A, C). Hence, the trans-membrane domain and additional C-terminal motifs (i.e. three RxR motifs) are sufficient to ensure ER localization, which was also the case for the mimicking mutant STIM2.2Δ674 and the mutant only lacking the PBD STIM2.2Δ5K. However, all STIM2 proteins lacking the PBD, i.e. STIM2.3, STIM2.2Δ674 and STIM2.2Δ5K, did not pre-cluster in contrast to STIM2.2 despite the identical sensitive EF hand. A chimera consisting of the STIM1 N terminus and the STIM2 C terminus displayed mobile clusters under ambient conditions, whereas the chimera comprised of the STIM2 N terminus and the STIM1 C terminus displayed comet-like microtubular tracking, characteristic for STIM1, despite the more sensitive EF hand [Ahmand et al. 2022]. In conclusion, these findings demonstrate that the sensitive EF hand may initiate STIM2 activation, but PM tethering is required for stabilization of puncta under resting conditions. To confirm this hypothesis, the experiment should be repeated using TIRF microscopy, which enables visualization of only the PM. Moreover, artificial addition of the PBD to STIM2.3 is likely to result in pre-clustering.

Following store depletion, STIM2.3 translocated into the same ER-PM junctional regions as STIM1 and STIM2.2 (Fig. 14B,D) and together with BiFC results (Fig. 15B) demonstrate that variants can form hetero-oligomers. Additionally, STIM2.3 did not alter cluster sizes of STIM1 and STIM2.2 (Fig. 14E), which does not explain the increased SOCE phenotype. To further analyze the impact of the PBD on cluster formation in the absence of endogenous STIM, time lapse recordings of the different STIM2 proteins were performed in HEK STIM1/STIM2$^{-/-}$ cells. As previously shown, deletion of the PBD abolished pre-clustering and additionally reduced Tg-induced cluster formation in STIM2.3, STIM2.2Δ5K and its rescuing mutant STIM2.2 2xIP+Δ5K despite their differential SOCE phenotype. In contrast, STIM2.2 was already pre-clustered and displayed prominent clustering upon store depletion (Fig. 19). These results confirm previous findings by S. Zheng et al. (2018) demonstrating that PM tethering is not crucial for ORAI gating but rather facilitates SOCE activation. Interestingly, both STIM2.3 and STIM2.2 2xIP+Δ5K displayed mobile clusters indicating that stable cluster formation requires PBD-mediated anchoring of STIM2 at the PM. However, ORAI over-expression can increase cluster sizes by stabilizing the STIM2 oligomers.

Regulation of STIM2 function

SOCE is a mechanism sensitive to oxidative stress. Exposure of ORAI1 and ORAI2 to extracellular reactive oxygen species causes thiol oxidation of C195 resulting in SOCE inhibition [Bogeski et al. 2010; Alansary et al. 2016]. While oxidation of the intraluminal C56 store-independently causes STIM1 oligomerization and subsequent SOCE activation [Hawkins et al. 2010], oxidoreductase ERp57-induced oxidation of C49 and C56 leads to the formation of a disulfide bridge interfering with STIM1 and SOCE activation [Prins et al. 2011]. In contrast to STIM1, STIM2 contains ten additional C-terminal cysteine residues suggesting higher redox sensitivity [Bhardwaj et al. 2016]. Xiao et al. (2020) identified in an in vivo redox proteomic screen several cysteine residues in STIM2 to be oxidized with C313 as the prominent residue in 9 out of 20 cases. This study is supported by the findings of Gibhardt et al. (2020) identifying C313 within STIM2 CAD as the critical residue responsible for the reduced SOCE under oxidative conditions. However, incubation with 1 mM H_2O_2 only significantly reduced influx rate in STIM2.2-expressing cells and Δplateau in STIM2.3-expressing cells. Moreover, external H_2O_2 did not affect STIM2.2Δ674-mediated SOCE (Fig. 22). The strong store depletion used in the

Ca^{2+} re-addition protocol likely counteracts the inhibitory effect of H$_2$O$_2$ on STIM2 function. In addition, deletion of the C-terminal residues might alter the reactiveness of C313. To confirm the negative effect of C313 oxidation on STIM2.3-mediated SOCE, the experiment should be repeated using a global protocol simultaneously triggering store depletion and Ca^{2+} influx. In STIM2, oxidation of the cytosolic cysteine C812 in direct vicinity to the PBD promotes oligomerization of a recombinant C-terminal fragment of STIM2, spanning the amino acids 325 – 833, and subsequent anchoring at the PM. However, whether oxidation of cytosolic cysteines facilitates STIM2 oligomerization and promotes enhanced Ca^{2+} influx under oxidative conditions, remains to be investigated [Bhardwaj et al. 2013]. Potentially, the oxidation of cytosolic cysteines is responsible for hypoxia-induced cell death in cultured neurons mediated by increased STIM2-mediated SOCE [Berna-Erro et al. 2009]. Due to its truncated C terminus lacking five cysteine residues compared to STIM2.2, STIM2.3 may be less sensitive to redox modifications exerting a protective role during oxidative stress in neurons.

5.3 Potential physiological function

Influence of STIM on voltage-gated Ca^{2+} entry

The neuroblastoma cell line SH-SY5Y expresses functional voltage-gated Ca^{2+} channels and their auxiliary subunits and offer certain advantages over primary neurons to study calcium homeostasis in neuronal cells. Sousa et al. (2013) showed that Ca$_v$2.2 (CACNA1B) and Ca$_v$3.1 (CACNA1G) are expressed VGCCs, whereas Ca$_v$1.2 (CACNA1C) was not detected. Our expression analysis confirmed expression of Ca$_v$2.2 and Ca$_v$3.1, however, Ca$_v$1.2 was also expressed in all analyzed cell lines. Interestingly, knockout of either STIM1, STIM2 or both homologues in SH-SY5Y cells increased the expression of Ca$_v$ channels compared to WT cells with Ca$_v$2.2 as the dominant isoform in the single knockout cell lines (Fig. 23A,B). Differences between RNA Seq and qRT-PCR data are likely due to different passage numbers. Furthermore, additional RNA Seq samples are required for SH-SY5Y STIM1$^{-/-}$ and STIM1/STIM2$^{-/-}$ to confirm the obtained results. Additionally, specific inhibitors could help to elucidate which Ca$_v$ channel mediates the K$^+$ induced Ca^{2+} influx and whether this result agrees with those of RNA Seq and qRT-PCR.

Deletion of STIM2 alone only slightly reduced SOCE, whereas knockout of STIM1 in SH-SY5Y STIM1$^{-/-}$ and STIM1/STIM2$^{-/-}$ cells completely abolished Tg-induced Ca^{2+} influx

indicating that in these cells SOCE is mainly mediated by STIM1. However, the neuroblastoma cell line is a heterogeneous population classified into three morphologically distinct phenotypes corresponding to N- (neuroblast-like), S- (substrate-adherent) and I- (intermediate) type [Ciccarone et al. 1989]. Although the initial SH-SY5Y cell line only consisted of N-type cells, Bell et al. (2013) demonstrated that both N- and S-types were isolated from cultured SH-SY5Y cells. In cell culture, both N- and S-type cells can switch their phenotype [Ciccarone et al. 1989] resulting in differential expression of ORAI1 and TRPC1. S-type cells display reduced SOCE compared to N-type cells [Bell et al. 2013]. Hence, it remains to be investigated whether knockout of only one STIM isoform promotes either one or the other phenotype.

Previous studies report a direct inhibitory effect of STIM1 on voltage-gated Ca^{2+} entry and internalization of the voltage-gated channel $Ca_v1.2$ [Park et al. 2010; Youjun Wang et al. 2010; Dittmer et al. 2017]. Indeed, deletion of STIM1 and STIM2 increased K^+ induced Ca^{2+} peak and the number of cells responding to the depolarization stimulus (% Responder) (Fig. 23B,D), supporting previous findings of a negative feedback mechanism between SOCE and VGCE. However, this negative regulation is not a STIM1-specific effect, since deletion of only STIM2 led to a similar increase in K^+-induced Ca^{2+} peak. Furthermore, the single knockout of only one STIM homologue results in the same phenotype as the double knockout indicating that Ca_v inhibition does not require Ca^{2+} influx through ORAI, which is absent in SH-SY5Y STIM1$^{-/-}$ and SH-SY5Y STIM1/STIM2$^{-/-}$ cells (Fig. 26A,C). In conclusion, our results indicate that Ca_v inhibition is a synergistic effect, which requires the presence of both STIM1 and STIM2.

Heterologous expression of all three STIM2 splice variants (i.e. STIM2.1, STIM2.2, STIM2.3) in SH-SY5Y STIM2$^{-/-}$ cells only slightly reduced K^+ peak and the number of responding cells (Fig. 24) and argues against acute interacting interference of STIM2 with Ca_v channels. Interestingly, the inhibitory variant STIM2.1 did not further decrease the endogenous STIM1-mediated SOCE in contrast to findings by Miederer et al (2015) and Rana et al. (2015). These results and recent findings by Ramesh et al. (2021) indicate that STIM-mediated inhibition of VGCE is more likely a long-term effect due to enhanced internalization of the VGCC and/or reduced Ca_v expression mediated through a SOCE-sensitive transcription factor. Since both mechanisms mediate Ca^{2+} influx, this negative feedback regulation could be just an indirect mechanism to adjust Ca^{2+} influx dependent on the expression levels of VGCC, STIM and ORAI but without STIM directly

affecting Ca$_v$ channel function. However, analysis of the VGCE in the STIM2.3-stable cell line could help to further elucidate the mechanism of Ca$_v$ inhibition.

SH-SY5Y cells can be differentiated into more mature neuron-like cells expressing neuronal markers using retinoic acid and BDNF [Pezzini et al. 2017]. In addition to morphological changes, differentiation of SH-SY5Y WT and STIM$^{-/-}$ cells increased VGCE and simultaneously reduced SOCE for WT and SH-SY5Y STIM2$^{-/-}$ cells (Fig. 25, Fig. 26) confirming previous studies [Brown et al. 2005; Whitworth et al. 2019]. While the reduced SOCE in differentiated cells is mediated by a decrease in ORAI1 expression, increase in VGCE is based on the high-voltage activated channels Ca$_v$1 and Ca$_v$2 [Toselli et al. 1991; Whitworth et al. 2019]. Upon differentiation, knockout of STIM no longer appears to affect K$^+$ induced Ca^{2+} influx and the number of responding cells indicating that upregulation of VGCE is independent of SOCE upon differentiation. Pezzini et al. (2017) demonstrated in a transcriptomic and bioinformatic analysis of RA-differentiated SH-SY5Y cells significant downregulation of VGCC γ-subunits and significant upregulation of the VGCC β2-subunit, STIM1 and ORAI3. While γ-subunits suppress VGCC function by triggering a hyperpolarization shift [reviewed in Black III 2003], β2-subunits promote surface expression of Ca$_v$ channels and thereby enhance channel activation [reviewed in Buraei and Yang 2013]. Additionally, Ca$_v$β2 prevents voltage-independent inactivation of high-voltage activated channels in response to GPCR-mediated PIP$_2$ depletion by stabilizing the Ca^{2+} channel [reviewed in Buraei and Yang 2013]. In T cells, overexpression of ORAI3 inhibits SOCE and might interfere with STIM1/ORAI1 gating in heteromeric CRAC channel complexes [Alansary et al. 2015]. In conclusion, differential expression of SOCE and VGCC components upon differentiation might not be an interdependent regulation but more likely supports an independent negative feedback mechanism to adjust Ca^{2+} signaling.

Role of the PBD in STIM2-mediated NFAT translocation

SOCE as the main Ca^{2+} influx pathway in immune cells regulates activation and nuclear translocation of the transcription factor NFAT following calcineurin-mediated dephosphorylation. The scaffolding protein AKAP79 interacts with the ORAI1 N terminus and recruits the signalosome complex consisting of calcineurin, NFAT, calmodulin and ORAI1 and thereby couples NFAT activation to local Ca^{2+} signals [Kar et al. 2014; Kar, Lin, et al. 2021]. Assembly of the signaling complex is facilitated by STIM2 targeting STIM1/ORAI1 complexes to AKAP79. Deletion of the PBD in STIM1 abolished

99

NFAT translocation, which was rescued by STIM2 over-expression [Son et al. 2020]. Hence, it was unclear, whether the PBD in STIM2 is required for NFAT activation and stabilization of the signalosome complex. In control transfected cells, Ca^{2+} release from internal stores is not sufficient to trigger NFAT translocation confirming previous findings [Kar et al. 2011]. Over-expression of STIM2.2 and STIM2.3 led to nuclear NFAT translocation in SH-SY5Y STIM1/STIM2$^{-/-}$ cells independent of STIM1, whereas deletion of the PBD in STIM2 (STIM2.2Δ5K) abolished activation of NFAT due to insufficient Ca^{2+} influx. Both SOCE and NFAT activation was rescued by the simultaneous mutation of both EB binding motifs in STIM2.2 2xIP+Δ5K (Fig. 27). These results demonstrate that STIM2-mediated NFAT activation per se does not necessarily require the PBD following Tg-induced store depletion. In contrast, deletion of the PBD in STIM1 only slightly affected Ca^{2+} influx but completely abolished NFAT translocation. Additionally, NFAT activation does not linearly correlate with Ca^{2+} influx [Son et al. 2020; Knapp et al. 2022], however, Kar et al. (2011) reported, that increased Ca^{2+} concentrations result in augmented NFAT translocation compared to lower concentrations. STIM2.2-mediated Ca^{2+} influx is sufficient to induce maximal NFAT activation at rest and STIM2.2 2xIPΔ5K induces the same NFAT translocation as STIM2.3 despite a reduced Ca^{2+} entry, thus, the increased STIM2.3-mediated SOCE does not further enhance NFAT translocation. Strikingly, basal NFAT translocation under resting conditions was only observed in STIM2.2-expressing cells but not in cells expressing STIM2 proteins lacking the PBD (i.e. STIM2.3, STIM2.2 2xIP+Δ5K) despite increased resting Ca^{2+} levels (Fig. 27). These results indicate that the PBD more likely stabilizes the signalosome complex and promotes translocation of NFAT under conditions with only mild store depletion, with STIM2.3 potentially preventing untimely activation. An artificial STIM2.3 containing the PBD should restore basal NFAT translocation. Nuclear accumulation of NFAT is determined by long-lasting Ca^{2+} signals and required for gene expression, whereas nuclear export is a slow process requiring re-phosphorylation [Kar et al. 2011]. In this context, enhanced STIM2.3-mediated SOCE could extent the time of nuclear NFAT accumulation modulating gene expression.

In neurons, the transcription factor CREB mainly mediates gene expression regulating growth, synaptic plasticity and neuroprotection. In contrast to NFAT, activation of CREB requires its phosphorylation by the cAMP-dependent PKA in response to external stimuli including growth factors and depolarization [Lonze and Ginty 2002]. In addition

to its pivotal role in immune cell function, NFAT is of critical importance to neurons. The scaffolding protein AKAP79/150 couples Ca^{2+} influx through L-type Ca^{2+} channels (LTCC) to NFAT signaling by recruiting calcineurin [Oliveria et al. 2007; Murphy et al. 2019]. Additionally, anchoring of PKA to AKAP79/150 maintains basal LTCC activity and coupling to CaN/NFAT signaling [Murphy et al. 2014]. Enhanced neuronal activity results in NFAT-dependent upregulation of voltage-gated M-type channels KCNQ2/3 to suppress hyperexcitability in a negative feedback mechanism [J. Zhang and Shapiro 2012]. Furthermore, Graef et al. (2003) demonstrated that sustained NFAT activation is required for embryonic axonal growth induced by the growth factors neurotrophin and netrin. During synaptogenesis, axon terminal maturation is characterized by axonal remodeling and synaptic vesicle accumulation. While the latter is regulated by PKA/CREB signaling, morphological remodeling of axon terminals requires CaN/NFAT-dependent gene expression [Yoshida and Mishina 2005]. AKAP79 recruits the signalosome including STIM/ORAI complexes, promoting NFAT activation, thus, in the neuronal context, STIM2 could be involved in NFAT-dependent axonogenesis and synaptic plasticity. It is yet to be investigated whether the two STIM2 variants regulate distinct NFAT- or CREB-dependent functions due to differential localization.

Identification of STIM2 interaction partners

The identification of interaction partners provides insights into the physiological function of a protein, its regulatory mechanism and involvement in further cellular processes. In addition to STIM and ORAI isoforms, several proteins have been described to modulate Ca^{2+} influx through direct interaction with the SOCE components. While STIMATE is a positive SOCE regulator promoting oligomerization of STIM1 [Jing et al. 2015], SARAF initiates Ca^{2+} dependent inactivation [Raz Palty et al. 2012; Albarran et al. 2016]. In contrast, POST does not directly modulate SOCE activity, but formation of a STIM1/POST complex inhibits PMCA activity, thereby, maintaining high cytosolic Ca^{2+} concentrations [Krapivinsky et al. 2011]. However, interaction partners of STIM2 are less characterized. Hence, bimolecular fluorescence complementation assay was performed using already established bait proteins to identify STIM2 interaction partners. Since, insertion of the STIM2.3-specific domain leads to increased SOCE, interaction partners were analyzed following store depletion. So far, no differential interaction partners have been identified demonstrating that the C-terminal truncation in STIM2.3 does not interfere with binding of the hitherto analyzed proteins (Fig. 28A).

Both STIM2 variants only showed low interaction with superoxide dismutase 1 (SOD1), the L-type Ca^{2+} channel Ca_v1.2 (CACNA1C), phosphodiesterase 8B (PDE8B) and the non-selective cation channel TRPC5. These results indicate that Ca_v1.2 and PDE8B may be STIM1-exclusive interaction partners [Park et al. 2010; Dittmer et al. 2017; Knapp et al. 2022] or interaction of STIM2 with Ca_v channels is STIM1-dependent. Additionally, direct interaction of STIM1 with Ca_v1.2 requires Homer1 [Dionisio et al. 2015], which might not be sufficiently expressed in HEK STIM1/2$^{-/-}$ cells. Both STIM2.2 and STIM2.3 showed interaction with TRPC1 supporting the hypothesis of TRPC1-mediated Ca^{2+} influx contributing to the increased SOCE phenotype of the splice variant. No interaction was detected for EFEMP1, which served as a negative control, excluding complementation of the YFP without direct interaction of the examined proteins. However, subcellular localization and stability of the analyzed proteins affect the results, thus, appropriate negative controls are required [Kodama and Hu 2012]. In BiFC, potential sources of error, leading to false-positive or false-negative results, are low transfection efficiencies due to large plasmids, differential expression of the analyzed POI and effect of the tag on protein function. Hence, results from BiFC require further validation using either Co-IP or FRET analysis [Kudla and Bock 2016]. While BiFC showed prominent interaction of both STIM2 variants with synaptotagmin 2 (Syt2), Co-IP only identified Syt2 as an interaction partner of STIM2.2 (Fig. 28). Hence, co-immuno-precipitation of two membrane bound proteins such as STIM2 and synaptotagmin 2 may require stronger detergents. Due to insufficient solubilization, interaction of proteins located in different membranes may be abolished leading to false-negative results. In contrast to the usual detergent sodium-dodecyl-sulfate (SDS), dodecyl-β-D-maltoside (DDM) is a non-ionic mild detergent, which does not denature proteins. To confirm the obtained results, the experiment should be repeated under optimized buffer conditions using different detergents such as Tween20, NP40 or Triton X-100. A successful Co-IP requires sufficient solubilization and maintenance of the protein-protein interaction.

In order to identify splice-specific interaction partners, an IP with subsequent mass spectrometry (MS) can be performed. Alternative methods such as APEX2 or crosslinking are performed in intact cells with complex protein networks under native conditions offering advantages over Co-IP, which is performed in a cell-free system with artificial buffer conditions. The APEX2-based biotinylation assay also identifies transient interaction partners through covalent binding of biotin-phenoxyl radicals to proteins following incubation with H_2O_2. The biotin-labeled proteins are then enriched using

streptavidin-beads and analyzed using MS [Hung et al. 2016]. However, APEX2 labels all proteins in a maximum distance of 20nm, which could possibly identify false-positive interaction partners. Crosslinking substances such as DTSSP (3,3'-dithiobis sulfosuccinimidyl propionate) or EDC (1-ethyl-3-3-dimethylaminopropyl carbodiimide hydrochlorid) enhance weak interactions by covalently linking functional groups (e.g. amine or sulfhydryl) of interacting proteins [Chu et al. 2018].

In 2019, Chauhan et al. demonstrated interaction of STIM2 with the heterotrimeric AMP-activated protein kinase (AMPK), which regulates enegery metabolism in response to energy stress and ATP depletion. Moreover, STIM2 functions as a scaffolding protein promoting Ca^{2+}-induced phosphorylation of AMPK at Thr172 of the catalytic α-subunit by Ca^{2+}/Calmodulin dependent kinase kinase II, the upstream kinase activated by increased cytosolic Ca^{2+} concentrations [Chauhan et al. 2019]. Co-IP experiments confirmed previous findings (Fig. 29). Furthermore, STIM2.3 showed reduced interaction with and activation of AMPKα indicating that the interacting domain in STIM2 overlaps with the splice site spanning the amino acids 646 to 674. Due to increased basal Ca^{2+} levels, both STIM2.2 and STIM2.3 interact with AMPKα under resting conditions, which was enhanced upon store depletion. However, phosphorylation of AMPKα was reduced after store depletion demonstrating that AMPK activation requires direct interaction with STIM2 and does not linearly correlate with Ca^{2+} influx. Furthermore, Ca^{2+}-dependent phosphorylation of AMPKα is mediated by the CaMKKII, which also binds to the CAD in STIM2. Hence, store depletion might promote the interaction of STIM2 with ORAI, thereby resulting in reduced AMPKα phosphorylation due to diminished interaction with CaMKKII. In contrast, Tg-induced STIM2.2 activation resulting in C-terminal unfolding likely facilitates interaction with AMPKα. In addition to AMPK phosphorylation, analysis of further downstream targets such as ACC are required to quantify AMPK activity.

The organization of functional neuronal networks require PI3/Akt-dependent polarization, in which formation of one axon and differentiation of the residual neurites into dendrites are the basis for the unidirectional signal transduction [Yoshimura et al. 2006]. Axon formation is an energy consuming process requiring large amounts of ATP. In hippocampal neurons, activation of the main energy sensor AMPK disturbed association of PI3 kinase (PI3K) and the motor protein Kif5 preventing trafficking of PI3K to the axonal tip, polarization, and axon growth [Amato et al. 2011]. Two independent studies performed in cortical and hippocampal neurons reported that

enhanced activation of AMPK impairs axonogenesis as well as dendritic growth and arborization through suppression of mTOR and Akt signaling pathways [T. Williams et al. 2011; Ramamurthy et al. 2014]. However, catalytic activity of AMPK is not required for early neurogenesis, migration, or polarization [T. Williams et al. 2011]. Furthermore, acute axonal activation of AMPK leads to suppression of the retrograde transport of mitochondria, which are the main neuronal energy source. Hence, AMPK locally minimizes energy consumption and restores energy homeostasis during energy stress [Watters et al. 2020]. Moreover, AMPK couples neuronal energy metabolism to memory formation by regulating long term potentiation (LTP), a specific form of activity-dependent synaptic plasticity, in a mTOR-dependent manner. Thus, AMPK activity needs to be tightly regulated since any dysregulation detrimentally impacts synaptic plasticity [Potter et al. 2010; Marinangeli et al. 2018]. Chronic activation of AMPK results in reduced expression of synaptic proteins associated with synaptic stability in differentiated SH-SY5Y cells, demonstrating a crucial role of energy metabolism in proper neuronal functionality [Yang et al. 2022]. Whether STIM2 as a scaffolding protein is involved in neuronal CaMKKII-dependent AMPK regulation of axonal polarization and synaptic plasticity is yet to be investigated. However, these results suggest a splice-dependent regulation of AMPK activity. The novel splice variant STIM2.3 could positively regulate axonogenesis and synaptic plasticity through reduced AMPK activation.

During early stages of AD, synaptotoxic β-amyloid oligomers trigger CaMKKII-dependent hyperactivation of AMPK resulting in loss of dendritic spines in response to increased cytosolic Ca^{2+} levels [Mairet-Coello et al. 2013]. Recently, A. Lee et al. (2022) uncovered a mechanism, in which Aβ-dependent CaMKKII/AMPK induces phosphorylation of Tau, linking remodeling and fission of dendritic mitochondria to loss of dendritic spines [A. Lee et al. 2022]. Additionally, enhanced AMPK activity induces autophagic degradation of postsynaptic proteins [Domise et al. 2019]. The role of STIM2 in AMPK-induced synaptic loss during AD is yet to be analyzed. It remains to be investigated whether STIM2 is an upstream effector of the Ca^{2+}-dependent CaMKKII/AMPK pathway or an indirect downstream target. Despite loss of STIM2 and impaired neuronal SOCE during AD, STIM2.3 could display a neuroprotective function by preventing AMPK hyper-activation and loss of dendritic spines, a hallmark of neurodegeneration.

STIM2.3 positively regulates neuronal processes

The generation of stable splice-specific SH-SY5Y cells should provide insights into potential physiological functions of the novel STIM2.3. While the clonal cell line E12.1 stably expressed STIM2.3 increasing SOCE compared to the control cell line SH-SY5Y STIM2$^{-/-}$, stable expression of STIM2.2 in the clonal cell line G11.1 was not unequivocally confirmed (Fig. 30). Despite genomic detection of the plasmid DNA using primers amplifying the N and specific C terminus, expression of HA-tagged STIM2.2 has not been confirmed on protein level. Furthermore, SOCE was not increased in G11.1-cells compared to control cells, suggesting a compensatory mechanism to prevent persistently elevated STIM2.2-mediated Ca^{2+} levels. Possibly, further posttranslational processing of STIM2.2 cleaving the N terminus may result in a store independent STIM2, which is no longer capable of activating ORAI and SOCE following store depletion [Graham et al. 2011]. The observed molecular weight of STIM2.2 was slightly lower than the expected weight of ~100 kDa. In addition, an HA antibody failed to detect STIM2.2, supporting the hypothesis of altered N-terminal processing. Further experiments are required to investigate the underlying mechanism explaining the observed phenotype in the stable cell line G11.1. Localization analysis could clarify whether STIM2.2 no longer displays ER distribution or whether only the Ca^{2+} sensing EF hand is lacking to prevent excess Ca^{2+} overload. However, RNA Seq and subsequent Gene Ontology analysis revealed that STIM2.3 positively regulates axonogenesis, axon development and guidance (Fig. 31B). Although these pathways were identified as downregulated processes upon knockout of STIM2 (Fig. 32A), the associated genes are different for both STIM2 KO and STIM2.3 overexpression (Table A1;Table A3). Additionally, deletion of STIM1 did not significantly affect axonal development (Fig. 32C,D) indicating that axonogenesis and neuron development might be mainly STIM2-dependent processes. However, transcriptomic analysis of a STIM2.2-stable cell line is required to exclude overexpression artefacts and to validate the STIM2.3-specific effects. RNA Seq identified for the STIM2.3-stable cell line E12.1 the gene microtubule associated protein 6 (*MAP6*) as one of the DEGs responsible for axonal growth [Deloulme et al. 2015]. Furthermore, *NSG2* (neuronal vesicle trafficking associated 2), GABA receptor subunit β3 (*GABRB3*) and the gene encoding the voltage-gated M-type channel *KCNQ3* are upregulated in E12.1-cells. NSG2 is localized in the somato-dendritic arbors regulating trafficking of protein complexes and colocalizes with the postsynaptic Homer1. NSG2 directly interacts with the AMPA receptor subunits GluA1 and GluA2 [Chander et al. 2019]

suggesting that STIM2-dependent AMPAR trafficking [Garcia-Alvarez et al. 2015] may be mediated through NSG2. KCNQ3 is upregulated in response to LTCC-induced increase in cytosolic Ca^{2+} concentration to suppress hyperexcitability indicating that STIM2.3 may regulate neurotransmission in a NFAT-dependent manner [J. Zhang and Shapiro 2012]. In addition, the GABA receptor subunit β3 regulates assembly and trafficking of the inhibitory GABA receptor in the ER lumen, which determines neuronal excitability [Connolly et al. 1996; Jacob et al. 2008]. Moreover, binding of the microtubular-tracking protein EB3 to STIM2.2 is important for the maintenance of dendritic spines and disruption of the association results in a reduced number of mushroom spines [Pchitskaya et al. 2017]. Hence, STIM2.3, naturally lacking both C-terminal MBP attachment sites, may reduce the number of dendritic spines and thus, shape synaptic plasticity. In this context, a potential reduced sensitivity to partial store depletion of STIM2.3 might prevent increased Syt7-mediated excitatory spontaneous neurotransmission in response to ER stress [Chanaday et al. 2021].

In conclusion, these findings support a role of STIM2.3 in axonogenesis and synaptic plasticity. Whether splice specific regulation of neuronal development and neurotransmission is mediated through NFAT or AMPK signaling remains to be investigated. Additionally, further samples are required to confirm the obtained results, since RNA sequencing only analyses the transcriptome at certain conditions and time points. Differentiation of the STIM2.3-stable cell line E12.1 could provide additional information in a more neuron-like background. Further experiments validating potential STIM2.3-specific effects on axonal development and synaptic transmission could be performed in primary murine hippocampal neurons.

5.4 Outlook

Characterization of the gain-of-function STIM2.3 highlights the functional diversity of STIM splice variants outside their conventional role in immune cell response. Expression of STIM2.3 seems to be restricted to the nervous system and various experiments indicate a role in axon development and neurotransmission. However, there are still many unanswered questions. It remains to be investigated whether splicing of STIM2.3 is regulated in an age-, gender- or development-dependent manner. Bioinformatic analysis of publicly available RNA Seq data of different human brain regions could provide information whether splicing of STIM2.3 is associated with neurodegenerative

diseases. Furthermore, the role of the STIM2.3-specific amino acids remains to be investigated. The specific residues are not responsible for the SOCE-phenotype but may function as a novel binding site or mediate differential localization compared to STIM2.2. Future experiments analyzing neuronal localization of STIM2.3 and identification of splice specific interaction partners help to understand its physiological relevance. Despite the lack of a murine STIM2.3, primary murine hippocampal neurons infected with adeno-associated virus encoding the novel splice variant can be used for further experiments.

References

Ahmand, M., Ong, H. L., Saadi, H., Son, G. Y., Shokatian, Z., Terry, L. E., et al. (2022). "Functional communication between IP3R and STIM2 at subthreshold stimuli is a critical checkpoint for initiation of SOCE." *PNAS*, *104*, 1–12. doi:10.1016/j.ceca.2022.102574

Alansary, D., Bogeski, I., & Niemeyer, B. A. (2015). Facilitation of Orai3 targeting and store-operated function by Orai1. *Biochimica et Biophysica Acta (BBA) - Molecular Cell Research*, *1853*(7), 1541–1550. doi:10.1016/J.BBAMCR.2015.03.007

Alansary, D., Peckys, D. B., Niemeyer, B. A., & Jonge, N. De. (2020). Detecting single ORAI1 proteins within the plasma membrane reveals higher-order channel complexes. *Journal of Cell Science*, *133*. doi:10.1242/jcs.240358

Alansary, D., Schmidt, B., Dörr, K., Bogeski, I., Rieger, H., Kless, A., & Niemeyer, B. A. (2016). Thiol dependent intramolecular locking of Orai1 channels. *Scientific Reports*, *6*(May), 1–11. doi:10.1038/srep33347

Albarran, L., Lopez, J. J., Amor, N. Ben, Martin-Cano, F. E., Berna-Erro, A., Smani, T., et al. (2016). Dynamic interaction of SARAF with STIM1 and Orai1 to modulate store-operated calcium entry. *Scientific Reports*, *6*. doi:10.1038/srep24452

Amato, S., Liu, X., Zheng, B., Cantley, L., Rakic, P., & Man, H. Y. (2011). AMP-activated protein kinase regulates neuronal polarization by interfering with PI 3-kinase localization. *Science*, *332*(6026), 247–251. doi:10.1126/science.1201678

Anders, S., & Huber, W. (2010). Differential expression analysis for sequence count data. *Genome Biology*, *11*(R106). doi:10.1074/jbc.272.7.4310

Auten, R. L., & Davis, J. M. (2009). The Role of Oxygen in Health and Disease - A Series of Reviews Oxygen Toxicity and Reactive Oxygen Species : The Devil Is in the Details. *Pedriatic Research*, *66*(2), 121–127.

Baraniak, J. H. J., Zhou, Y., Nwokonko, R. M., & Gill, D. L. (2020). The Intricate Coupling Between STIM Proteins and Orai Channels. *Current Opinion in Physiology*, *17*, 106–114. doi:10.1016/j.cophys.2020.07.018.The

Barton, R. A., & Venditti, C. (2014). Rapid evolution of the cerebellum in humans and other great apes. *Current Biology*, *24*(20), 2440–2444. doi:10.1016/j.cub.2014.08.056

Bauer, M. C., O'Connell, D., Cahill, D. J., & Linse, S. (2008). Calmodulin binding to the polybasic C-termini of STIM proteins involved in store-operated calcium entry. *Biochemistry*, *47*(23), 6089–6091. doi:10.1021/bi800496a

Bell, N., Hann, V., Redfern, C. P. F., & Cheek, T. R. (2013). Store-operated Ca2+ entry in proliferating and retinoic acid-differentiated N- and S-type neuroblastoma cells. *Biochimica et Biophysica Acta*, *1833*(3), 643–651. doi:10.1016/j.bbamcr.2012.11.025

Berna-Erro, A., Braun, A., Kraft, R., Kleinschnitz, C., Schuhmann, M. K., Stegner, D., et al. (2009). STIM2 Regulates Capacitive Ca2+ Entry in Neurons and Plays a Key Role in Hypoxic Neuronal Cell Death. *Science Signaling*, *2*(93), 1–11. doi:10.1126/scisignal.2000522

Berridge, M.J. (1993). Inositol trisphosphate and calcium signalling. *Nature*, *361*(6410), 315–325. doi:10.1038/361315a0

Berridge, Michael J, Bootman, M. D., & Roderick, H. L. (2003). Calcium signalling: dynamics, homeostasis and remodelling. *Nature reviews. Molecular cell biology*, *4*(7), 517–529. doi:10.1038/nrm1155

Berridge, Michael J, Lipp, P., & Bootman, M. D. (2000). The versatility and universality of calcium signalling. *Nature reviews. Molecular cell biology*, *1*(1), 11–21. doi:10.1038/35036035

Bhardwaj, R., Augustynek, B. S., Ercan-Herbst, E., Kandasamy, P., Seedorf, M., Peinelt, C., & Hediger, M. A. (2020). Ca2+/calmodulin binding to STIM1 hydrophobic residues facilitates slow Ca2+-dependent inactivation of the ORAI1 channel. *Cellular Physiology and Biochemistry*, *54*(2), 252–270. doi:10.33594/000000218

Bhardwaj, R., Hedinger, M. A., & Demaurex, N. (2016). Redox modulation of STIM-ORAI signaling. *Cell Calcium*, 142–152. https://ac.els-cdn.com/S0143416016300252/1-s2.0-S0143416016300252-main.pdf?_tid=f5886820-2f67-471e-879d-49c612c9eff7&acdnat=1529832144_e1950e221f124725c2b85eeedeccb525

Bhardwaj, R., Uller, H.-M., Nickel, W., & Seedorf, M. (2013). Oligomerization and Ca2+/Calmodulin control bindig of the ER Ca2+ sensors STIM1 and STIM2 to plasma membrane lipids. *Biosci. Rep*, *33*(5), 833–845. doi:10.1042/BSR20130089

Black III, J. L. (2003). The Voltage-Gated Calcium Channel γ Subunits: A Review of the Literature. *Journal of Bioenergetics and Biomembranes*, *35*(6), 649–660. doi:10.1023/B:JOBB.0000008029.22650.c5

Bogeski, I., Kummerow, C., Al-Ansary, D., Schwarz, E. C., Koehler, R., Kozai, D., et al. (2010). Differential redox regulation of ORAI ion channels: a mechanism to tune cellular calcium signaling. *Science signaling*, *3*(115), ra24. doi:10.1126/scisignal.2000672

Böhm, J., Bulla, M., Urquhart, J. E., Malfatti, E., Williams, S. G., O'Sullivan, J., et al. (2017). ORAI1 Mutations with Distinct Channel Gating Defects in Tubular Aggregate Myopathy. *Human Mutation*, *38*(4), 426–438. doi:10.1002/humu.23172

Brandman, O., Liou, J., Park, W. S., & Meyer, T. (2007). STIM2 is a Feedback Regulator that Stabilizes Basal Cytosolic and Endoplasmic Reticulum Ca2+ Levels. *Cell*, *131*(7), 1327–1339. doi:10.1016/j.cell.2007.11.039

Brown, A. M., Riddoch, F. C., Robson, A., Redfern, C. P. F., & Cheek, T. R. (2005). Mechanistic and functional changes in Ca2+ entry after retinoic acid-induced differentiation of neuroblastoma cells. *Biochemical Journal*, *388*(3), 941–948. doi:10.1042/BJ20042127

Buraei, Z., & Yang, J. (2013). Structure and function of the β subunit of voltage-gated Ca2+ channels. *Biochimica et Biophysica Acta - Biomembranes*, *1828*(7), 1530–1540. doi:10.1016/j.bbamem.2012.08.028

Butorac, C., Muik, M., Derler, I., Stadlbauer, M., Lunz, V., Krizova, A., et al. (2019). A novel STIM1-Orai1 gating interface essential for CRAC channel activation. *Cell Calcium*, *79*(February), 57–67. doi:10.1016/j.ceca.2019.02.009

Cai, X., Zhou, Y., Nwokonko, R. M., Loktionova, N. A., Wang, X., Xin, P., et al. (2016). The Orai1 Store-operated Calcium Channel Functions as a Hexamer. *The Journal of biological chemistry*, *291*(50), 25764–25775. doi:10.1074/jbc.M116.758813

Calloway, N., Holowka, D., & Baird, B. (2010). Abasic sequence in STIM1 promotes Ca2+ influx by interacting with the C-terminal acidic coiled-coiled of Orai1. *Biochemistry*, *49*(6), 1067–1071. doi:doi:10.1021/bi901936q.

Carafoli, E. (1991). Calcium pump of the plasma membrane. *Physiol Rev*, *71*(1), 129–153. http://physrev.physiology.org.libproxy1.usc.edu/content/71/1/129?ijkey=b495f7 cffcfe589f19e05cd5e84e984f0dcede7a&keytype2=tf_ipsecsha

Carafoli, Ernesto. (1987). Intracellular Calcium Homeostasis. *Annu Rev Biochem*, *56*, 395–433. doi:10.1002/9781118675410

Carafoli, Ernesto, Santella, L., Branca, D., & Brini, M. (2001). Generation, Control, and Processing of Cellular Calcium Signals. *Critical Reviews in Biochemistry and Molecular Biology*, *36*(2), 107–260. doi:10.1080/20014091074183

Chanaday, N. L., Nosyreva, E., Shin, O. H., Zhang, H., Aklan, I., Atasoy, D., et al. (2021). Presynaptic store-operated Ca2+ entry drives excitatory spontaneous neurotransmission and augments endoplasmic reticulum stress. *Neuron*, *109*(8), 1314-1332.e5. doi:10.1016/j.neuron.2021.02.023

Chander, P., Kennedy, M. J., Winckler, B., & Weick, J. P. (2019). Neuron-specific Gene 2 (NSG2) encodes an AMPA receptor interacting protein that modulates excitatory neurotransmission. *eNeuro*, *6*(1). doi:10.1523/ENEURO.0292-18.2018

Chang, C.-L., Chen, Y.-J., Quintanilla, C. G., Hsieh, T.-S., & Liou, J. (2018). EB1 binding restricts STIM1 translocation to ER–PM junctions and regulates store-operated Ca2+ entry. *The Journal of Cell Biology*, *217*(6), 2047–2058. doi:10.1083/jcb.201711151

Chauhan, A. S., Liu, X., Jing, J., Lee, H., Yadav, R. K., Liu, J., et al. (2019). STIM2 interacts with AMPK and regulates calcium-induced AMPK activation. *FASEB journal : official publication of the Federation of American Societies for Experimental Biology*, *33*(2), 2957–2970. doi:10.1096/fj.201801225R

Chernyuk, D. P., Vlasova, O. L., Bezprozvanny, I. B., & Popugaeva, E. A. (2016). Hyperexpression of STIM2 protein lowers the amount of Abeta plaques in the brain of Alzheimer ' s disease mouse model. *St. Petersburg Polytechnical University Journal: Physics and Mathematics*, *2*(4), 329–336. doi:10.1016/j.spjpm.2016.11.009

Chu, F., Thornton, D. T., & Nguyen, H. T. (2018). Chemical cross-linking in the structural analysis of protein assemblies. *Methods*, *144*, 53–63. doi:10.1016/j.ymeth.2018.05.023.Chemical

Chung, S., Zhang, M., & Stathopulos, P. B. (2018). The 2β splice variation alters the structure and function of the stromal interaction molecule coiled-coil domains. *International Journal of Molecular Sciences*, *19*(11), 15–19. doi:10.3390/ijms19113316

Ciccarone, V., Spengler, B. A., Meyers, M. B., Biedler, J. L., & Ross, R. A. (1989). Phenotypic diversification in human neuroblastoma cells: expression of distinct neural crest lineages. *Cancer research*, *49*(1), 219–225.

Clapham, D. E. (1995). Calcium signaling. *Cell*. doi:10.1016/0092-8674(95)90408-5

Clapham, D. E. (2007). Calcium Signaling. *Cell*, *131*(6), 1047–1058. doi:10.1016/j.cell.2007.11.028

Connolly, C. N., Wooltorton, J. R. A., Smart, T. G., & Moss, S. J. (1996). Subcellular localization of γ-aminobutyric acid type A receptors is determined by receptor β subunits. *Proc Natl Acad Sci USA*, *93*(18), 9899–9904. doi:10.1073/pnas.93.18.9899

Covington, E. D., Wu, M. M., & Lewis, R. S. (2010). Essential Role for the CRAC Activation Domain in Store-dependent Oligomerization of STIM1. *Molecular Biology of the Cell*, *21*(11), 1897–1907. doi:10.1091/mbc.E10-02-0145

Darbellay, B., Arnaudeau, S., Bader, C. R., Konig, S., & Bernheim, L. (2011). STIM1L is a new actin-binding splice variant involved in fast repetitive Ca 2+ release. *Journal of Cell Biology*, *194*(2), 335–346. doi:10.1083/jcb.201012157

Deloulme, J. C., Gory-Fauré, S., Mauconduit, F., Chauvet, S., Jonckheere, J., Boulan, B., et al. (2015). Microtubule-associated protein 6 mediates neuronal connectivity through Semaphorin 3E-dependent signalling for axonal growth. *Nature Communications*, *6*. doi:10.1038/ncomms8246

Demuro, A., Penna, A., Safrina, O., Yeromin, A. V., Amcheslavsky, A., Cahalan, M. D., & Parker, I. (2011). Subunit stoichiometry of human Orai1 and Orai3 channels in closed and open states. *Proceedings of the National Academy of Sciences of the United States of America*, *108*(43), 17832–17837. doi:10.1073/pnas.1114814108

Derler, I., Butorac, C., Krizova, A., Stadlbauer, M., Muik, M., Fahrner, M., et al. (2018). Authentic CRAC channel activity requires STIM1 and the conserved portion of the Orai N terminus. *Journal of Biological Chemistry*, *293*(4), 1259–1270. doi:10.1074/jbc.M117.812206

Derler, I., Fahrner, M., Carugo, O., Muik, M., Bergsmann, J., Schindl, R., et al. (2009). Increased hydrophobicity at the N terminus/membrane interface impairs gating of the severe combined immunodeficiency-related ORAI1 mutant. *Journal of Biological Chemistry*, *284*(23), 15903–15915. doi:10.1074/jbc.M808312200

Derler, I., Plenk, P., Fahrner, M., Muik, M., Jardin, I., Schindl, R., et al. (2013). The extended transmembrane orai1 N-terminal (ETON) region combines binding interface and gate for orai1 activation by STIM1. *Journal of Biological Chemistry*, *288*(40), 29025–29034. doi:10.1074/jbc.M113.501510

Dionisio, N., Smani, T., Woodard, G. E., Castellano, A., Salido, G. M., & Rosado, J. A. (2015). Homer proteins mediate the interaction between STIM1 and Cav1.2 channels. *Biochimica et Biophysica Acta - Molecular Cell Research*, *1853*(5), 1145–1153. doi:10.1016/j.bbamcr.2015.02.014

Dittmer, P. J., Wild, A. R., Dell'Acqua, M. L., & Sather, W. A. (2017). STIM1 Ca2+Sensor Control of L-type Ca2+-Channel-Dependent Dendritic Spine Structural Plasticity and Nuclear Signaling. *Cell Reports*, *19*(2), 321–334. doi:10.1016/j.celrep.2017.03.056

Domise, M., Sauvé, F., Didier, S., Caillerez, R., Bégard, S., Carrier, S., et al. (2019). Neuronal AMP-activated protein kinase hyper-activation induces synaptic loss by an autophagy-mediated process. *Cell Death and Disease*, *10*(3). doi:10.1038/s41419-019-1464-x

Dörr, K., Kilch, T., Kappel, S., Alansary, D., Schwär, G., Niemeyer, B. A., & Peinelt, C. (2016). Cell type-specific glycosylation of Orai1 modulates store-operated Ca2+ entry. *Science Signaling*, *9*(418), ra25. doi:10.1126/scisignal.aaa9913

Dyrda, A., Koenig, S., & Frieden, M. (2020). STIM1 long and STIM1 gate differently TRPC1 during store-operated calcium entry. *Cell Calcium*, *86*(November 2019), 102134. doi:10.1016/j.ceca.2019.102134

Elorza, A., Márquez, Y., Cabrera, J. R., Sánchez-Trincado, J. L., Santos-Galindo, M., Hernández, I. H., et al. (2021). Huntington's disease-specific mis-splicing unveils key effector genes and altered splicing factors. *Brain*, *144*(7), 2009–2023. doi:10.1093/brain/awab087

Ercan, E., Chung, S. H., Bhardwaj, R., & Seedorf, M. (2012). Di-Arginine Signals and the K-Rich Domain Retain the Ca 2+ Sensor STIM1 in the Endoplasmic Reticulum. *Traffic*, *13*(7), 992–1003. doi:10.1111/j.1600-0854.2012.01359.x

Fahrner, M., Muik, M., Schindl, R., Butorac, C., Stathopulos, P., Zheng, L., et al. (2014). A coiled-coil clamp controls both conformation and clustering of stromal interaction molecule 1 (STIM1). *The Journal of biological chemistry*, *289*(48), 33231–44. doi:10.1074/jbc.M114.610022

Fahrner, M., Pandey, S. K., Muik, M., Traxler, L., Butorac, C., Stadlbauer, M., et al. (2018). Communication between N terminus and loop2 tunes Orai activation. *Journal of Biological Chemistry*, *293*(4), 1271–1285. doi:10.1074/jbc.M117.812693

Feske, S., Gwack, Y., Prakriya, M., Srikanth, S., Puppel, S.-H., Tanasa, B., et al. (2006). A mutation in Orai1 causes immune deficiency by abrogating CRAC channel function. *Nature*, *441*, 179–185. doi:10.1038/nature04702

Feske, S., Skolnik, E. Y., & Prakriya, M. (2012, June 15). Ion channels and transporters in lymphocyte function and immunity. *Nature reviews. Immunology*. doi:10.1038/nri3233

Garcia-Alvarez, G., Lu, B., Yap, K. A. F., Wong, L. C., Thevathasan, J. V., Lim, L., et al. (2015). STIM2 regulates PKA-dependent phosphorylation and trafficking of AMPARs. *Molecular Biology of the Cell*, *26*(6), 1141–1159. doi:10.1091/mbc.E14-07-1222

Garcia-alvarez, G., Shetty, M. S., Lu, B., Yap, K. A. F., Oh-Hora, M., Sajikumar, S., et al. (2015). Impaired spatial memory and enhanced long-term potentiation in mice with forebrain-specific ablation of the Stim genes. *Frontiers in Behavioral Neuroscience*, *9*(July), 1–12. doi:10.3389/fnbeh.2015.00180

Garcia, D., & Shaw, R. J. (2017). AMPK : Mechanisms of Cellular Energy Sensing and Restoration of Metabolic Balance. *Molecular Cell*, *66*(6), 789–800. doi:10.1016/j.molcel.2017.05.032

Gibhardt, C. S., Cappello, S., Bhardwaj, R., Hediger, M. A., Schindl, R., Bogeski, I., et al. (2020). Oxidative Stress-Induced STIM2 Cysteine Modifications Suppress Store-Operated Calcium Entry ll Oxidative Stress-Induced STIM2 Cysteine Modifications Suppress Store-Operated Calcium Entry. doi:10.1016/j.celrep.2020.108292

Gilson, A. (2016). *Identification of new STIM splice variants and expression in the mouse brain during healthy ageing*. Universität des Saarlandes.

Gowans, G. J., Hawley, S. A., Ross, F. A., & Hardie, D. G. (2013). AMP is a true physiological regulator of amp-activated protein kinase by both allosteric activation and enhancing net phosphorylation. *Cell Metabolism*, *18*(4), 556–566. doi:10.1016/j.cmet.2013.08.019

Graef, I. A., Wang, F., Charron, F., Chen, L., Neilson, J., Tessier-Lavigne, M., & Crabtree, G. R. (2003). Neurotrophins and netrins require calcineurin/NFAT signaling to stimulate outgrowth of embryonic axons. *Cell*, *113*(5), 657–670. doi:10.1016/S0092-8674(03)00390-8

Graham, S. J. L., Dziadek, M. A., & Johnstone, L. S. (2011). A Cytosolic STIM2 Preprotein Created by Signal Peptide Inefficiency Activates ORAI1 in a Store-independent Manner. *Journal of Biological Chemistry*, *286*(18), 16174–16185. doi:10.1074/jbc.M110.206946

Grigoriev, I., Gouveia, S. M., van der Vaart, B., Demmers, J., Smyth, J. T., Honnappa, S., et al. (2008). STIM1 Is a MT-Plus-End-Tracking Protein Involved in Remodeling of the ER. *Current Biology*, *18*(3), 177–182. doi:10.1016/j.cub.2007.12.050

Gruszczynska-Biegala, J., Sladowska, M., & Kuznicki, J. (2016). AMPA Receptors Are Involved in Store-Operated Calcium Entry and Interact with STIM Proteins in Rat Primary Cortical Neurons. *Frontiers in cellular neuroscience*, *10*(October), 251. doi:10.3389/fncel.2016.00251

Gruszczynska-Biegala, J., Strucinska, K., Maciag, F., Majewski, L., Sladowska, M., & Kuznicki, J. (2020). STIM Protein-NMDA2 Receptor Interaction Decreases NMDA-Dependent Calcium Levels in Cortical Neurons. *Cells*, *9*(1), 160. doi:10.3390/cells9010160

Grynkiewicz, G., Poenie, M., & Tsien, R. Y. (1985). A new generation of Ca2+ indicators with greatly improved fluorescence properties. *Journal of Biological Chemistry*, *260*(6), 3440–3450. doi:3838314

Hammad, A. S., Yu, F., Botheju, W. S., Elmi, A., Alcantara-Adap, E., & Machaca, K. (2021). Phosphorylation of STIM1 at ERK/CDK sites is dispensable for cell migration and ER partitioning in mitosis. *Cell Calcium*, *100*(July), 102496. doi:10.1016/j.ceca.2021.102496

Hartmann, J., Karl, R., Alexander, R. P. D., Adelsberger, H., Brill, M. S., Rühlmann, C., et al. (2014). STIM1 Controls Neuronal Ca2+ Signaling, mGluR1-Dependent Synaptic Transmission, and Cerebellar Motor Behavior. *Neuron*, *82*(3), 635–644. doi:10.1016/j.neuron.2014.03.027

Hawkins, B. J., Irrinki, K. M., Mallilankaraman, K., Lien, Y.-C., Wang, Y., Bhanumathy, C. D., et al. (2010). S-glutathionylation activates STIM1 and alters mitochondrial homeostasis. *The Journal of cell biology*, *190*(3), 391–405. doi:10.1083/jcb.201004152

Hawley, S. A., Selbert, M. A., Goldstein, E. G., Edelman, A. M., Carling, D., & Hardie, D. G. (1995). 5'-AMP activates the AMP-activated protein kinase cascade, and Ca2+/calmodulin activates the calmodulin-dependent protein kinase I cascade, via three independent mechanisms. *Journal of Biological Chemistry*, *270*(45), 27186–27191. doi:10.1074/jbc.270.45.27186

Herzig, S., & Shaw, R. J. (2018). AMPK: Guardian of metabolism and mitochondrial homeostasis. *Nature Reviews Molecular Cell Biology*, *19*(2), 121–135. doi:10.1038/nrm.2017.95

Honnappa, S., Gouveia, S. M., Weisbrich, A., Damberger, F. F., Bhavesh, N. S., Jawhari, H., et al. (2009). An EB1-Binding Motif Acts as a Microtubule Tip Localization Signal. *Cell*, *138*(2), 366–376. doi:10.1016/j.cell.2009.04.065

Hoth, M., & Penner, R. (1992). Depletion of intracellular calcium stores activates a calcium current in mast cells. *Nature*, *355*(6358), 353–356. doi:10.1038/355353a0

Hou, X., Pedi, L., Diver, M. M., & Long, S. B. (2012a). Crystal Structure of the Calcium release-activated Calcium Channel Orai. *Biophysical Chemistry*, *338*(6112), 1308–1313. doi:10.1016/j.immuni.2010.12.017.Two-stage

Hou, X., Pedi, L., Diver, M. M., & Long, S. B. (2012b). Crystal structure of the calcium release-activated calcium channel Orai. *Science*, *338*(6112), 1308–1313. doi:10.1126/science.1228757

Hung, V., Udeshi, N. D., Lam, S. S., Loh, K. H., Cox, K. J., Pedram, K., et al. (2016). Spatially resolved proteomic mapping in living cells with the engineered peroxidase APEX2. *Nature Protocols*, *11*(3), 456–475. doi:10.1038/nprot.2016.018

Jacob, T. C., Moss, S. J., & Jurd, R. (2008). GABAa receptor trafficking and its role in the dynamic modulation of neuronal inhibition. *Nat Rev Neurosci.*, *9*(5), 331–343. doi:10.1038/nrn2370.GABA

Ji, W., Xu, P., Li, Z., Lu, J., Liu, L., Zhan, Y., et al. (2008). Functional stoichiometry of the unitary calcium-release-activated calcium channel. *PNAS*, *105*(36), 13668–13673. doi:10.1073/pnas.0806499105

Jing, J., He, L., Sun, A., Quintana, A., Ding, Y., Ma, G., et al. (2015). Proteomic mapping of ER – PM junctions identifies STIMATE as a regulator of Ca 2 + influx. *Nature Cell Biology*, *17*(10), 1339–1347. doi:10.1038/ncb3234

Kar, P., Barak, P., Zerio, A., Lin, Y.-P., Parekh, A. J., Watts, V. J., et al. (2021). AKAP79 Orchestrates a Cyclic AMP Signalosome Adjacent to Orai1 Ca2+ Channels. *Function*, *2*(5). doi:10.1093/function/zqab036

Kar, P., Lin, Y., Bhardwaj, R., Tucker, C. J., Bird, G. S., & Hediger, M. A. (2021). The N terminus of Orai1 couples to the AKAP79 signaling complex to drive NFAT1 activation by local. *PNAS*, *118*(19). doi:10.1073/pnas.2012908118

Kar, P., Nelson, C., & Parekh, A. B. (2011). Selective activation of the transcription factor NFAT1 by calcium microdomains near Ca2+ release-activated Ca2+ (CRAC) channels. *Journal of Biological Chemistry*, *286*(17), 14795–14803. doi:10.1074/jbc.M111.220582

Kar, P., Samanta, K., Kramer, H., Morris, O., Bakowski, D., & Parekh, A. B. (2014). Dynamic assembly of a membrane signaling complex enables selective activation of NFAT by orai1. *Current Biology*, *24*(12), 1361–1368. doi:10.1016/j.cub.2014.04.046

Kato, H., Uno, I., Ishikawa, T., & Takenawa, T. (1989). Activation of phosphatidylinositol kinase and phosphatidylinositol-4-phosphate kinase by cAMP in Saccharomyces cerevisiae. *Journal of Biological Chemistry*, *264*(6), 3116–3121. doi:10.1016/s0021-9258(18)94039-1

Kawasaki, T., Lange, I., & Feske, S. (2009). A minimal regulatory domain in the C terminus of STIM1 binds to and activates ORAI1 CRAC channel. *Biochem Biophys Res Commun*, *385*(1), 49–54. doi:10.1016/j.bbrc.2009.05.020.

Kim, K. M., Rana, A., & Park, C. Y. (2019). Orai1 inhibitor STIM2β regulates myogenesis by controlling SOCE dependent transcriptional factors. *Scientific Reports*, *9*(1), 1–11. doi:10.1038/s41598-019-47259-5

Knapp, M. L., Alansary, D., Poth, V., Förderer, K., Sommer, F., Zimmer, D., et al. (2022). A longer isoform of Stim1 is a negative SOCE regulator but increases cAMP-modulated NFAT signaling. *EMBO reports*, *23*(3), 1–20. doi:10.15252/embr.202153135

Kodama, Y., & Hu, C. D. (2012). Bimolecular fluorescence complementation (BiFC): A 5-year update and future perspectives. *BioTechniques*, *53*(5), 285–298. doi:10.2144/000113943

Korzeniowski, M. K., Manjarrés, I. M., Varnai, P., & Balla, T. (2012). Activation of STIM1-Orai1 involves an intramolecular switching mechanism. *Science Signaling*, *3*(148). doi:10.1126/scisignal.2001122.ACTIVATION

Kovalevich, J., & Langford, D. (2013). Considerations for the Use of SH-SY5Y Neuroblastoma Cells in Neurobiology. *Methods Mol Biol.*, *1078*, 9–21. doi:10.1007/978-1-62703-640-5

Kraft, R. (2015). STIM and ORAI proteins in the nervous system. *Channels*, *9*(5), 244–252. doi:10.1080/19336950.2015.1071747

Krapivinsky, G., Krapivinsky, L., Stotz, S. C., Manasian, Y., & Clapham, D. E. (2011). POST, partner of stromal interaction molecule 1 (STIM1), targets STIM1 to multiple transporters. *Proceedings of the National Academy of Sciences of the United States of America*, *108*(48), 19234–19239. doi:10.1073/pnas.1117231108

Kudla, J., & Bock, R. (2016). Lighting the way to protein-protein interactions: Recommendations on best practices for bimolecular fluorescence complementation analyses. *Plant Cell*, *28*(5), 1002–1008. doi:10.1105/tpc.16.00043

Kunkl, M., Porciello, N., Mastrogiovanni, M., Capuano, C., Lucantoni, F., Moretti, C., et al. (2017). ISA-2011B, a phosphatidylinositol 4-phosphate 5-kinase a inhibitor, impairs CD28-dependent costimulatory and pro-inflammatory signals in human T lymphocytes. *Frontiers in Immunology*, *8*(APR), 1–10. doi:10.3389/fimmu.2017.00502

Kushnireva, L., Korkotian, E., & Segal, M. (2021). Calcium Sensors STIM1 and STIM2 Regulate Different Calcium Functions in Cultured Hippocampal Neurons, *12*(January), 1–12. doi:10.3389/fnsyn.2020.573714

Lee, A., Kondapalli, C., Virga, D. M., Lewis, T. L., Koo, S. Y., Ashok, A., et al. (2022). Aβ42 oligomers trigger synaptic loss through CAMKK2-AMPK-dependent effectors coordinating mitochondrial fission and mitophagy. *Nature Communications*, *13*(1). doi:10.1038/s41467-022-32130-5

Lee, S. K., Lee, M. H., Jeong, S. J., Qin, X., Lee, A. R., Park, H., & Park, C. Y. (2020). The inactivation domain of STIM1 acts through intramolecular binding to the coiled-coil domain in the resting state. *Journal of Cell Science*, *133*(1). doi:10.1242/jcs.237354

Li, X., Wu, G., Yang, Y., Fu, S., Liu, X., Kang, H., et al. (2017). Calmodulin dissociates the STIM1-Orai1 complex and STIM1 oligomers. *Nature communications*, *8*(1), 1042. doi:10.1038/s41467-017-01135-w

Li, Z., Lu, J., Xu, P., Xie, X., Chen, L., & Xu, T. (2007). Mapping the interacting domains of STIM1 and Orai1 in Ca2+ release-activated Ca2+ channel activation. *The Journal of biological chemistry*, *282*(40), 29448–56. doi:10.1074/jbc.M703573200

Liou, J., Kim, M. L., Heo, W. Do, Jones, J. T., Myers, J. W., Ferrell, J. E., & Meyer, T. (2005, July). STIM Is a Ca(2+) Sensor Essential for Ca(2+)-Store-Depletion-Triggered Ca(2+) Influx. *Current biology : CB*. doi:10.1016/j.cub.2005.05.055

Lis, A., Peinelt, C., Beck, A., Parvez, S., Monteilh-Zoller, M., Fleig, A., & Penner, R. (2007). CRACM1, CRACM2, and CRACM3 Are Store-Operated Ca2+ Channels with Distinct Functional Properties. *Current Biology*, *17*(9), 794–800. doi:10.1016/j.cub.2007.03.065

Lomax, R. B., Camello, C., Coppenolle, F. Van, Petersen, O. H., & Tepikin, A. V. (2002). Basal and Physiological Ca $2^{/-}$ Leak from the Endoplasmic Reticulum of Pancreatic Acinar Cells SECOND MESSENGER–ACTIVATED CHANNELS AND TRANSLOCONS*. doi:10.1074/jbc.M201845200

Lonze, B. E., & Ginty, D. D. (2002). Function and regulation of CREB family transcription factors in the nervous system. *Neuron*, *35*(4), 605–623. doi:10.1016/S0896-6273(02)00828-0

Lunz, V., Romanin, C., & Frischauf, I. (2019). STIM1 activation of Orai1. *Cell Calcium*, *77*(September 2018), 29–38. doi:10.1016/j.ceca.2018.11.009

Lytton, J., Westlin, M., & Hanley, M. R. (1991). Thapsigargin inhibits the sarcoplasmic or endoplasmic reticulum Ca-ATPase family of calcium pumps. *The Journal of biological chemistry*, *266*(26), 17067–71. http://www.ncbi.nlm.nih.gov/pubmed/1832668. Accessed 14 June 2018

Mairet-Coello, G., Courchet, J., Pieraut, S., Courchet, V., Maximov, A., & Polleux, F. (2013). The CAMKK2-AMPK Kinase Pathway Mediates the Synaptotoxic Effects of Aβ Oligomers through Tau Phosphorylation. *Neuron*, *78*(1), 94–108. doi:10.1016/j.neuron.2013.02.003

Majewski, L., & Kuznicki, J. (2015). SOCE in neurons : Signaling or just refilling ? *Biochimica et Biophysica Acta*, *1853*, 1940–1952. doi:10.1016/j.bbamcr.2015.01.019

Majewski, L., Maciąg, F., Boguszewski, P. M., & Kuznicki, J. (2020). Transgenic mice overexpressing human STIM2 and ORAI1 in neurons exhibit changes in behavior and calcium homeostasis but show no signs of neurodegeneration. *International Journal of Molecular Sciences*, *21*(3), 1–15. doi:10.3390/ijms21030842

Majewski, T., Maciag, F., Boguszewski, P. M. P. M., Wasilewska, I., Wiera, G., Wójtowicz, T., et al. (2016). Overexpression of STIM1 in neurons in mouse brain improves contextual learning and impairs long-term depression. *Biochimica et Biophysica Acta - Molecular Cell Research*, *1864*(6), 1071–1087. doi:10.1016/j.bbamcr.2016.11.025

Malli, R., Naghdi, S., Romanin, C., & Graier, W. F. (2008). Cytosolic Ca2+ prevents the subplasmalemmal clustering of STIM1: an intrinsic mechanism to avoid Ca2+ overload. *Journal of cell science*, *121*(Pt 19), 3133–3139. doi:10.1242/jcs.034496

Marinangeli, C., Didier, S., Ahmed, T., Caillerez, R., Domise, M., Laloux, C., et al. (2018). AMP-Activated Protein Kinase Is Essential for the Maintenance of Energy Levels during Synaptic Activation. *iScience*, *9*, 1–13. doi:10.1016/j.isci.2018.10.006

McNally, B. A., Somasundaram, A., Jairaman, A., Yamashita, M., & Prakriya, M. (2013). The C- and N-terminal STIM1 binding sites on Orai1 are required for both trapping and gating CRAC channels. *The Journal of physiology*, *591*(11), 2833–50. doi:10.1113/jphysiol.2012.250456

Mcnally, B. A., Yamashita, M., Engh, A., & Prakriya, M. (2009). Structural determinants of ion permeation in CRAC channels. *PNAS*, *106*(52), 22516–22521. doi:10.1073/pnas.0909574106

Miederer, A.-M., Alansary, D., Schwär, G., Lee, P.-H., Jung, M., Helms, V., & Niemeyer, B. a. (2015). A STIM2 splice variant negatively regulates store-operated calcium entry. *Nature Communications*, *6*, 6899. doi:10.1038/ncomms7899

Mignen, O., Thompson, J. L., & Shuttleworth, T. J. (2008a). Both Orai1 and Orai3 are essential components of the arachidonate-regulated Ca2+-selective (ARC) channels. *Journal of Physiology*, *586*(1), 185–195. doi:10.1113/jphysiol.2007.146258

Mignen, O., Thompson, J. L., & Shuttleworth, T. J. (2008b). Orai1 subunit stoichiometry of the mammalian CRAC channel pore. *Journal of Physiology*, *586*(2), 419–425. doi:10.1113/jphysiol.2007.147249

Moraes, F., & Góes, A. (2016). A decade of human genome project conclusion: Scientific diffusion about our genome knowledge. *Biochemistry and Molecular Biology Education*, *44*(3), 215–223. doi:10.1002/bmb.20952

Morin, G., Bruechle, N. O., Singh, A. R., Knopp, C., Jedraszak, G., Elbracht, M., et al. (2014). Gain-of-Function Mutation in STIM1 (P.R304W) Is Associated with Stormorken Syndrome. *Human Mutation*, *35*(10), 1121–1132. doi:10.1002/humu.22621

Muik, M., Fahrner, M., Derler, I., Schindl, R., Bergsmann, J., Frischauf, I., et al. (2009). A cytosolic homomerization and a modulatory domain within STIM1 C terminus determine coupling to ORAI1 channels. *Journal of Biological Chemistry*, *284*(13), 8421–8426. doi:10.1074/jbc.C800229200

Mullins, F. M., & Lewis, R. S. (2016). The inactivation domain of STIM1 is functionally coupled with the Orai1 pore to enable Ca 2+ -dependent inactivation. *The Journal of General Physiology*, *147*(2), 153–164. doi:10.1085/jgp.201511438

Mungai, P. T., Waypa, G. B., Jairaman, A., Prakriya, M., Dokic, D., Ball, M. K., & Schumacker, P. T. (2011). Hypoxia Triggers AMPK Activation through Reactive Oxygen Species-Mediated Activation of Calcium Release-Activated Calcium Channels. *Molecular and Cellular Biology*, *31*(17), 3531–3545. doi:10.1128/mcb.05124-11

Murphy, J. G., Crosby, K. C., Dittmer, P. J., Sather, W. A., & Dell'Acqua, M. L. (2019). AKAP79/150 recruits the transcription factor NFAT to regulate signaling to the nucleus by neuronal L-type Ca2+ channels. *Molecular Biology of the Cell*, *30*(14), 1743–1756. doi:10.1091/mbc.E19-01-0060

Murphy, J. G., Sanderson, J. L., Gorski, J. A., Scott, J. D., Catterall, W. A., Sather, W. A., & Dell'Acqua, M. L. (2014). AKAP-anchored PKA maintains neuronal L-type calcium channel activity and NFAT transcriptional signaling. *Cell Reports*, *7*(5), 1577–1588. doi:10.1016/j.celrep.2014.04.027

Nelson, M. E., Parker, B. L., Burchfield, J. G., Hoffman, N. J., Needham, E. J., Cooke, K. C., et al. (2019). Phosphoproteomics reveals conserved exercise-stimulated signaling and AMPK regulation of store-operated calcium entry. *The EMBO Journal*, *38*(24), 1–20. doi:10.15252/embj.2019102578

Nesin, V., Wiley, G., Kousi, M., Ong, E.-C., Lehmann, T., Nicholl, D. J., et al. (2014). Activating mutations in STIM1 and ORAI1 cause overlapping syndromes of tubular myopathy and congenital miosis. *Proceedings of the National Academy of Sciences of the United States of America*, *111*(11), 4197–202. doi:10.1073/pnas.1312520111

Nicholls, D., & Åkerman, K. (1982). Mitochondrial calcium transport. *Biochimica et Biophysica Acta*, *683*(1), 57–88. doi:10.1016/0304-4173(82)90013-1

Niggli, V., Adunyah, E. S., Penniston, J. T., & Carafoli, E. (1981). Purified (Ca2+-Mg2+)-ATPase of the erythrocyte membrane. Reconstitution and effect of calmodulin and phospholipids. *Journal of Biological Chemistry*, *256*(1), 395–401. doi:10.1016/s0021-9258(19)70149-5

Olianas, M. C., Dedoni, S., & Onali, P. (2014). Involvement of store-operated Ca2+ entry in activation of AMP-activated protein kinase and stimulation of glucose uptake by M3 muscarinic acetylcholine receptors in human neuroblastoma cells. *Biochimica et Biophysica Acta - Molecular Cell Research*, *1843*(12), 3004–3017. doi:10.1016/j.bbamcr.2014.09.012

Oliveria, S. F., Dell'Acqua, M. L., & Sather, W. A. (2007). AKAP79/150 anchoring of calcineurin controls neuronal L-type Ca2+ channel activity and nuclear signaling. *Neuron*, *55*(2), 261–275. doi:10.1016/j.neuron.2007.06.032.AKAP79/150

Ong, H. L., De Souza, L. B., Zheng, C., Cheng, K. T., Liu, X., Goldsmith, C. M., et al. (2015). STIM2 enhances receptor-stimulated Ca2+signaling by promoting recruitment of STIM1 to the endoplasmic reticulum-plasma membrane junctions. *Science Signaling*, *8*(359), ra3. doi:10.1126/scisignal.2005748

Palty, R., Silverman, W. F., Hershfinkel, M., Caporale, T., Sensi, S. L., Parnis, J., et al. (2010). NCLX is an essential component of mitochondrial Na+/Ca2+ exchange. *Proceedings of the National Academy of Sciences*, *107*(1), 436–441. doi:10.1073/pnas.0908099107

Palty, Raz, & Isacoff, E. Y. (2016). Cooperative binding of stromal interaction molecule 1 (STIM1) to the N and C termini of calcium release-activated calcium modulator 1 (Orai1). *Journal of Biological Chemistry*, *291*(1), 334–341. doi:10.1074/jbc.M115.685289

Palty, Raz, Raveh, A., Kaminsky, I., Meller, R., & Reuveny, E. (2012). SARAF inactivates the store operated calcium entry machinery to prevent excess calcium refilling. *Cell*, *149*(2), 425–438. doi:10.1016/j.cell.2012.01.055

Park, C. Y., Hoover, P. J., Mullins, F. M., Bachhawat, P., Covington, D., Raunser, S., et al. (2009). STIM1 clusters and Activates CRAC Channels via Direct Binding of a Cytosolic Domain to Orai1. *Cell*, *136*(5), 876–890. doi:10.1016/j.cell.2009.02.014.STIM1

Park, C. Y., Shcheglovitov, A., & Dolmetsch, R. E. (2010). The CRAC Channel Activator STIM1 Binds and Inhibits L-Type Voltage-Gated Calcium Channels. *Science*, *330*(6000), 101–105. doi:10.1126/science.1191027 Channel

Patil, C. S., Li, H., Lavine, N. E., Shi, R., Bodalia, A., Siddiqui, T. J., & Jackson, M. F. (2022). ER-resident STIM1 / 2 couples Ca 2 + entry by NMDA receptors to pannexin-1 activation, 1–11. doi:10.1073/pnas.2112870119/-/DCSupplemental.Published

Pchitskaya, E., Kraskovskaya, N., Chernyuk, D., Popugaeva, E., Zhang, H., Vlasova, O., & Bezprozvanny, I. (2017). Stim2-Eb3 Association and Morphology of Dendritic Spines in Hippocampal Neurons. *Scientific Reports*, *7*(1), 1–13. doi:10.1038/s41598-017-17762-8

Peacock, M. (2010). Calcium metabolism in health and disease. *Clinical journal of the American Society of Nephrology : CJASN*, *5 Suppl 1*(Supplement 1), S23-30. doi:10.2215/CJN.05910809

Penna, A., Demuro, A., Yeromin, A. V., Zhang, S. L., Safrina, O., Parker, I., & Cahalan, M. D. (2008). The CRAC channel consists of a tetramer formed by Stim-induced dimerization of Orai dimers. *Nature*, *456*(7218), 116–120. doi:10.1038/nature07338.The

Pezzini, F., Bettinetti, L., Di Leva, F., Bianchi, M., Zoratti, E., Carrozzo, R., et al. (2017). Transcriptomic Profiling Discloses Molecular and Cellular Events Related to Neuronal Differentiation in SH-SY5Y Neuroblastoma Cells. *Cellular and Molecular Neurobiology*, *37*(4), 665–682. doi:10.1007/s10571-016-0403-y

Pizzo, P., Lissandron, V., Capitanio, P., & Pozzan, T. (2011). Ca2+ signalling in the Golgi apparatus. *Cell Calcium*, *50*(2), 184–192. doi:10.1016/j.ceca.2011.01.006

Popugaeva, E., Pchitskaya, E., Speshilova, A., Alexandrov, S., Zhang, H., Vlasova, O., & Bezprozvanny, I. (2015). STIM2 protects hippocampal mushroom spines from amyloid synaptotoxicity. *Molecular neurodegeneration*, *10*(1), 37. doi:10.1186/s13024-015-0034-7

Poth, V. (2018). *Charakterisierung der neuen STIM2-SPleißvariante STIM2.3*.

Potter, W. B., O'Riordan, K. J., Barnett, D., Osting, S. M. K., Wagoner, M., Burger, C., & Roopra, A. (2010). Metabolic regulation of neuronal plasticity by the energy sensor AMPK. *PLoS ONE*, *5*(2). doi:10.1371/journal.pone.0008996

Pozo-Guisado, E., Casas-Rua, V., Tomas-Martin, P., Lopez-Guerrero, A. M., Martin-Romero, F. J., & Alvarez-Barrientos, A. (2013). Phosphorylation of stim1 at erk1/2 target sites regulates interaction with the microtubule plus-end binding protein eb1. *Journal of Cell Science*, *126*(14), 3170–3180. doi:10.1242/jcs.125054

Prakriya, M., & Lewis, R. S. (2015). Store-Operated Calcium Channels. *Physiological Reviews*, *95*(4), 1383–1436. doi:10.1152/physrev.00020.2014

Prins, D., Groenendyk, J., Touret, N., & Michalak, M. (2011). Modulation of STIM1 and capacitative Ca2+ entry by the endoplasmic reticulum luminal oxidoreductase ERp57. *EMBO reports*, *12*(11), 1182–1188. doi:10.1038/embor.2011.173

Putney, J W. (1986). A model for receptor-regulated calcium entry. *Cell calcium*, *7*(1), 1–12. http://www.ncbi.nlm.nih.gov/pubmed/2420465. Accessed 17 May 2017

Putney, James W. (1986). A model for receptor-regulated calcium entry. *Cell Calcium*, *7*(1), 1–12. doi:10.1016/0143-4160(86)90026-6

Ramamurthy, S., Chang, E., Cao, Y., Zhu, J., & Ronnett, G. V. (2014). AMPK activation regulates neuronal structure in developing hippocampal neurons. *Neuroscience*, *259*, 13–24. doi:10.1016/j.neuroscience.2013.11.048

Ramesh, G., Jarzembowski, L., Schwarz, Y., Poth, V., Konrad, M., Knapp, M. L., et al. (2021). A short isoform of STIM1 confers frequency-dependent synaptic enhancement. *Cell Reports*, *34*(11). doi:10.1016/j.celrep.2021.108844

Rana, A., Yen, M., Sadaghiani, A. M., Malmersj??, S., Park, C. Y., Dolmetsch, R. E., & Lewis, R. S. (2015). Alternative splicing converts STIM2 from an activator to an inhibitor of store-operated calcium channels. *Journal of Cell Biology*, *209*(5), 653–670. doi:10.1083/jcb.201412060

Rizzuto, R., De Stefani, D., Raffaello, A., & Mammucari, C. (2012). Mitochondria as sensors and regulators of calcium signalling. *Nature Reviews Molecular Cell Biology*, *13*(9), 566–578. doi:10.1038/nrm3412

Rizzuto, R., Marchi, S., Bonora, M., Aguiari, P., Bononi, A., De Stefani, D., et al. (2009). Ca2+ transfer from the ER to mitochondria: When, how and why. *Biochimica et Biophysica Acta - Bioenergetics*, *1787*(11), 1342–1351. doi:10.1016/j.bbabio.2009.03.015

Rizzuto, R., Pinton, P., Carrington, W., Fay, F. S., Fogarty, K. E., Lifshitz, L. M., et al. (1998). Close Contacts with the Endoplasmic Reticulum as Determinants of Mitochondrial Ca 2+ Responses. *Science*, *280*(5370), 1763–1766. doi:10.1126/science.280.5370.1763

Roos, J., DiGregorio, P. J., Yeromin, A. V., Ohlsen, K., Lioudyno, M., Zhang, S., et al. (2005). STIM1, an essential and conserved component of store-operated Ca 2+ channel function. *Journal of Cell Biology*, *169*(3), 435–445. doi:10.1083/jcb.200502019

Ryu, X. C., Jang, X. D. C., Jung, X. D., Kim, X. Y. G., Shim, X. H. G., Ryu, H., et al. (2017). STIM1 Regulates Somatic Ca2+ Signals and Intrinsic Firing Properties of Cerebellar Purkinje Neurons. *The Journal of Neuroscience*, *37*(37), 8876–8894. doi:10.1523/JNEUROSCI.3973-16.2017

Sanders, M. J., Grondin, P. O., Hegarty, B. D., Snowden, M. A., & Carling, D. (2007). Investigating the mechanism for AMP activation of the AMP-activated protein kinase cascade. *Biochemical Journal*, *403*(1), 139–148. doi:10.1042/BJ20061520

Sauer, H., Wartenberg, M., & Hescheler, J. (2001). Reactive oxygen species as intracellular messengers during cell growth and differentiation. *Cellular physiology and biochemistry*, *11*(4), 173–186. doi:10.1159/000047804

Shalygin, A., Kolesnikov, D., Glushankova, L., Gusev, K., Skopin, A., Skobeleva, K., & Kaznacheyeva, E. V. (2021). Role of STIM2 and Orai proteins in regulating TRPC1 channel activity upon calcium store depletion. *Cell Calcium*, *97*. doi:10.1016/j.ceca.2021.102432

Shaw, J. P., Utz, P. J., Durand, D. B., Toole, J. J., Emmel, E. A., & Crabtree, G. R. (1988). Identification of a putative regulator of early T cell activation genes. *Science*, *241*(4862), 202–205. doi:10.1126/science.3260404

Shaw, P. J., & Feske, S. (2012). Physiological and pathophysiological functions of SOCE in the immune system. *Frontiers in bioscience (Elite edition)*, *4*, 2253–68. doi:10.2741/E540

Shrestha, N., Hye-Ryong Shim, A., Maneshi, M. M., See-Wai Yeung, P., Yamashita, M., & Prakriya, M. (2022). Mapping interactions between the CRAC activation domain and CC1 regulating the activity of the ER Ca2+ sensor STIM1. *Journal of Biological Chemistry*, *298*(8). doi:10.1016/j.jbc.2022.102157

Son, G. Y., Subedi, K. P., Ong, H. L., Noyer, L., Saadi, H., Zheng, C., et al. (2020). STIM2 targets Orai1/STIM1 to the AKAP79 signaling complex and confers coupling of Ca2+ entry with NFAT1 activation. *Proceedings of the National Academy of Sciences of the United States of America*, *117*(28), 16638–16648. doi:10.1073/pnas.1915386117

Sousa, S. R., Vetter, I., Ragnarsson, L., & Lewis, R. J. (2013). Expression and Pharmacology of Endogenous Cav Channels in SH-SY5Y Human Neuroblastoma Cells. *PLoS ONE*, *8*(3). doi:10.1371/journal.pone.0059293

Stathopulos, P. B., Zheng, L., & Ikura, M. (2009). Stromal interaction molecule (STIM) 1 and STIM2 calcium sensing regions exhibit distinct unfolding and oligomerization kinetics. *Journal of Biological Chemistry*, *284*(2), 728–732. doi:10.1074/jbc.C800178200

Stathopulos, P. B., Zheng, L., Li, G.-Y., Plevin, M. J., & Ikura, M. (2008). Structural and Mechanistic Insights into STIM1-Mediated Initiation of Store-Operated Calcium Entry. *Cell*, *135*(1), 110–122. doi:10.1016/j.cell.2008.08.006

Stein, B. D., Calzolari, D., Hellberg, K., Hu, Y. S., He, L., Hung, C. M., et al. (2019). Quantitative In Vivo Proteomics of Metformin Response in Liver Reveals AMPK-Dependent and -Independent Signaling Networks. *Cell Reports*, *29*(10), 3331-3348.e7. doi:10.1016/j.celrep.2019.10.117

Subedi, K. P., Ong, H. L., Son, G. Y., Liu, X., & Ambudkar, I. S. (2018). STIM2 Induces Activated Conformation of STIM1 to Control Orai1 Function in ER-PM Junctions. *Cell Reports*, *23*(2), 522–534. doi:10.1016/j.celrep.2018.03.065

Sun, S., Zhang, H., Liu, J., Popugaeva, E., Xu, N.-J., Feske, S., et al. (2014, April). Reduced Synaptic STIM2 Expression and Impaired Store-Operated Calcium Entry Cause Destabilization of Mature Spines in Mutant Presenilin Mice. *Neuron*. doi:10.1016/j.neuron.2014.02.019

Suter, M., Riek, U., Tuerk, R., Schlattner, U., Wallimann, T., & Neumann, D. (2006). Dissecting the role of 5′-AMP for allosteric stimulation, activation, and deactivation of AMP-activated protein kinase. *Journal of Biological Chemistry*, *281*(43), 32207–32216. doi:10.1074/jbc.M606357200

Tazi, J., Bakkour, N., & Stamm, S. (2009). Alternative splicing and disease. *Biochimica et Biophysica Acta - Molecular Basis of Disease*, *1792*(1), 14–26. doi:10.1016/j.bbadis.2008.09.017

Tedeschi, V., Sisalli, M. J., Pannaccione, A., Piccialli, I., Molinaro, P., Annunziato, L., & Secondo, A. (2022). Na+/Ca2+ exchanger isoform 1 (NCX1) and canonical transient receptor potential channel 6 (TRPC6) are recruited by STIM1 to mediate Store-Operated Calcium Entry in primary cortical neurons. *Cell Calcium*, *101*(December 2021). doi:10.1016/j.ceca.2021.102525

Thompson, J. L., Mignen, O., & Shuttleworth, T. J. (2009). The Orai1 severe combined immune deficiency mutation and calcium release-activated Ca2+ channel function in the heterozygous condition. *The Journal of biological chemistry*, *284*(11), 6620–6. doi:10.1074/jbc.M808346200

Thompson, J. L., & Shuttleworth, T. J. (2013). Molecular basis of activation of the arachidonate-regulated Ca2+ (ARC) channel, a store-independent orai channel, by plasma membrane STIM1. *Journal of Physiology*, *591*(14), 3507–3523. doi:10.1113/jphysiol.2013.256784

Tirado-lee, L., Yamashita, M., & Prakriya, M. (2015). Conformational Changes in the Orai1 C-Terminus Evoked by STIM1 Binding, 1–17. doi:10.1371/journal.pone.0128622

Toselli, M., Masetto, S., Rossi, P., & Taglietti, V. (1991). Characterization of a Voltage-dependent Calcium Current in the Human Neuroblastoma Cell Line SH-SY5Y During Differentiation. *The European journal of neuroscience*, *3*(6), 514–522. doi:10.1111/j.1460-9568.1991.tb00838.x

Vang, A. G., Basole, C., Dong, H., Nguyen, R. K., Housley, W., Guernsey, L., et al. (2016). Differential expression and function of PDE8 and PDE4 in effector T cells: Implications for PDE8 as a drug target in inflammation. *Frontiers in Pharmacology*, *7*(AUG), 1–9. doi:10.3389/fphar.2016.00259

Vig, M., Beck, A., Billingsley, J. M., Lis, A., Parvez, S., Peinelt, C., et al. (2006). CRACM1 Multimers Form the Ion-Selective Pore of the CRAC Channel. *Current Biology*, *16*(20), 2073–2079. doi:10.1016/j.cub.2006.08.085

Wang, X., Wang, Y., Zhou, Y., Hendron, E., Mancarella, S., Andrake, M. D., et al. (2014). Distinct Orai-coupling domains in STIM1 and STIM2 define the Orai-activating site. *Nature communications*, *5*, 3183. doi:10.1038/ncomms4183

Wang, Yan, Liu, J., Huang, B. O., Xu, Y.-M., Li, J., Huang, L.-F., et al. (2015). Mechanism of alternative splicing and its regulation. *Biomedical reports*, *3*(2), 152–158. doi:10.3892/br.2014.407

Wang, Youjun, Deng, X., Mancarella, S., Hendron, E., Eguchi, S., Soboloff, J., et al. (2010). The Calcium Store Sensor, STIM1, Reciprocally Controls Orai and Cav1.2 Channels. *Science*, *330*(6000), 105–109. doi:10.1126/science.1191086

Watters, O., Connolly, N. M. C., König, H. G., Düssmann, H., & Prehn, J. H. M. (2020). AMPK Preferentially Depresses Retrograde Transport of Axonal Mitochondria during Localized Nutrient Deprivation. *Journal of Neuroscience*, *40*(25), 4798–4812. doi:10.1523/JNEUROSCI.2067-19.2020

Whitworth, C. L., Redfern, C. P. F., & Cheek, T. R. (2019). Differentiation-Induced Remodelling of Store-Operated Calcium Entry Is Independent of Neuronal or Glial Phenotype but Modulated by Cellular Context. *Molecular Neurobiology*, *56*(2), 857–872. doi:10.1007/s12035-018-1112-y

Williams, R. T., Manji, S. S. M., Parker, N. J., Hancock, M. S., Van Stekelenburg, L., Eid, J.-P. P., et al. (2001). Identification and characterization of the STIM (stromal interaction molecule) gene family: coding for a novel class of transmembrane proteins. *The Biochemical journal*, *357*(Pt 3), 673–685. doi:10.1042/0264-6021:3570673

Williams, T., Courchet, J., Viollet, B., Brenman, J. E., & Polleux, F. (2011). AMP-activated protein kinase (AMPK) activity is not required for neuronal development but regulates axogenesis during metabolic stress. *Proceedings of the National Academy of Sciences of the United States of America*, *108*(14), 5849–5854. doi:10.1073/pnas.1013660108

Woods, A., Dickerson, K., Heath, R., Hong, S. P., Momcilovic, M., Johnstone, S. R., et al. (2005). Ca2+/calmodulin-dependent protein kinase kinase-β acts upstream of AMP-activated protein kinase in mammalian cells. *Cell Metabolism*, *2*(1), 21–33. doi:10.1016/j.cmet.2005.06.005

Woods, A., Johnstone, S. R., Dickerson, K., Leiper, F. C., Fryer, L. G. D., Neumann, D., et al. (2003). LKB1 Is the Upstream Kinase in the AMP-Activated Protein Kinase Cascade. *Current Biology*, *13*(22), 2004–2008. doi:10.1016/j.cub.2003.10.031

Xiao, H., Jedrychowski, M. P., Schweppe, D. K., Huttlin, E. L., Yu, Q., Heppner, D. E., et al. (2020). A Quantitative Tissue-Specific Landscape of Protein Redox Regulation during Aging. *Cell*, *180*, 968–983. doi:10.1016/j.cell.2020.02.012

Xie, J., Ma, G., Zhou, L., He, L., Zhang, Z., Tan, P., et al. (2022). Identification of a STIM1 Splicing Variant that Promotes Glioblastoma Growth. *Advanced Science*, *2103940*, 1–15. doi:10.1002/advs.202103940

Yang, A. J. T., Mohammad, A., Tsiani, E., Necakov, A., & MacPherson, R. E. K. (2022). Chronic AMPK Activation Reduces the Expression and Alters Distribution of Synaptic Proteins in Neuronal SH-SY5Y Cells. *Cells*, *11*(15), 1–14. doi:10.3390/cells11152354

Yap, K. A. F., Shetty, M. S., Garcia-Alvarez, G., Lu, B., Alagappan, D., Oh-Hora, M., et al. (2017). STIM2 regulates AMPA receptor trafficking and plasticity at hippocampal synapses. *Neurobiology of Learning and Memory*, *138*, 54–61. doi:10.1016/J.NLM.2016.08.007

Yen, M., Lokteva, L. A., & Lewis, R. S. (2016). Functional Analysis of Orai1 Concatemers Supports a Hexameric Stoichiometry for the CRAC Channel. *Biophysical Journal*, *111*(9), 1897–1907. doi:10.1016/j.bpj.2016.09.020

Yoshida, T., & Mishina, M. (2005). Distinct roles of calcineurin-nuclear factor of activated T cells and protein kinase A - cAMP response element-binding protein signaling in presynaptic differentiation. *Journal of Neuroscience*, *25*(12), 3067–3079. doi:10.1523/JNEUROSCI.3738-04.2005

Yoshimura, T., Arimura, N., & Kaibuchi, K. (2006). Signaling networks in neuronal polarization. *Journal of Neuroscience*, *26*(42), 10626–10630. doi:10.1523/JNEUROSCI.3824-06.2006

Yu, G., Wang, L. G., Han, Y., & He, Q. Y. (2012). ClusterProfiler: An R package for comparing biological themes among gene clusters. *OMICS A Journal of Integrative Biology*, *16*(5), 284–287. doi:10.1089/omi.2011.0118

Yuan, J. P., Zeng, W., Dorwart, M. R., Choi, Y., Paul, F., & Muallem, S. (2009). SOAR and the polybasic STIM1 domains gate and regulate the Orai channels. *Nat Cell Biol.*, *11*(3), 337–343. doi:10.1038/ncb1842.SOAR

Zhang, J., & Shapiro, M. S. (2012). Activity-Dependent Transcriptional Regulation of M-Type (Kv7) K+ Channels by AKAP79/150-Mediated NFAT Actions. *Neuron*, *76*(6), 1133–1146. doi:10.1016/j.neuron.2012.10.019

Zhang, S. L., Yeromin, A. V, Zhang, X. H.-F., Yu, Y., Safrina, O., Penna, A., et al. (2006). Genome-wide RNAi screen of Ca(2+) influx identifies genes that regulate Ca(2+) release-activated Ca(2+) channel activity. *Proceedings of the National Academy of Sciences of the United States of America*, *103*(24), 9357–9362. doi:10.1073/pnas.0603161103

Zheng, L., Stathopulos, P. B., Schindl, R., Li, G.-Y., Romanin, C., & Ikura, M. (2011). Auto-inhibitory role of the EF-SAM domain of STIM proteins in store-operated calcium entry. *Proceedings of the National Academy of Sciences of the United States of America*, *108*(4), 1337–42. doi:10.1073/pnas.1015125108

Zheng, S., Zhou, L., Ma, G., Zhang, T., Liu, J., Li, J., et al. (2018). Calcium store refilling and STIM activation in STIM- and Orai-deficient cell lines. *Pflugers Archiv : European journal of physiology*, *470*, 1555–1567.

Zhou, J., Song, J., & Wu, S. (2019). Autophagic degradation of stromal interaction molecule 2 mediates disruption of neuronal dendrites by endoplasmic reticulum stress. *Journal of Neurochemistry*, *151*(3), 351–369. doi:https://doi.org/10.1111/jnc.14712

Zhou, Yandong, Cai, X., Loktionova, N. A., Wang, X., Nwokonko, R. M., Wang, X., et al. (2016). The STIM1-binding site nexus remotely controls Orai1 channel gating. *Nature Communications*, *7*, 13725. doi:10.1038/ncomms13725

Zhou, Yandong, Nwokonko, R. M., Cai, X., Loktionova, N. A., Abdulqadir, R., Xin, P., et al. (2018). Cross-linking of Orai1 channels by STIM proteins. *Proceedings of the National Academy of Sciences of the United States of America*, *115*(15), E3398–E3407. doi:10.1073/pnas.1720810115

Zhou, Yubin, Ramachandran, S., Oh-hora, M., Rao, A., & Hogan, P. G. (2010). Pore architecture of the ORAI1 store-operated calcium channel. *PNAS*, *107*(11), 4896–4901. doi:10.1073/pnas.1001169107

Zweifach, A., & Lewis, R. S. (1993). Mitogen-Regulated Ca2+ Current of T-Lymphocytes Is Activated by Depletion of Intracellular Ca2+ Stores. *Proceedings of the National Academy of Sciences of the United States of America*, *90*(13), 6295–6299.

List of Figures

List of Tables

Abbreviations

6-Bnz-cAMP	N6-Benzoyladenosine-3,'5'-cyclic monophosphate
aa	amino acid
AD	Alzheimer's Disease
AKAP79	A kinase anchoring protein 79
AM	acetoxymethyl ester
AMPA	α-amino-3-hydroxy-5-methyl-4-isoxazolepropionic acid
AMPAR	AMPA receptor
AMPK	AMP-activated protein kinase
ADP	adenosine diphosphate
AMP	adenosine monophosphate
ATP	adenosine triphosphate
AUC	area under the curve
BCA	bicinoquinic acid
BDNF	brain derived neurotrophic factor
BiFC	bimolecular fluorescence complementation
BLAST	Basic Local Alignment Search Tool
Ca^{2+}	calcium, calcium
CAD	channel activating domain
CaM	calmodulin
CaMKII	Ca^{2+}/calmodulin dependent kinase II
CaMKKII/β	Ca^{2+}/calmodulin dependent kinase kinase II/β
cAMP	cyclic adenosine monophosphate
CC	coiled-coiled
CDI	Ca^{2+} dependent inactivation
cDNA	complementary DNA
cEF	canonical EF hand
Co-IP	co-immuniprecipitation
CRAC	Ca^{2+} release activated Ca^{2+}
Ct	cycle threshold
DAG	diacylglycerol
DDM	dodecyl-ß-D-maltoside
DMEM	Dulbecco's modified Eagle medium
DNA	desoxyribonuleic acid
dNTP	desoxynucleoside triphosphate
EB	end binding
EDTA	ethylenediaminetetraacetic acid
EFEMP1	EGF containing Fibulin Extracellular Matrix Protein 1
ER	endoplasmic reticulum
ERK1/2	extracellular signal regulated kinase 1/2
ETON	extended transmembrane ORAI1 N-terminal
FCDI	fast Ca^{2+} dependent inactivation
FCS	fetal calf serum
FLOT1	Flotilin 1
FRET	Förster resonance energy transfer
gDNA	genomic DNA
GFP	green fluorescent protein
GO	Gene Ontology
GPCR	G-protein coupled receptor

gRNA	guide RNA, guide RNA
GTQ	gen technology quality
HA	hemagglutinin
HD	Huntington's Disease
HEK	human embryonic kidney
I_{CRAC}	Ca^{2+} release activated Ca^{2+} current
ID	inhibitory domain
IP_3	inositol 1,4,5 trisphosphate
IP_3R	IP_3 receptor
LKB1	liver kinase B1
LTCC	L-type Ca^{2+} channel
MBP	microtubular binding protein
MCU	mitochondrial Ca^{2+} uniporter
MEF2C	myocyte enhancer factor 2C
MEM	Minimum essential medium
mGluR1	metabotropic glutamate receptor
MIP	maximum intensity projection
MS	mass spectrometry
n/hEF	non-canonical/hidden EF hand
NCLX	$Na^+/Li^+/Ca^{2+}$ exchanger
NCX	Na^+/Ca^{2+} exchanger
NEAA	non-essential amino acids
NFAT	nuclear factor of activated T cells
NMDA	N methyl D aspartat
NMDAR	NMDA receptor
nSOC	neuronal store-operated Ca^{2+} entry
OASF	ORAI activating small fragment
Panx1	pannexin 1
PBD	polybasic domain
PBS	phosphate-buffered saline
PCR	polymerase chain reaction
PDE8B	phosphodiesterase 8B
PF	PDE8B inhibitor PF-04957325
PI3K	phosphatidylinositol 3-kinase
PIP_2	phosphatidylinositol 4,5 bisphosphate
PIP5K	phosphatidylinositol-4-phosphate kinase 5
PKA	protein kinase A
PLC	phospholipase C
PM	plasma membrane
PMCA	plasma membrane Ca^{2+} ATPase
PN	Purkinje neurons
POI	protein of interest
POST	partner of STIM
qRT-PCR	quantitative real-time PCR
RA	retinoic acid
RNA	ribonucleic acid
RNA Seq	RNA sequencing
ROC	receptor operated channels
ROS	reactive oxygen species
rpm	revolutions per minute

RT	room temperature
RyR	ryanodine receptor
SAM	sterile alpha motif
SEM	standard error of the mean
SD	standard deviation
SDS	sodium-dodecyl sulfate
SDS-PAGE	sodium-dodecyl-sulfate polyacrylamide gel electrophoresis
SERCA	sarco/endoplasmic reticulum Ca^{2+} ATPase
S_n/P_n	serine/proline rich region
SOAR	STIM1 ORAI activating region
SOC	store-operated channels
SOCE	store-operated Ca^{2+} entry
SOD1	superoxide dismutase 1
SPCA	secretory pathway Ca^{2+} ATPase
STIM	stromal interaction molecule
Syt7	synaptotagmin 7
TBP	TATA box binding protein
Tg	Thapsigargin
TIRFM	total internal reflection fluorescence microscopy
TMD	transmembrane domain
TRPC	transient receptor potential canonical
VGCC	voltage-gated Ca^{2+} channels
VGCE	voltage-gated Ca^{2+} entry
YFP	yellow fluorescent protein
YFPc	C-terminal part of YFP (aa 156-720)
YFPn	N-terminal part of YFP (aa 1-155)

Appendix

Table A1 **Upregulated GO terms and the associated genes in SH-SY5Y E12.1**

GO term	Genes
positive regulation of neurogenesis	*TRIM67/NKX2-5/ID2/NRCAM/MAP6/ISLR2/PLXNA4*
positive regulation of differentiation	*TRIM67/NKX2-5/NRCAM/MAP6/ISLR2/PLXNA4*
neuron projection guidance	*NRCAM/GAP43/UNC5D/PLXNA4/PIK3R1/CRMP1*
axon guidance	*NRCAM/GAP43/UNC5D/PLXNA4/PIK3R1/CRMP1*
CNS neuron differentiation	*DCX/ID4/CHD5/UNC5D/PLXNA4*
regulation of membrane potential	*PID1/KCNQ3/NRCAM/CHRNA9/GABRB3/RIMS4/JUN*
forebrain development	*DCX/CASP3/ID4/ID2/POU3F3/CHD5/PLXNA4*
telencephalon development	*DCX/CASP3/ID4/ID2/POU3F3/PLXNA4*
axonogenesis	*DCX/NRCAM/MAP6/ISLR2/GAP43/UNC5D/ PLXNA4/PIK3R1/CRMP1*
axon development	*DCX/NRCAM/MAP6/ISLR2/GAP43/UNC5D/ PLXNA4/PIK3R1/CRMP1/JUN*

Table A2 **Downregulated GO terms and the associated genes in SH-SY5Y E12.1**

GO term	Genes
receptor tyrosine kinase binding	*ANGPT1/LRP4*
membrane microdomain	*ANGPT1/LRP4/CNTN1*
membrane raft	*ANGPT1/LRP4/CNTN1*
negative regulation of Wnt signaling pathway	*LRP4/TBX18/TLE2*
urogenital system development	*ANGPT1/LRP4/ROBO2/TBX18*
renal system development	*ANGPT1/LRP4/ROBO2/TBX18*
regulation of peptidyl-tyrosine phosphorylation	*ANGPT1/LRP4/CNTN1/IGF2*

Table A3 **Downregulated GO terms and the associated genes in SH-SY5Y STIM2$^{-/-}$**

GO term	Genes
axonogenesis	*SEMA3D/APOE/XK/DLX5/LHX9/UNC5D/SLITRK6/ POU3F2/SPON2/SLITRK5/POU4F1/MATN2/LGI1/ PTPRM/NRP2/NRXN1/GFRA1/BDNF/SCN1B/LRP4/ FGF13/FOXD1/LPAR3/SLITRK3*
axon development	*SEMA3D/APOE/XK/DLX5/LHX9/UNC5D/SLITRK6/ POU3F2/SPON2/SLITRK5/POU4F1/MATN2/LGI1/ PTPRM/NRP2/NRXN1/GFRA1/BDNF/SCN1B/LRP4/ PLP1/FGF13/FOXD1/LPAR3/SLITRK3*
positive regulation of PI3K signaling	*ANGPT1/HGF/ERBB4/DCN/WNT16/IGF2/PRR5L/PDGFC*
positive regulation of MAPK cascade	*ANGPT1/HGF/TNFRSF1A/ERBB4/WNT16/TRIM5/ GPR37/IGF2/BMP4/TLR6/PLCB1/MAP3K21/TENM1/ SYK/TNFRSF10A/FGF1/FGFR4/MAP3K15/SOX2/*

	PDGFC/LPAR3/TLR4
synapse assembly	PTPRD/SLITRK6/SLITRK5/POU4F1/NRXN1/CLSTN2/ BDNF/CBLN2/LRP4/PCLO/SLITRK3
axon guidance	SEMA3D/DLX5/LHX9/UNC5D/SPON2/MATN2/LGI1/ PTPRM/NRP2/NRXN1/GFRA1/BDNF/SCN1B/FOXD1
neuron projection guidance	SEMA3D/DLX5/LHX9/UNC5D/SPON2/MATN2/LGI1/ PTPRM/NRP2/NRXN1/GFRA1/BDNF/SCN1B/FOXD1
protein tyrosine kinase activity	FGFRL1/HGF/ERBB4/TEC/NRP2/MAP3K21/FGF5/ SYK/PDGFRL/FGF1/FGFR4/TXK
G-protein coupled receptor activity	GPRC5B/SFRP4/GPR37/GPR150/GPR22/GRM8/ PDGFRL/P2RY2/GPR156/CALCRL/PROKR2/MCHR1/ PRLHR/GPR1/LPAR3

Table A4 **Upregulated GO terms and the associated genes in SH-SY5Y STIM2$^{-/-}$**

GO term	Genes
voltage-gated calcium channel complex	CACNA1D/CACNA1G/CACNG2/CATSPERE/RYR1
retinoic acid binding	SERPINA5/CYP27C1/RXRA/CYP26A1
heart development	SCUBE1/ID2/ID1/ID3/PLN/SNAI2/GATA5/ RXRA/HES1/DNAAF1/HTR2B/SNAI1/DKK1/OLFM1/ NEXN/APLNR/SOX18/MSX2/PROX2/SCX/TH/ MYLK2/TBX1/RYR1
metal ion transmembrane transporter activity	SLC12A7/TRPV4/KCNT1/SCN4B/STIM2/ABCC8/ CACNA1D/CACNA1G/ATP2B2/CACNG2/ASIC4/ SLC34A3/ASIC3/SHROOM2/SLC1A1/SLC6A11/ SCN2B/KCNQ3/SLC6A17/SLC13A3/KCNMA1/SLC9B1/ RYR1
developmental maturation	ID2/ASCL1/PAEP/HES1/PTH1R/LYL1/WNT10B/ SOX18/MSX2/NFASC/CDH3/FAM20C/BCL11A/RYR1
extracellular matrix organization	SCUBE1/COL27A1/HTRA1/TIMP1/COL9A1/ITGA6/ TCF15/CRISPLD2/ FBLN2/ADAM8/COL6A3/ICAM2/ADAMTS2/LAMC3/ SCX/LAMB3
voltage gated ion channel activity	CACNA1D/CACNA1G/CACNG2/RYR1
regulation of hormone levels	TRPV4/TSPOAP1/DIO3/BLK/ABCC8/CYP27C1/CHST8/ CACNA1D/SYT7/ADRA2A/ADCY5/DGAT2/SCG5/ ADORA1/MME/CD38/GLP1R/CYP26A1/SLC44A4
embryonic morphogenesis	ID2/MAFB/DUSP2/ATOH8/GSC/HES1/DNAAF1/ STOX1/HTR2B/TLX2/SNAI1/WNT6/COBL/DKK1/ APLNR/SOX18/MSX2/SCX/TH/SLC44A4/LAMB3/TBX1

Table A5 **Downregulated GO terms and the associated genes in SH-SY5Y STIM1$^{-/-}$**

GO term	Genes
apical plasma membrane	*RAB27B/CDHR5/DUOX1/SLC4A7/SLC34A3/LMO7/ EGFR/ATP7A/MPDZ/NOD1/CSPG4/STX3/PATJ*
sarcoplasmic reticulum exocrine system development	*ITPR3/ITPR2/CACNA2D1/GSTM2/ASPH/ITPR1 TGM2/LAMA5/SEMA3C/EGFR/IGSF3/LAMA1/RAB26*
apical part of cell	*RAB27B/ITPR3/CDHR5/DUOX1/SLC4A7/SLC34A3/LMO7/ EGFR/DYNC2H1/ATP7A/MPDZ/AFDN/NOD1/CSPG4/ MYO6/STX3/PATJ*
cell-substrate adhesion	*ABI3BP/FREM1/COL3A1/NID2/NID1/LAMA5/LAMC1/ ITGA4/MKLN1/ITGAV/FMN1/PKD1/ARHGAP6/DMD/ PEAK1/ITGA2/LAMB1/CDK6/VCL/MERTK/FAT2*
extracellular matrix organization	*ABI3BP/HSPG2/COL3A1/NID2/NID1/LAMA4/LAMA5/LAMC1/ LRP1/ITGA4/ITGAV/COL24A1/THSD4/MFAP4/FBN1/VCAN/ ATP7A/ITGA2/LAMB1/LAMA1/ERO1A/DCN*
cluster of actin-based cell projections	*ITPR3/CDHR5/MYO15B/ADGRV1/SLC4A7/SLC34A3/ADD3/ ATP7A/VCL/DOCK4/FLNB/PLEC*
cell substrate junction	*TGM2/FLRT1/FAT1/HSPG2/LRP1/ITGA4/ITGAV/AHNAK/ LMO7/CD46/EGFR/LPP/DMD/DST/PEAK1/FLNC/ITGA2/ ARHGAP26/VCL/CSPG4/LAYN/SNTB1/FLNB/PLEC*
extracellular matrix	*RELN/ABI3BP/FLRT1/FREM1/HSPG2/COL3A1/NID2/ LTBP2/FRAS1/NID1/LAMA4/LAMA5/LAMC1/LTBP1/ TRIL/COL24A1/NAV2/THSD4/MFAP4/FBN1/VCAN/ CHAD/DST/LAMB1/LAMA1/DCN*
ECM structural constituent	*ABI3BP/HSPG2/COL3A1/NID2/LTBP2/FRAS1/NID1/LAMA4/ LAMA5/LAMC1/LTBP1/COL24A1/THSD4/MFAP4/FBN1/VCAN/ LAMB1/LAMA1/DCN*

Table A6 **Upreguated GO terms and the associated genes in SH-SY5Y STIM1$^{-/-}$**

GO term	Genes
synaptic vesicle membrane	*SYN1/RPH3A/SVOP/SYT5/RAB3C/CLTA/CLTB/PTPRN2*
growth cone	*GAP43*
telencephalon development	*NEFL/ID2/NME1/DCX/NRGN/BCAN/H2AFX/CDK5R2/ RTN4R/C12orf57/UQCRQ/PAX5/DPYSL2/ATF5/CRTAC1/ PEBP1/RAN/CNTN2*

condensed chromosome	*SYN1/CDT1/RPA2/H2AFX/CDCA5/CENPV/CENPM/PMF1/ CENPX/PINX1/SKA2/SPC24/BIRC5/CENPW/NCAPH2*
unfolded protein response	*CCND1/ATP6V0D1/ATF4*
DNA conformation change	*RPA2/H2AFX/CDC45/ASF1B/CDCA5/CENPV/CENPM/ CENPX/CHAF1B/2AFY2/HIST1H1C/CHAF1A/HIRA/ CENPW/CHD4/NCAPH2/POLE3/MCM7/MCM6/HMGB3*
mitotic cell cycle phase transition	*ID2/CCND1/CDC6/MAD2L1BP/CDT1/PCNA/RPA2/ DYNLL1/CDC45/CDCA5/E2F1/CDK2AP2/HAUS8/ MAD2L2/LSM10/PINX1/HAUS1/TUBA1A/CDC25A/ SSNA1/RBX1/CDKN2C/RAD51C*
axon part	*NEFL/GAP43/STMN3/AP3B2/GPRIN1/NRCAM/HSPA8/ CPLX2/MAPK8IP1/DYNLL1/RANBP1/CDK5R2/RTN4R/ SNAP25/SHANK2/PTPRN/L1CAM/DPYSL2/ATP6V0D1/ CRTAC1/PTPRN2/PEBP1/CALB1/ANK1/CNTN2*
DNA replication	*GINS2/RRM2/ID3/FEN1/CDC6/PCLAF/CDT1/PCNA/RPA2/ DUT/HRAS/CDC45/MCM5/GINS3/RFC2/CENPX/CHAF1B/ MCM3/RMI2/GMNN/PTMS/CHAF1A/POLE3/MCM7/MCM6*
organelle inner membrane	*CKMT1B/GCAT/NDUFS5/AURKAIP1/TOMM40/TIMM8B/ TIMM13/UQCRQ/NDUFC2/TIMM10/MRPL51/NDUFB11/ MRPL1/ATP5F1E/MRPL20/NDUFB2/ATP5MC1/NDUFS3/ MRPL15/MRPL11/CKMT1A/MPC1/MRPL33/MRPL14/ NDUFS6/MRPL23/ATP5MD/NDUFB6/ATP5F1D/ COX6B1/NDUFA11/COA3/PPIF/NDUFB3/ATP5PF/NDUFA12/ ATP5MF*

Publications

Diener, C., Hart, M., Alansary, D., <u>Poth, V.</u>, Walch-Rückheim, B., Menegatti, J., et al. (**2018**). Modulation of intracellular calcium signaling by microRNA-34a-5p. *Cell Death and Disease*, *9*(10). doi:10.1038/s41419-018-1050-7

<u>Poth, V.</u>*, Knapp, M. L.*, & Niemeyer, B. A. (**2020**). STIM proteins at the intersection of signaling pathways. *Current Opinion in Physiology*, *17*, 63–73. doi:10.1016/j.cophys.2020.07.007

Ramesh, G., Jarzembowski, L., Schwarz, Y., <u>Poth, V.</u>, Konrad, M., Knapp, M. L., et al. (**2021**). A short isoform of STIM1 confers frequency-dependent synaptic enhancement. *Cell Reports*, *34*(11). doi:10.1016/j.celrep.2021.108844

Knapp, M. L., Alansary, D., <u>Poth, V.</u>, Förderer, K., Sommer, F., Zimmer, D., et al. (**2022**). A longer isoform of Stim1 is a negative SOCE regulator but increases cAMP-modulated NFAT signaling. *EMBO reports*, *23*(3), 1–20. doi:10.15252/embr.202153135

<u>Poth, V.</u>, Do, H. T. T., Foerderer, K., Tschernig, T., Alansary, D., Helms, V., & Niemeyer, B. A. (**2023**). A better brain? Alternative spliced STIM2 in hominoids arises with synapse formation and creates a gain-of-function variant. *bioRxiv*, 2023.01.27.525873. doi:10.1101/2023.01.27.525873

Danksagung

Es ist vollbracht! Eine aufregende Reise voller Höhen und Tiefen geht zu Ende.

An erster Stelle möchte ich mich von Herzen bei Barbara Niemeyer bedanken. Danke für deine uneingeschränkte Unterstützung, deine unglaubliche Geduld und inspirierenden Ideen. Ich bin dankbar für all die Möglichkeiten und Freiheiten, die du mir während der letzten Jahre gegeben hast, an denen ich nicht nur beruflich, sondern auch persönlich gewachsen bin. Deine Begeisterung für Forschung ist einfach ansteckend.

Danke an Thomas Tschernig und Nicole Ludwig für die Bereitstellung primärer humaner Gehirnproben und humaner RNA, das maßgeblich zu meinem Projekt beigetragen hat.

Ein großes Danke an Dalia. Du hast mir in diesem Labor so viel beigebracht und mich stets mit all deinen Tipps und Tricks unterstützt.

Danke an Mona, Maryam, Kathrin und Priska. Ihr habt mir den Alltag versüßt und einmal mehr gezeigt, wie wichtig solch wunderbare Kollegen sind. Ihr werdet mir fehlen.

Danke an Lukas für die unzähligen Neuronen-Präps, deine Klonierungsexpertise und deinen Remotesupport mit dem LSM egal zu welcher Uhrzeit.

Ein großes Danke an Cora, Gertrud, Carmen, Sandra, Kathrin, Andrea und Kathleen. Ihr erleichtert den Laboralltag enorm.

Unendlicher Dank geht an meine wundervollen Eltern, die mir erst diesen Weg ermöglicht und mich bei all meinen Vorhaben bedingungslos unterstützt haben. Ich hab euch lieb!

Mein besonderer Dank geht an Tim. Du hast die letzten 9 Jahre so viel mitgemacht, du hast einen eigenen Doktortitel verdient. Du gibst mir in schwierigen Zeiten Halt und feierst mit mir jeden noch so kleinen Erfolg. Du bist für mich da, wenn ich dich brauche. Gemeinsam schaffen wir alles!

Curriculum vitae

Aus datenschutzrechtlichen Gründen wird der Lebenslauf in der elektronischen Fassung der Dissertation nicht veröffentlicht.